NORTHWESTERN UNIVERSITY

An Experimental-Theoretical Investigation of the Mechanical and Interfacial Properties of Functionalized Graphene-Based Nanomaterials

A DISSERTATION

SUBMITTED TO THE GRADUATE SCHOOL
IN PARTIAL FULLFILMENT OF THE REQUIREMENTS

for the degree

DOCTOR OF PHILOSOPHY

Field of Theoretical and Applied Mechanics

By

Rafael Antonio Soler-Crespo

EVANSTON, ILLINOIS

December 2017

Abstract

An Experimental-Theoretical Investigation of the Mechanical and Interfacial Properties of Functionalized Graphene-Based Nanomaterials

Rafael A. Soler-Crespo

The exceptional mechanical properties of carbon-based 2D nanomaterials, such as graphene, have widely motivated researchers to incorporate them as constituents in novel, engineered devices and structural materials. A major bottleneck in this vision for graphene is the poor interfaces it can form: indeed, the low interfacial shear strength of graphene prevents successful scaling up of its mechanical properties. In this light, graphene oxide (GO), an oxidized variant of graphene capable of significant interfacial interactions, has gained significant interest in research communities as a viable alternative to scaling and the development of engineered systems.

While the rich chemistry of GO makes it amenable to scaling up strategies, it also creates a complex materials envelope with widely varying attainable properties. At the same time, the multitude of interfaces that GO can form leads to a wide library of complementary systems in the development of structural materials. In this light, experimentation becomes a poor alternative to design successful GO-based structures: notably, the number of trial-and-error cycles and potential experiments to reach viable designs and form a sufficient fundamental knowledge pool quickly becomes intractable. To address these limitations, the U.S. Federal Government has established the Materials Genome Initiative (MGI): a framework by which materials discovery and design is led by predictive simulations, and complemented by selective experimentation. However, to fully reach the vision of the MGI, a number of developments in tools and fundamental knowledge must be achieved.

Herein, we focus on the validation of theoretical tools that demonstrate their accuracy by simulating fundamental experiments and observations, which lead to a basic understanding of the material properties and toughening mechanisms present in GO and GO-based systems. First, we demonstrate a novel mechanochemical transformation in GO, accessible to only certain GO compositions, that endows the material with significant ductility. Next, this observation and contrasting reports in the literature motivated a full exploration of the GO structure-property space. By performing such a study computationally, we demonstrate how the mechanical properties of GO are correlated to its chemistry, and may lead to intrinsic toughening mechanisms. Finally, these studies motivated us to understand the existence and nature of extrinsic toughening mechanisms, which can be easily promoted in GO-polymer systems, and that lead to incredible mechanical performance. The methodology showed herein is utilized to preliminarily probe the substrate-polymer space for GO and demonstrate basic design rules and guiding principles which, in agreement with the tenets of the MGI, suggest viable pathways for the development of GO-based devices and structural materials.

Acknowledgements

This thesis is the culmination of various research contributions, and a large number of people have enabled it directly by providing support, collaborations and mentoring. First, I would like to thank my Ph.D. advisor, Prof. Horacio D. Espinosa, for his guidance throughout my graduate education. From him I learned the true definition of research, and I can only hope to inspire others to excellence as he inspired me. I would also like to thank my committee members (Profs. Sinan Keten, Jiaxing Huang and SonBinh T. Nguyen) for their support and guidance in evaluating the body of work I have established, and their key feedback to improve upon it.

The support of collaborators has been critical in the work presented in this thesis, spanning a multidisciplinary network of researchers. Ms. Lily Mao, Prof. SonBinh T. Nguyen and Prof. Jiaxing Huang supported materials preparation and characterization, and provided insightful discussions into how chemistry and mechanics synergize to achieve the materials performance reported herein. Mr. Zhaoxu Meng, Dr. Wenjie Xia, Dr. Luis Ruiz and Prof. Sinan Keten provided valuable lessons and collaboration in the development and use of coarse grained models. Finally, key HRTEM characterization protocols were made possible with aid from Dr. Jianguo Wen and Dr. Dean Miller from Argonne National Laboratories.

Throughout my graduate education, I have also been fortunate to work with incredible people. In no particular order, I would like to thank Drs. Jeffrey T. Paci, Wei Gao, Xiaoding Wei, Wonmo Kang, Ruiguo Yang, Allison Beese, Michael Chon and Matthew Daly. Each of these postdoctoral fellows taught me critical scientific and life lessons, and were role models in my maturation as a scientist and individual. I'd also like to thank my current and past colleagues (in no particular order): Richard (He) Zhao, Matthew Ford, Alireza Zaheri, Siyan Dong, Prithvijit Mukherjee, Zhaowen Lin, Hoang Nguyen, Xu Zhang, Cesar Patiño, Nibir Pathak, Andrea

Castiglioni, Massimiliano Milan, Antonio Pedivellano, Dr. Ben Russell, Dr. Changjin Huang, Dr. Juan Pablo Giraldo and Dr. Ivano Benedetti for their friendship, support and helpful discussions.

I would like to highlight the importance of three great friends I've made during my Ph.D. education: Dr. Michael R. Roenbeck, Samba Shiva Prasad Nathamgari and Rajaprakash Ramachandramoorthy. Without their support, laughs and sincere friendship the completion of my Ph.D. would have been harder than I can envision. Guys, I will miss you incredibly, and the fond memories I have made with you in the lab are something I will always cherish.

I am also forever grateful for the support of the staff at the Mechanical Engineering and Civil Engineering Departments – in particular, Jennie Edelstein, Pat Dyess, Sinta Kulanda, Rick Marzec and Nathan Youngblood – who have provided an incredible amount of support in administrative components of the Ph.D. forming experience. Truly, their work is very much appreciated because it allows us to focus on research, making the process straightforward and enjoyable.

This work was made possible through support from the National Science Foundation (DMREF Award No. CMMI-1235480), Army Research Office (MURI Award No. W911NF-08-1-0541) and NSF XSEDE (NSF XSEDE Award Nos. TG-MSS140028 and TG-MSS150003). I also thank the National Science Foundation GRFP program, Northwestern University and the International Institute for Nanotechnology for directly supporting my Ph.D. studies.

Finally, I would like to thank my wife (Alejandra Vivanco), my parents (Rafael Soler-Garcia and Antonia Crespo-Colon), my brothers (Luis and Jose Soler-Crespo) and God for their unconditional love, support and never-ending patience. They all have been my strength and my motivation, and I am eternally thankful for their love and presence in my life. I love you all very much.

To my wife and my mother, the most important women in my life

Table of Contents

List of Figures

List of Tables

Chapter 1: Introduction and Motivation

The ever-present need for engineered, lightweight materials with exceptional performance continues to be the prevailing motivation underpinning research efforts in the design of advanced composites. Notably, the collective properties of composites have been shown to be dominated by their structure, constituents and mechanistic behavior[1]. Thus, within the context of materials design, the selection of chemistry, functionality, and fabrication methodologies is a critical aspect in delivering architectures and motifs which expand the performance space of engineered composites. This search for effective architectures and material hierarchies is guided by synergistic design outcomes, whereby the weight-normalized mechanical performance of composite materials is drastically improved beyond that of the individual constituents[1]. In addition to the design space of hierarchies, the selection criteria for the matrix and reinforcing phases are fulfilled by a large variety of constituents, which creates a significantly vast design space[1-3] and allows engineers to contemplate unique synergistic effects in the design of composite materials[3-4].

As part of this broad materials envelope, the emergence and rise of atomically thin 2D materials represents the apex of nanoscale refinement, offering reinforcing constituents with unprecedented properties and reaching the theoretical limits of surface-to-volume fractions[5]. With respect to composites design, the monolayer nature of 2D materials is particularly attractive, as it enables bottom-up design schemes, which facilitates precise spatial tailoring of mechanical properties and constituent interactions. In this regard, the design flexibility facilitated by atomically thin materials presents an unprecedented opportunity for transformative breakthroughs in composites research and materials engineering. However, despite their success in nanoscale electronic and piezoelectric devices[6-8], the development of structural materials based on atomically thin 2D constituents has been frustrated by the disconnect between the materials- and application-

scales. For example, graphene oxide (GO) is known to possess monolayer strengths in the GPa-range[9-11], which are accessible through a directed failure of the in-plane sp^2/sp^3 covalently-bonded network. Conversely, bulk GO papers have been reported to fail at tensile loads of ~ 120 MPa[12], driven by interplanar shearing of monolayer stacks[13]. This disparity between in-plane and interfacial mechanical strengths is a general characteristic of 2D materials, and represents a significant roadblock for the scalability of atomically thin materials to structural dimensions[5].

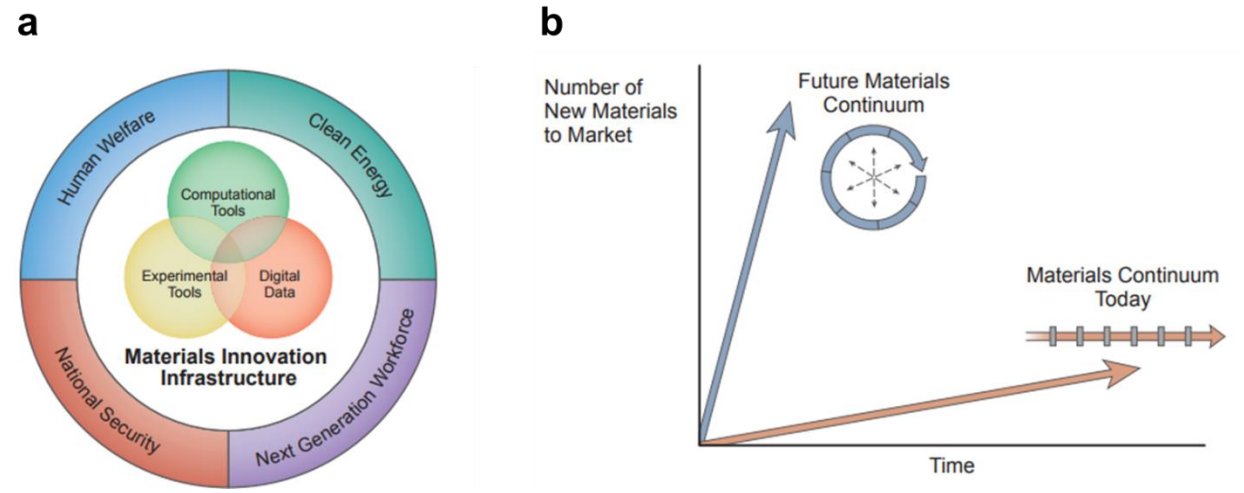

Figure 1. Summary of vision and mission for Materials Genome Initiative. a, A combination of social and technological driving forces will lead to a synergistic combination of theoretical and experimental tools in the search of novel design infrastructure. **b,** Previous materials continuum design trends are linear and cumbersome, with little feedback between different design steps. The Materials Genome Initiative seeks to revolutionize such approaches by highlighting the importance of integrated, computationally-driven design trends to expedite materials discovery and design. Adapted from the original Materials Genome Initiative white paper, found on [14].

In this light, and within the context of composites design, a tailoring and optimization of constituent interactions at the interfacial scale must also be undertaken[2, 5]. This process establishes an ideal interlayer chemistry, which provides strong bonding between 2D building blocks, and facilitates cohesive multiscale mechanical behavior. However, the assembly of a wide library of constituents into novel structural composites, which must also closely consider their interfacial interactions, represents an inherently multiscale and complex problem, cumbersome for experimental tools but amenable to investigation with predictive computational tools. Indeed,

experimental tools such as atomic force microscopy (AFM) testing are often paired with complementary computational simulations in order to measure the intrinsic strength of 2D materials[9, 15] and elucidate the complex deformation mechanisms that arise during testing[9-11], which are not directly observable in experiments at the nanoscale. Concurrently, and in an effort to circumvent crucial experimental limitations, computational researchers are continuously developing new approaches and techniques that provide efficient and accurate descriptions of atomistic phenomena in materials[16-20], and can expedite the design process by providing reasonable input into the appropriate selection of materials for consideration.

Frustrated by the ever-increasing time-to-deployment between the conception and realization of engineered systems, and in view of the increasing role of computational tools in materials discovery and design, the White House of the United States released a white paper titled *Materials Genome Initiative for Global Competitiveness* in June 2011[14]. Here, a direct call was made to scientific communities to invest research efforts into accelerating materials design using predictive computational models with selective experimental verification[14] (Figure 1a). The Materials Genome Initiative (MGI) description emphasized that traditional linear materials design approaches prohibit feedback between scientists at different stages in the design process, which results in exorbitant delays and economic costs[14] from the conception of an idea to its eventual deployment. Such material design processes, it was argued, stood to benefit from predictive tools that can speed up and enhance the materials design continuum (Figure 1b). Notably, scientific communities have greatly benefited over the past 20 years with the advent of modern computational techniques, whose role has become increasingly critical in describing physical and chemical phenomena of interest[21] beyond what experiments may capture. Furthermore, computational tools have become widespread due to modern breakthroughs such as GPU

computing and videogame consoles clustering[22-23], enabling access to research communities to a larger pool of computational resources. These factors, thus, justify the realization of computationally-guided materials research as an attractive opportunity, and support the principles set forth by the Materials Genome Initiative.

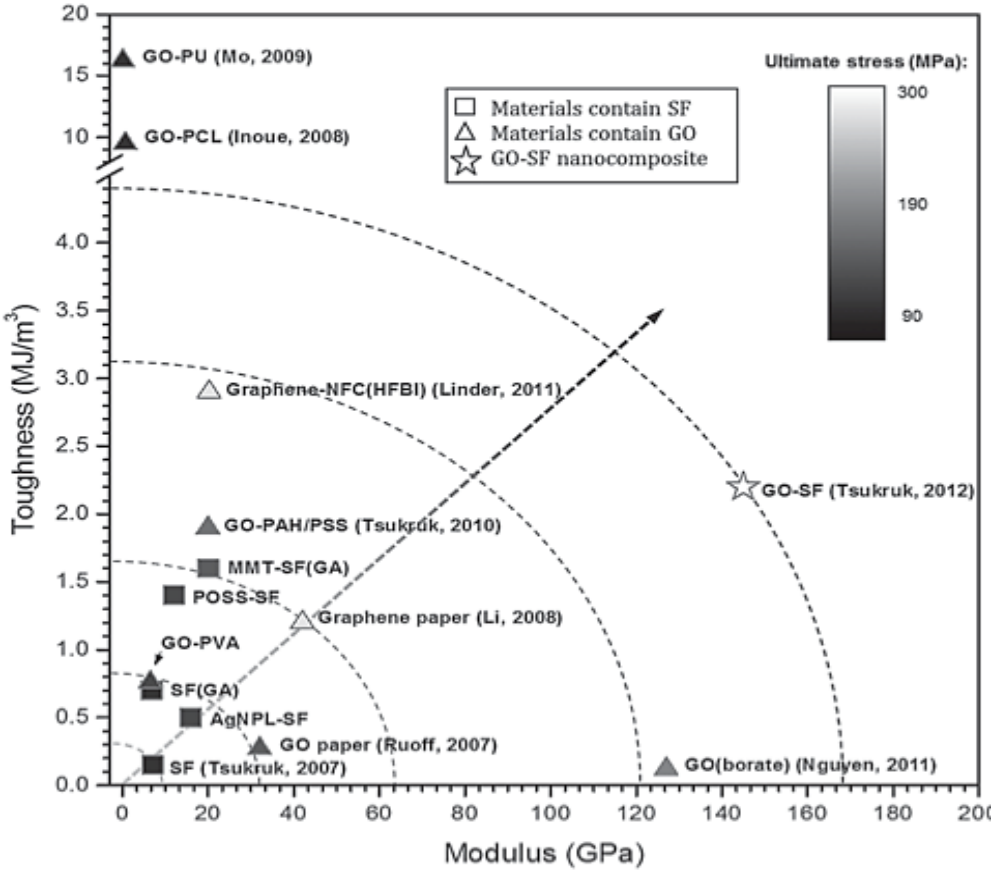

Figure 2. Ashby plot for a variety of composites derived from graphene oxide (GO), graphene and other material systems modified with silk fibers (SF) and other matrix materials. Reprinted from [24] with permission from John Wiley and Sons.

Clearly, a variety of test beds are viable for the application of the methodologies highlighted by the MGI, but the development of novel carbon-based lightweight nanocomposite structures with incredible mechanical properties, such as those originally envisioned based on graphene building blocks[25], remains especially promising. In terms of structural properties, carbon-based nanomaterials have been reported to possess extraordinary mechanical properties

and their aspect ratio is amenable to the design of engineered materials. Furthermore, these nanomaterials remain an active research front in both experimental[9, 11, 26-27] and theoretical[10-11, 28-29] research circles, and the development of tools that can probe nanomaterials[10-11, 15] continues forward at a remarkable pace. In this light, the poor interlayer mechanical strength of graphene[5] has frustrated its use as an engineering constituent but its functionalized variants, *e.g.* GO, enable the possibility to achieve improved mechanical performance due to their potential tunability and enhanced interfacial behavior[2, 27, 29-30]. However, the wide materials envelope provided by functionalized carbon-based nanomaterials is too broad to study as an initial foray into the ideologies of the Materials Genome Initiative. For this reason, and given its exceptional promise in terms of its chemistry and facile fabrication, research circles have paid increasing attention to GO.

GO, as an oxidized variant of graphene, provides rich chemistry which is also capable of forming strong interfaces. This has led to it becoming the focus of increasing composites design with various manufacturing strategies, which have often led to mixed results[12, 24, 30-31]. Notably, no engineered composite material has been able to harness all the promising intrinsic mechanical properties of GO (Figure 2). This can be attributed, in part, to the poor body of fundamental knowledge that has existed to date, which hinders the establishment of logical design pathways from which the material can be modified and optimized to yield innovative solutions to engineering problems. From this perspective, GO presents an extremely rich proposition: by performing fundamental experiments and theoretical studies, it is possible to validate theoretical tools while discovering fundamental material behavior, which will in turn guide engineers in the optimum ways to design GO-based composites and devices. In this regard, the objectives of this thesis study are to: i) design a combination of experimental and theoretical methods and protocols

that can accurately capture the mechanical and interfacial properties of functionalized graphene-based nanomaterials; and ii) identify structure-property relationships and guiding principles which control mechanical and interfacial behavior, at the molecular level, for functionalized graphene-based materials.

This work is divided as follows: Chapter 2 provides a fundamental overview of the experimental and theoretical methodologies, as well as the motivation and usefulness, of techniques employed in this thesis. In Chapter 3, I present a study of GOs with a particular composition which enables a strongly ductile response. Motivated by Chapter 3 and results in the literature, Chapter 4 summarizes a computational study, in agreement with the ideology of the Materials Genome Initiative, that captures the critical relationships between the composition of GO and its resulting mechanical behavior. Then, motivated by the discovery of intrinsic toughening mechanisms in GO, we demonstrate in Chapter 5 how this toughening for GO monolayers can be further augmented by introducing extrinsic crack bridging, toughening mechanisms by the addition of an atomically-thin PVA layer. Finally, in Chapter 6, we summarize the reported work, demonstrate a preliminary generality of the theoretical tools developed herein, and give perspective into the future of the field. Given the wide variety of covered topics in this thesis work, each Chapter is self-contained and directly provides the relevant background information and literature.

Chapter 2: Core Analysis Techniques – Materials Synthesis, Nanomechanical Characterization and Theoretical Analyses

The length and temporal scales associated with key molecular processes in functionalized graphene-based systems require the identification and employment of particular research tools that can convey information to researchers that originates at the atomic and molecular level. In this light, a key suite of experimental and theoretical tools has been critical to uncover the fundamental deformation mechanisms and interfacial behavior of GO and GO-polymer based systems. Given their highly correlated and transferable nature, key methods are discussed in Chapter 2 for ease of reference for the reader. Each individual Chapter then expands on particular modifications to experimental or theoretical methodologies as needed, and provides particular parameters or metrics employed in each study. A description of materials preparation and characterization is first given, followed by experimental characterization and lastly theoretical analysis techniques that complement experimental findings.

Materials Synthesis

Contributions and credit: **Ms. Lily Mao, Prof. SonBinh T. Nguyen** and **Prof. Jiaxing Huang** identified key synthesis and characterization pathways for all materials used in this thesis, and **Dr. Jianguo Wen** and **Dr. Dean Miller** assisted with HRTEM characterization.

Theoretical tools are able to predict mechanisms that involve deformation pathways and molecular interactions. However, the successful validation and verification of such observations necessitates selective experimental validation with materials and conditions that closely replicate the modeling framework. The first, and most crucial, pathway to this verification is the synthesis and characterization of materials to ensure the systems modeled at the molecular level match those

that are subjected to experiments. This section describes the synthesis and chemical characterization of GO and GO-based materials, which are later subjected to experiments that corroborate theoretical findings.

Synthesis of GO

The first step towards the design of the experimental protocols in this thesis is the synthesis of the base material, which may be then subjected to experimental testing. There are multiple pathways to synthesize GO available to researchers[32-34], which vary in the obtained composition and reaction mechanisms. To achieve control over the resulting chemistry, and to facilitate the synthesis of the material, it is ideal to employ a reaction pathway which is well established and shown to achieve selective control over the reaction product by manipulating key steps in the materials creation.

Herein, each batch of graphite oxide was prepared using a modified Hummer's method[34]. Briefly, a 9:1 v/v mixture of concentrated H_2SO_4 (360 mL):H_3PO_4 (40 mL) was added to a mixture of graphite (3 g) and potassium permanganate (18 g). The reaction mixture was heated to 50 °C and stirred for 12 h. The mixture was then cooled to room temperature and poured over ice (~400 mL), followed by the addition of H_2O_2 (8 mL of a 30 wt % solution) until the solution turned bright yellow. The resulting graphite oxide was filtered through a 250 μm U.S. Standard testing sieve (VWR International LLC, Radnor, PA) and centrifuged (8228 rcf for 1 h) in a model 5804R centrifuge (Eppendorf, Inc., Westbury, NY) with the supernatant decanted away. The remaining solid was then washed with ultrapure deionized water (200 mL), HCl (200 mL of a 30 wt % solution), and ethanol (2 × 200 mL). After each wash, the mixture was filtered through the sieve and then centrifuged (8228 rcf for 1 hour) with the supernatant decanted away. The remaining

material was coagulated with ether (200 mL) and filtered over a PTFE membrane (Omnipore, 5 μm pore size, Millipore Inc., Billerica, MA) overnight. The GO filter cake was then dispersed in ultrapure deionized water, with the dispersion stirred for 18 hours. Any residual, unexfoliated graphite oxide was removed by centrifuging at 8228 rcf for 5 min (2x) with the precipitate discarded. The final dispersions contained ~3 mg mL^{-1} of graphene oxide (GO), with a C:O ratio determined by elemental analysis to be 1.13. Accounting for water content of 14.53% results in a C:O ratio of 1.57. GO films for XPS analysis, to identify the chemistry in the material, were prepared by drop casting GO solution onto silicon wafers with an oxide layer, followed by drying in ambient conditions.

Preparation of Si Substrates with Microwells

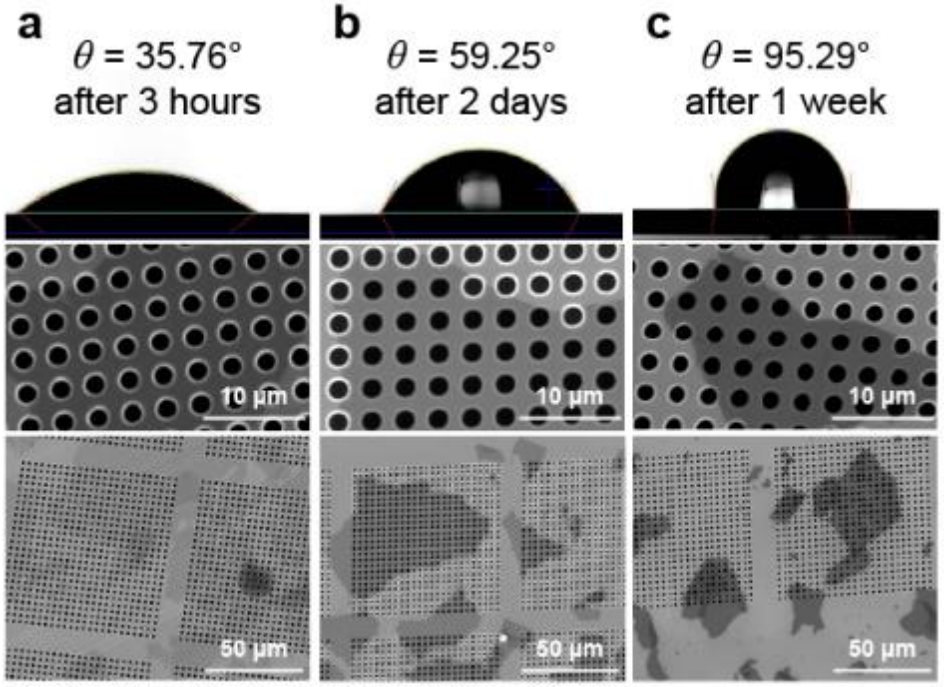

Figure 3. Effect of θ, the water contact angle of the substrate, on LB deposition of suspended GO membranes. Top row: Water contact angles of bare Si substrates at various times after substrate cleaning. **Middle and bottom rows:** SEM images of GO monolayers deposited on the same substrates with the water contact angles shown above. Wells that contain a ruptured membrane have bright edges due to the edge effect, while those that contain intact membranes have dark edges. **a,** Deposition on a substrate with < 60° water contact angle results in ruptured membranes. **b,** Deposition on a substrate with an optimal water contact angle of ~ 60° yields intact membranes. **c,**

Deposition on a substrate with > 60° water contact angle yields a lower coverage of intact but wrinkled membranes, presumably due to the hydrophobic nature of the substrate surface.

Si substrates containing arrays of microwells with 1.76 µm diameter and 4 µm depth were fabricated using a combination of photolithography and deep reactive-ion etching (DRIE), to suspend GO and GO-PVA monolayered specimens for nanomechanical characterization (discussed further in this Chapter). A 1.2 µm-thick photoresist layer (S1813 positive photoresist manufactured by Dow Electronic Materials Microposit, catalog number: DEM-10018348, Capitol Scientific, Inc., Austin, TX) was spin-coated onto the Si wafer at 4000 rpm using a spin coater (Cee 200X, Brewer Science, Inc., Rolla, MO). Following a 1 minute soft bake at 100 °C on a hot plate, the wafer was exposed to UV light (365 nm, 18 mW cm^{-2}) for 4 seconds on the Mask Aligner instrument (Suss MABA6, SÜSS MicroTec AG, Garching, Germany). After exposure, the wafer was developed in a MF 319 developer (manufactured by Dow Electronic Materials Microposit, catalog number: DEM-10018042, Capitol Scientific, Inc., Austin, TX) for 60 seconds. Spin rinsing was carried out with ultrapure deionized water (200 mL) for 30 seconds at approximately 300 rpm, followed by a 60 second spin dry at 3000 rpm.

The resulting photoresist-masked silicon wafer was then subjected to microwell etching using a DRIE machine (STS LpX Pegasus, SPTS Technologies Ltd, San Jose, CA). After etching, the remaining photoresist was removed using acetone, and the wafer was cleaned using isopropanol and ultrapure deionized water. This wafer was then cleaved into smaller substrates to be used in the LB deposition and subsequent membrane-deflection experiments.

Prior to LB deposition, the substrates were cleaned using the following procedure: 1) submerged in 2 mL of a 3:1 v/v mixture of conc. H_2SO_4:30 wt % H_2O_2 and heated in a Biotage (Uppsala, Sweden) SPX microwave reactor (software version 2.3, build 6250) at 180 °C for 45

min, 2) sonicated for 10 min each in ultrapure deionized water (~10 mL), methanol (~10 mL), and ultrapure deionized water (~10 mL), respectively, 3) dried under a flow of nitrogen for 1 min, and 4) treated with O_2 plasma (5 min at 190 W and 10-15 mTorr O_2) in a South Bay Technology, Inc. (San Clemente, CA) Model PC-2000 plasma cleaner. After this cleaning process, the substrates were left under ambient conditions and their water contact angle was monitored until the desired value was reached prior to LB deposition of GO and GO-PVA specimens (see procedure below). As captured in Figure 3 and shown previously[11], the yield of intact suspended GO membranes is dependent on the water contact angle of the substrate. As such, substrates with a water contact angle of approximately 60-70° were used to prevent membrane rupture.

Langmuir-Blodgett Assembly of GO and GO-PVA

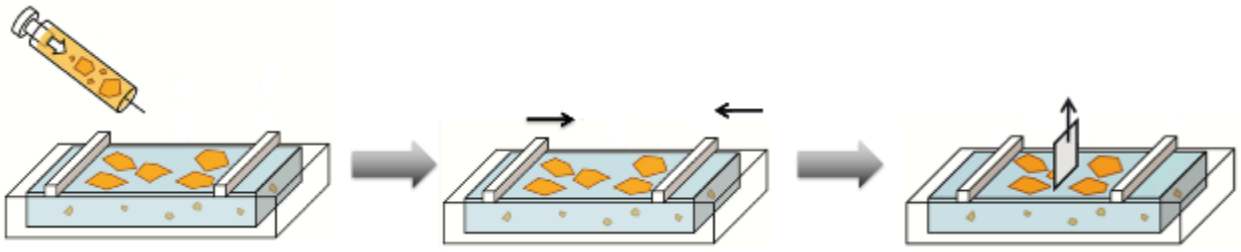

Figure 4. Schematic of Langmuir-Blodgett (LB) deposition process. GO films are suspended over a water bath to form a suspended film, and compressed together via surface tension that arises by bring towards each other two movable plates in a trough. Then, a substrate is dipped and slowly raised. Through surface tension, GO monolayers adhere to the substrate. Adapted from [35].

To prepare suspended, single GO and GO-PVA nanosheets for the AFM membrane-deflection experiments, the Langmuir-Blodgett (LB) assembly method (Figure 4) was employed[35-36]. The as-prepared aqueous GO dispersion was diluted with MeOH to a mixture of 5:1 v/v MeOH:GO dispersion. The Nima technology (Espoo, Finland) model 116 trough was cleaned with acetone, and filled with ultrapure deionized water. Typically, the GO/MeOH solution (300-480 μL) was spread onto the water surface dropwise at a rate of 100 μL min^{-1} using a glass syringe, forming a monolayer film on the surface. The surface pressure was monitored using a tensiometer

attached to a Wilhelmy plate. The film was allowed to equilibrate for at least 20 min after spreading, and then compressed by barriers at a speed of 100 cm^2 min^{-1}. Single GO nanosheets were transferred near the onset of the surface pressure increase by vertically dipping the substrate into the trough and slowly pulling it up at a rate of 2 mm min^{-1}.

The LB technique was also used to deposit an ultrathin PVA layer onto the suspended GO monolayers (see above) to create GO-PVA nanolaminate samples (see Chapter 5 for schematic). To prevent the GO monolayer from washing off during the deposition, PVA was deposited the day after LB deposition of the GO. A 1 mg/mL aqueous solution of PVA was diluted with EtOH to a mixture of 5:1 v/v EtOH:ultrapure deionized water. The Nima technology (Espoo, Finland) model 116 trough was cleaned with acetone, and filled with ultrapure deionized water. Generally, PVA solution (600 μL) was spread onto the water surface dropwise at a rate of 100 μL/min using a glass syringe, forming a film on the surface. The surface pressure was monitored using a tensiometer attached to a Wilhelmy plate. The film was allowed to equilibrate for at least 20 min after the spreading, and then compressed by barriers at a speed of 100 cm^2/min. The PVA layer was transferred at a surface area of 50 cm^2 by vertically dipping a substrate containing suspended GO monolayers into the trough and slowly pulling it up at a rate of 2 mm/min. The presence of GO and/or PVA was confirmed using electron microscopy and XPS characterization (see below).

Preparation of PVA-GO-PVA Nanolaminate and Bi-Nanolaminate Structures

In Chapter 5, we show how crack bridging, provided by a nanostructured network formed by atomically thin PVA chains deposited over GO monolayers, greatly enhances the fracture toughness and optimizes the stiffness of GO-PVA nanolaminate materials. In this light, it is natural to examine the ease to stack such materials to assemble nanocomposite systems, and their scaling

mechanical performance. Indeed, if the mechanical performance of GO-PVA nanolaminates is poor as the system is scaled, this observation points to the need to solve fundamental issues that affect system performance prior to composite assembly. Herein, we make first steps into investigating such scaling behavior issue by studying mono- and few-layered structures, and directly correlating their mechanical performance.

To prepare such systems, an aqueous PVA solution was prepared by dissolving PVA (200 mg) in ultrapure deionized water (16.7 mL) and stirring for at least 3 hours. This solution was mixed with the as-prepared aqueous GO dispersion (3.335 mL) to yield a 1:20 w/w GO:PVA dispersion, which was diluted to a final volume of 30 mL and centrifuged at 8228 rcf for 20 min. The supernatant was decanted to remove excess PVA not bound to GO nanosheets and the precipitate was re-dispersed in ~27 mL of ultrapure deionized water. The resulting dispersion of PVA-GO-PVA was spin-coated onto the patterned Si substrates at 2000 rpm, with an acceleration of 200 rpm to obtain a mix of PVA-GO-PVA nano- and bi-nanolaminates, which could be distinguished based on SEM and AFM characterization.

XPS Characterization of GO and GO-PVA

XPS is a powerful technique for the characterization of the surface chemical composition of nanomaterials, and has been extensively used to study functional groups in GO[37-38]. While XPS can detect these functional groups with high accuracy, the resulting C1s spectrum consists of several overlapping peaks corresponding to the different types of carbon atoms present. To accurately quantify the amount of each functional group, the C1s XPS spectrum must be carefully deconvoluted using the correct binding energies and number of peaks. Among previously reported studies, variation in the binding energy assigned to each functional group is presumably due to the

heterogeneous chemical structure of GO. Whereas the structural model of GO includes five types of functional groups, some researchers may choose to assign only four peaks to simplify deconvolution. For example, a common practice is to fit the epoxide and hydroxyl groups as a single peak, rather than as two separate peaks. However, this does not imply that XPS cannot distinguish between epoxide and hydroxyl groups. Although these two groups are expected to have similar binding energies, the epoxide group (C-O) can exhibit a larger chemical shift (relative to the C-C group) into the emission range of the carbonyl group (C=O)[37, 39]. Indeed, several previous works separately deconvoluted and quantified epoxide and hydroxyl groups[39-41].

X-ray photoelectron spectroscopy (XPS) was gathered in the Keck II/NUANCE facility at Northwestern University using a Thermo Scientific ESCALAB 250Xi (Al Kα radiation, $h\nu$ = 1486.6 eV) (Thermo Fisher Scientific Inc., West Palm Beach, FL) equipped with an electron flood gun. Samples for XPS analysis were prepared via LB deposition of GO and GO-PVA onto Si wafers (Item #785, 100 mm diameter, p-type, B-doped, single side polished) purchased from University Wafer, Inc. (Boston, MA). XPS data was obtained from three different locations on the surface of each sample, and was analyzed using Thermo Scientific Avantage Data System software (version 5.923), with a Smart background subtracted prior to peak deconvolution and integration.

Table 1. Tabulated XPS peak locations and intensities for GO.

Bond Type	Binding Energy (eV)	Relative Area
C-C	284.46	27.4%
C-OH	285.90	2.3%
C-O	286.52	60.6%
C=O	287.88	9.5%
C(O)O	289.42	0.3%

The C1s XPS spectrum of GO was deconvoluted into five peaks corresponding to the functional groups and binding energies listed in Table 1. Binding energies were based on

previously reported values[42] and are in good agreement with the literature[34, 37, 39-41]. All spectra were calibrated by assigning the binding energy of the graphitic peak (C-C) at 284.46 eV. The C-C binding energy is normally assigned at 284.5-285.0 eV, with chemical shifts of +1.5, +2.5, and +4.0 eV typically assigned to the functional groups of C-OH, C=O and C(O)-O[43]. We fit the epoxide and hydroxyl groups separately, assigning the peak at 285.90 eV to the C-OH group, and the peak at 286.52 eV to the C-O group. The peaks at 287.88 eV and 289.42 eV were attributed to the C=O and C(O)-O group, respectively. Based on this analysis, the percentage of graphitic carbon atoms (C-C) in our unmodified GO is 27.4%, while the oxidized carbon atoms consist mainly of epoxides (C-O, 60.6%) (see Chapter 3 for further details).

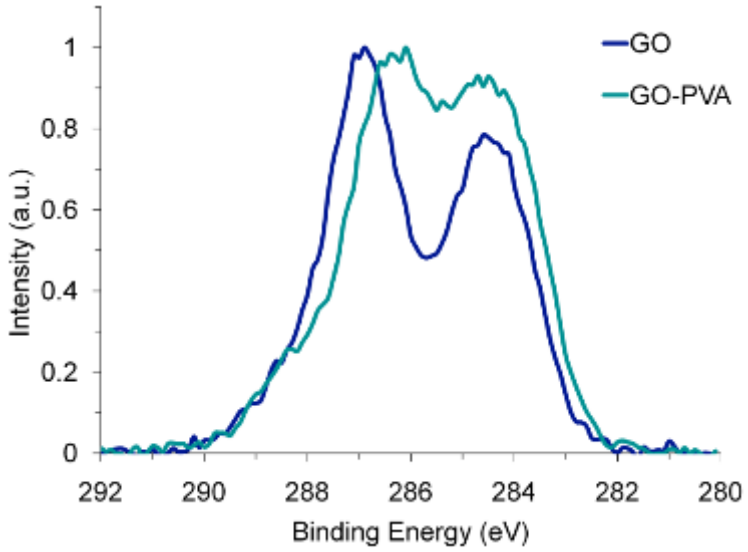

Figure 5. C1s XPS spectra of GO and GO-PVA. Both the peak shape and position of the GO spectrum change upon addition of PVA, indicating the successful modification of GO.

With regards to GO-PVA, we show further below and in Chapter 5 that EELS can capture the nanostructure of GO-PVA nanolaminates. Notwithstanding, XPS allows a quick and accurate verification of the adsorption of PVA molecules on GO nanosheets over the micron length scale, due to the larger XPS spot size (500 μm). Compared to the C1s XPS spectrum of GO, that of GO-PVA exhibits a clear change in the peak position, which can be attributed to the addition of PVA,

as captured in Figure 5. While the spectra of both materials contain a peak at a binding energy of 284.5 eV, corresponding to the graphitic carbon atoms of GO[43], the second peak in the GO-PVA spectrum (centered at 287 eV) is clearly shifted to a lower binding energy than that of GO (centered at 286.5 eV). In the GO spectrum, this second peak can be deconvoluted into five components corresponding to the oxygenated functional groups of GO, with the hydroxyl group at the lowest binding energy[37, 39]. Modification of the GO surface with PVA, which contains hydroxyl groups that have a similar binding energy (286.1 eV[44]) to those of GO (285.9 eV[42]) increases the overall hydroxyl content. As such, it is reasonable to expect the peak representing the combined oxygenated groups of GO to shift to a lower binding energy. This explains the shift in the oxygenated peak position of GO-PVA and confirms the adsorption of PVA on GO.

In addition to the peak position, the relative peak intensities are noticeably different in GO and GO-PVA. The intensity of the oxygenated peak in GO (287 eV) is significantly greater than that of the peak corresponding to graphitic carbon atoms (284.5 eV). In contrast, the intensity of the oxygenated peak in GO-PVA (286.5 eV) is similar to that of the graphitic carbon peak, suggesting that addition of PVA decreases the oxygen to carbon (O:C) ratio in GO-PVA. This is reasonable as the synthesized GO nanosheets have an O:C ratio of 0.66 (as determined by XPS survey scan), while pure PVA has an O:C ratio of 0.5. For the prepared GO-PVA nanolaminates, which contain GO and PVA in an approximate 1:1.5 weight ratio (based on the thickness and similar chemical composition of the two materials, see Chapter 5), an O:C ratio of 0.56 would be expected. In agreement with this prediction, the measured O:C ratio for the prepared GO-PVA nanolaminates is 0.61. Together with the XPS spectrum of GO-PVA, this data confirms that the PVA coverage detected by EELS is also present across the entire surface of GO-PVA nanolaminates.

TEM, STEM and EELS characterization of GO and GO-PVA

Transmission electron microscopy (TEM) and its associated characterization techniques, *e.g.*, scanning transmission electron microscopy (STEM) and electron energy loss spectroscopy (EELS), remain some of the most powerful techniques that convey information at atomic and molecular length scales to researchers[45]. High resolution TEM has been successfully used to characterize the microstructure of GO and validate the Lerf-Klinowski model for its microstructure[46-47]. Indeed, TEM in general provides access to critical materials characterization at the atomic level, *e.g.*, crystal structure and atom arrangement[45, 48-49]. However, based on the studied sample, TEM alone cannot reliably inform researchers on the chemical composition of a material. To bolster TEM capabilities, EELS spectroscopy, which can resolve the atomic identity of atoms that cause electron energy loss and scattering after interacting with the TEM electron beam, can be employed[45]. This technique has been successfully used to chemically identify a wide variety of materials imaged using TEM[45, 50-52]. Indeed, materials like polymers, which typically have no free electrons, display plasmon-like peaks in low-loss EELS spectra that can result in successful materials identification[45, 50]. Furthermore, when point-by-point information and EELS spectra are necessary to identify the location of particular atoms, then STEM, which provides highly localized sample information (<0.2 nm), can be utilized. Indeed, STEM has been recently used to probe the structure of functional groups in GO[52].

For the studies herein, HRTEM, STEM, and EELS characterizations were conducted using the Argonne Chromatic Aberration-Corrected TEM (ACAT) (a FEI Titan 80-300 ST with an image aberration corrector to correct both spherical and chromatic aberrations) at an accelerating voltage of 80 kV to reduce knock-on damage. The nanolaminate TEM specimens were prepared

by sequential Langmuir-Blodgett deposition of GO and PVA, or spin-coating a premixed aqueous solution of GO and PVA, onto TEM grids. HRTEM images were taken under conditions when spherical and chromatic aberration coefficients are corrected below certain values (C_s < 5 μm, C_c < 10 μm). Low-loss EELS spectra were recorded in an image-coupled mode. To avoid electron beam damage, a low probe current (5 pA) in STEM mode, relatively large probe size (~0.25 nm), and short dwell time (0.1 second) were used for the EELS line scan.

A comparison of the fast Fourier transform (FFT) patterns of GO and GO-PVA TEM images acquired in the ACAT (Figure 6) reveals no significant differences between the two materials, showing that TEM analysis alone cannot distinguish between them. Due to the presence of graphitic domains in GO and GO-PVA, both materials exhibit a symmetric six-fold pattern similar to that of pristine graphene (Figure 6a). The blurring of this six-fold pattern is attributed to the severe breaking of lattice symmetry in the graphitic domains of GO and GO-PVA. While oxidized domains are observable in HRTEM, these also do not convey sufficient information to readily detect the presence of PVA chains. Thus, and as alluded to before, TEM alone is not a sufficient technique to identify the presence and adsorption location of PVA chains.

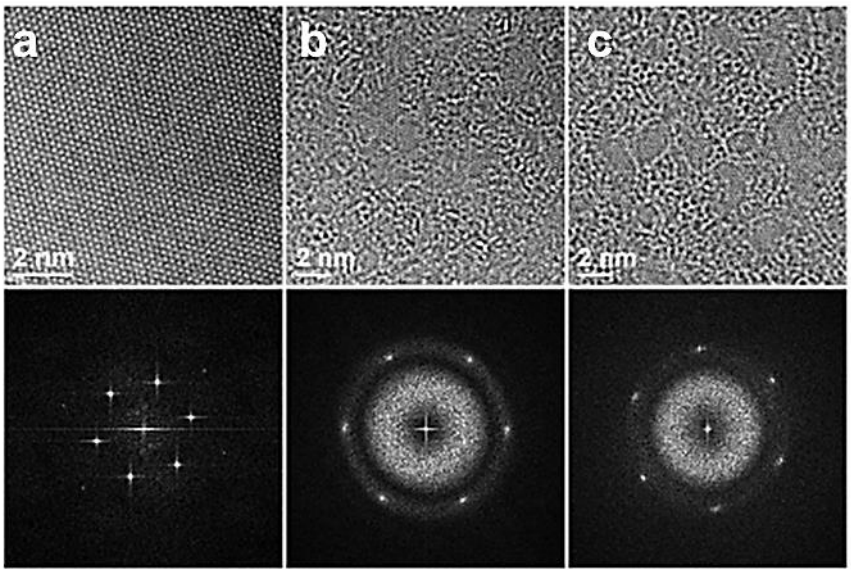

Figure 6. HRTEM images and fast Fourier transform (FFT) patterns for studied specimens. a-c, Shown are HRTEM and FFT patterns for single-layer graphene (**a**), GO (**b**), and GO-PVA (**c**). Both GO and GO-PVA exhibit graphitic domains dispersed throughout a continuous network of oxidized domains.

To circumvent limitations from SAED and FFT analysis of TEM images, EELS and STEM were employed to chemically characterize GO-PVA nanolaminates at the molecular level given the technique's sensitivity to chemical information that arises from local bonding. A series of control samples (graphene, GO, GO-PVA, PVA, and amorphous carbon) were prepared and characterized via EELS in TEM mode to serve as references for interpreting the EELS data of GO-PVA nanolaminates. Single-layer graphene samples, pre-deposited on Au-coated QUANTIFOIL R 2/4 TEM grids, were obtained from Graphenea Inc. (Cambridge, MA). GO and GO-PVA nanolaminate specimens were deposited onto lacey carbon-coated Cu TEM grids (Product #01895, Ted Pella, Redding, CA) via the LB method. PVA samples were prepared by spin-coating ~8 µL of an aqueous PVA dispersion (30 mg/mL) onto lacey carbon-coated Cu TEM grids at 4000 rpm, with an acceleration of 400 rpm used to reach this final speed.

The bare lacey carbon film of the prepared TEM grids served as the amorphous carbon samples. During TEM experiments, a short exposure time of 0.1 second was used to prevent

possible amorphous carbon buildup, which could alter the sample's plasmon peak position. The plasmon peak positions of the other reference samples were consistently below that of amorphous carbon (25 eV), suggesting there was no significant carbon buildup during experiments, and the obtained peak positions are representative of the non-contaminated control samples.

Previous studies have shown that the position of the π + σ plasmon peak in the EELS low-loss region (<100 eV) can be used to differentiate carbon-based materials such as graphene[51], GO[52], amorphous carbon[52], and organic polymers[50]. The π + σ peak in the EELS spectrum of unmodified GO is in good agreement with a previous report[52], and is significantly right-shifted in comparison to the π + σ peak of graphene, attributable to the presence of oxygen and the increased number of sp^3 carbon bonds in GO[52]. For pure PVA, which has a 2:1 C:O content and only sp^3 carbon atoms, the π + σ peak is at 23 eV, as shown in Figure 7. As such, the addition of a PVA layer (66% sp^3 carbon) on top of GO (~30% sp^3 carbon), as present in GO-PVA nanolaminates, should cause the π + σ plasmon peak of GO to shift to values in the 19-23 eV range. This is indeed observed in the EELS spectrum of GO-PVA nanolaminates, which exhibits a broad feature at ~21 eV, as shown in Figure 7. As this feature spans a large 17-23 eV range, it likely comprises individual contributions from GO and PVA.

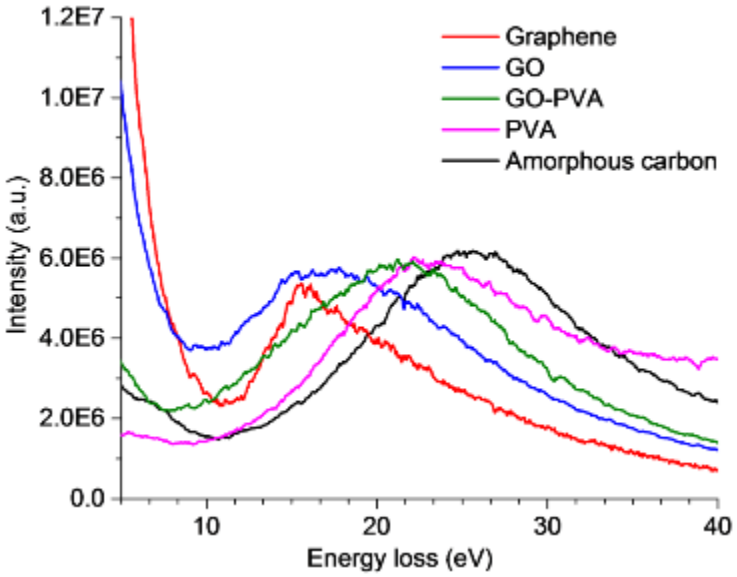

Figure 7. EELS spectra (collected in TEM mode) showing the π + σ plasmon peaks of graphene, GO, GO-PVA, PVA, and amorphous carbon.

Based on the aforementioned reference data, the position of the plasmon peak in the EELS spectra of GO-PVA nanolaminates obtained in line-scan mode (see Chapter 5) can be used to distinguish between the three different domains present: 1) mainly graphitic (graphene-like; π + σ peak = 15.5 ± 0.5 eV[51]); 2) more oxidized (GO-like; π + σ peak = 18.0 ± 1.0 eV[52]); and 3) PVA-covered (π + σ peak = 21.0 ± 0.5 eV). As discussed in Chapter 5, the EELS line scan of a GO-PVA nanolaminate, obtained via STEM characterization, was interpreted as showing the preferential adsorption of PVA to the oxidized domains of GO.

Nanomechanical Characterization

Contributions and credit: **Mr. Rafael A. Soler-Crespo** and **Dr. Xiaoding Wei** conducted nanomechanical experiments, and **Ms. Lily Mao** assisted in thickness characterization and analysis.

The preparation and characterization of materials, as discussed in the previous section, permitted a thorough nanomechanical characterization of GO and GO-based systems. To achieve

this goal, two key efforts were required: i) thickness characterization to appropriately scale the observed properties and, ii) nanomechanical characterization using AFM tools. In this section, each of the aforementioned experimental procedures is described in detail. Combined with the previously described materials characterization, the efforts in this Chapter led to the understanding of the fundamental behavior of GO and GO-based materials, which we anticipate will become a key foundation in the application of GO towards engineered systems.

Thickness Characterization via AFM

The characterization of GO and GO-based material thicknesses served a two-fold purpose: first, it allowed identification of regions where suspended membranes were available for mechanical testing and, second, it revealed the thickness of the material to identify the number of stacked layers, which we found agreed closely with previous reports for GO monolayers[53]. Importantly, the thickness of the membranes is crucial in scaling up the mechanical properties of the probed specimens[15], and in identifying the thickness of polymer chains deposited on GO membranes (see below). Thus, atomic force microscopy (AFM) images of supported or suspended nanosheets were obtained in tapping mode using a Park XE-120 AFM system (Park Systems, South Korea) and a Veeco Dimension 3100 AFM system (Plainview, NY), respectively. To obtain the images, a single-crystal diamond probe (catalog number: ART D160, K-TEK Nanotechnology, Wilsonville, OR) was used to scan regions where membranes were visible via optical microscopy, and that were independently corroborated to contain GO or GO-based membranes by employing scanning electron microscopy (SEM). A scan rate of 0.5-1.0 Hz was used to collect images in the range of 2 x 2 μm^2, up to 20 x 20 μm^2. A 1:2 ratio was employed between proportional and integral grains, respectively.

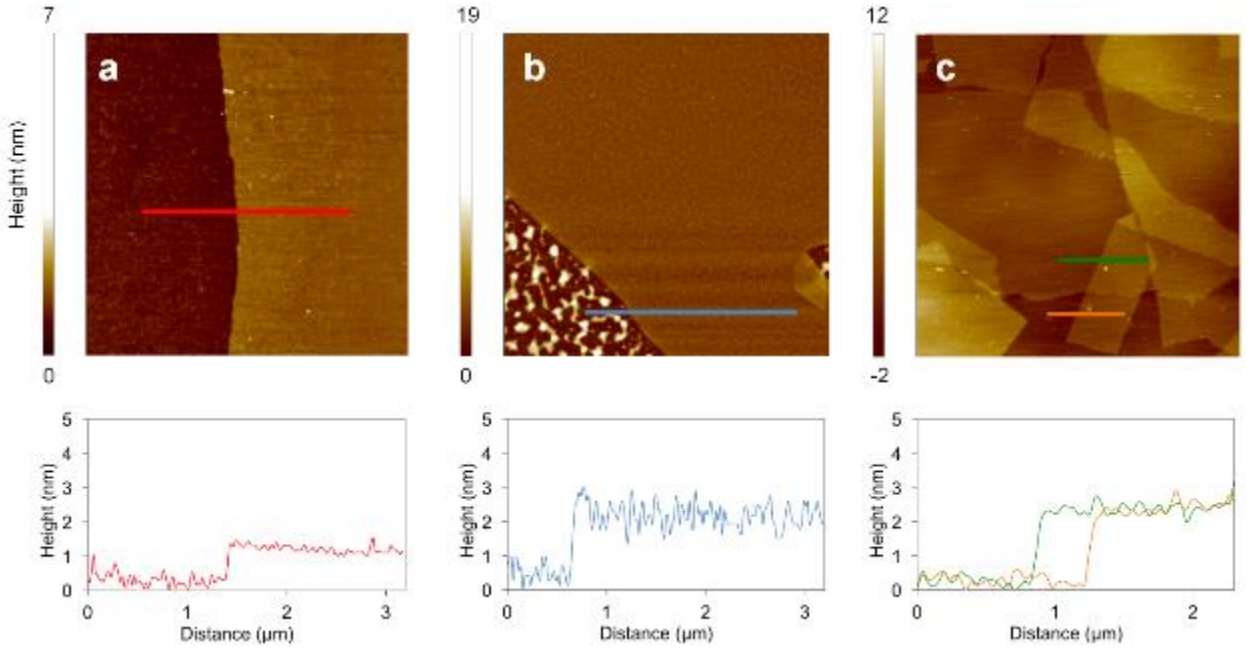

Figure 8. AFM characterization of GO nanosheets and nanolaminate systems. **a,** GO nanosheet, with a height of ~1 nm. **b,** GO-PVA nanolaminate, with a height of ~2.5 nm. The height variation of the nanolaminate is due to the microscale PVA network on the surface of GO. **c,** PVA-GO-PVA nano- and bi-nanolaminates. PVA-GO-PVA nanolaminates on both Si (orange line) and another nanolaminate (green line) exhibit a height of ~2.5 nm; as such, the bi-nanolaminate is expected to have a thickness of ~ 5 nm.

Comparing AFM thickness measurements of GO nanosheets before and after PVA modification revealed an increase in thickness, indicating the successful adsorption of PVA chains onto GO. Unmodified GO nanosheets have a thickness of about 1 nm (Figure 8a), in good agreement with previous reports[36, 53-54]. After Langmuir-Blodgett deposition of an ultra-thin layer of PVA onto GO nanosheets (see Chapter 2), the thickness of the resulting GO-PVA nanolaminates is around 2.5 nm (Figure 8b), suggesting that the layer of PVA on GO is about 1.5 nm thick. Compared to GO, the increased local height variations on the GO-PVA nanolaminate surface are attributed to the discontinuous microscale PVA network on GO, as further discussed in Chapter 5. In contrast, the local surface height of the PVA-GO-PVA nanolaminates is more uniform, despite having similar measured thickness as the GO-PVA nanolaminates (about 2.5 nm; Figure 8c, orange line). This is due to the difference in fabrication process: PVA-GO-PVA nanolaminates were

produced by spin-coating a premixed solution of GO and PVA, rather than Langmuir-Blodgett deposition (see Chapter 2), which presumably results in more homogeneous PVA coverage at the microscale.

In addition, an even thinner PVA layer can be achieved by spin-coating, as PVA chains adsorb to both faces of GO nanosheets within the premixed solution. This implies that the PVA layer on each face is only about 0.75 nm thick. Therefore, bilayer PVA-GO-PVA nanolaminates comprising a stack of two PVA-GO-PVA nanolaminates should have a thickness of around 5 nm. As seen in Figure 8c (green line), the thickness of a PVA-GO-PVA nanolaminate stacked on top of another PVA-GO-PVA nanolaminate is about 2.5 nm, suggesting that the entire bilayer assembly does indeed have a thickness of around 5 nm. Together, the AFM measurements clearly show the presence of PVA on GO nanosheets and confirm that the employed fabrication methods can achieve ultrathin (~0.75-1.5 nm) PVA layers on GO, and also validates the thickness of GO and GO-based materials in light of their nanomechanical characterization.

AFM Membrane Deflection Experiments

The geometry of 2D materials presents a number of challenges when developing protocols for probing mechanical properties. In contrast to 1D nanomaterials, such as CNTs, the membrane-like configuration of 2D materials raises significant issues with sample manipulation, making direct uniaxial tensile assessment of mechanical properties problematic. The development of experimental techniques which are capable of probing the mechanical properties of 2D materials remains a significant challenge for the research community. A typical characterization methodology implemented in the assessment of 2D mechanical properties relies on atomic force microscopy (AFM) based deflection experiments performed on monolayer films deposited on a

holey substrate, as detailed in Lee *et al.*[15] This technique is advantageous as it does not require a direct isolation and manipulation of monolayer films, but rather uses high-throughput deposition techniques to place films directly onto the holey substrate and provides significant information about mechanical properties and deformation pathways.

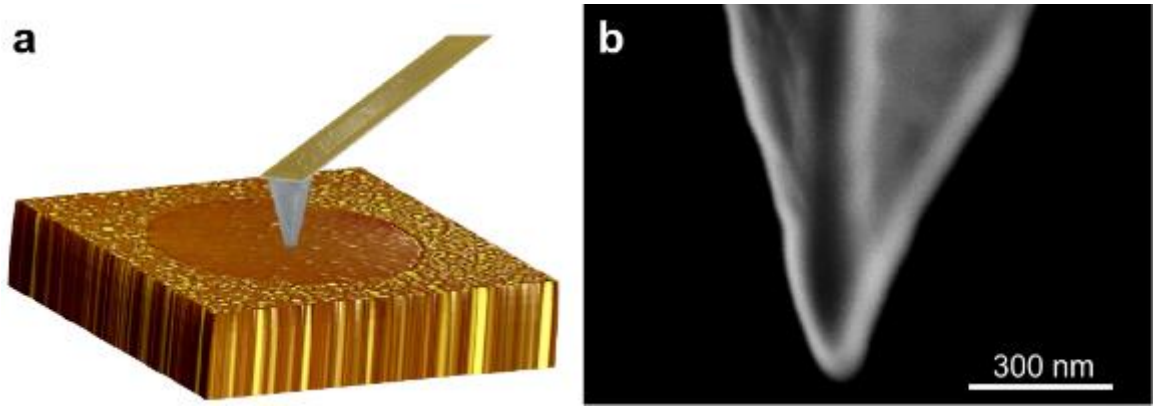

Figure 9. AFM membrane-deflection experiment methodology. a, Schematic of AFM membrane-deflection test on a suspended circular GO membrane. **b,** Scanning electron micrograph of a representative AFM tip.

To characterize the mechanical properties of GO and GO-based materials manufactured in this thesis, we employed AFM microscopy to conduct membrane deflection tests using a protocol similar to that described by Lee *et al.*[15] Briefly, a single-crystal diamond probe (catalog number: ART D160, K-TEK Nanotechnology, Wilsonville, OR) was used to indent the center of suspended membranes with an AFM (Dimension 3100, Veeco, Plainview, NY), as shown in Figure 9a. The stiffness of the used cantilevers (k = 3.00-10.00 N m^{-1}) was calibrated using a standard cantilever (CLFC-NOBO, Bruker) and accepted methods in the literature[55]. The tip radius of the AFM probes (R = 15-25 nm) was measured by an FEI NovaNano 600 SEM, as shown in Figure 9b. All experiments were performed at room temperature and 16% humidity inside a customized environmental chamber. A constant deflection rate of 1μm s^{-1} was used in all experiments.

For a suspended, circular, linear elastic membrane under a central load, the force vs. deflection response can be approximated as[15]

$$F = \pi\sigma_0 h\delta + \frac{Eh}{q^3 a^2}\delta^3 \quad (1)$$

where F is the applied force, δ is the membrane center deflection, h is the effective thickness of the specimen as measured using AFM thickness characterization (see Chapter 2), σ_0 is the prestress in the membrane, a is the membrane radius, E is the elastic modulus, and q is a dimensionless constant defined as $q = (1.05 - 0.15\nu - 0.16\nu^2)^{-1}$ where ν is the Poisson's ratio. We chose a Poisson's ratio of 0.2 based on DFTB calculations performed for Chapter 3, which is also consistent with that employed for graphene[15]. We also defined specific guidelines, described below, to select the fitting region on the raw data to achieve consistency when fitting and comparing the linear elastic behavior of different samples.

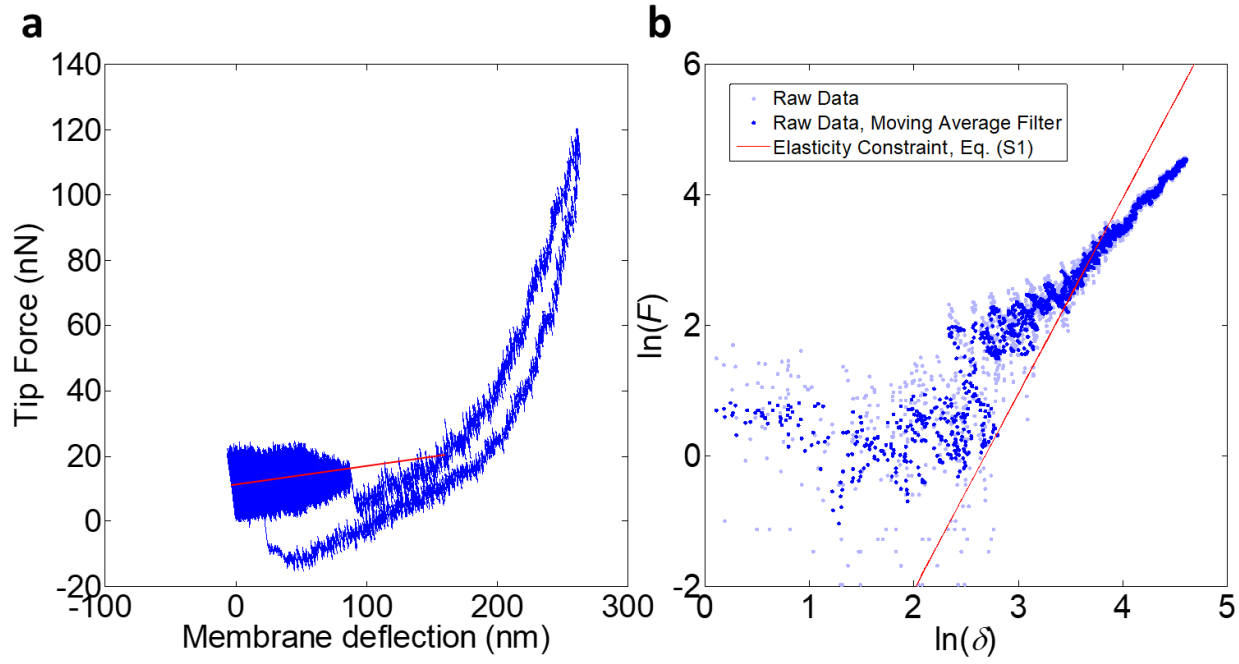

Figure 10. Selection of region to be fitted based on linear elastic, membrane deflection model. a, Selection of first point for fitting the AFM force-deflection curves. This point corresponds to the deflection value when the tip effective force, post-membrane adhesion (*i.e.*, after the cantilever straightens after snapping into the membrane),

matches the average value force measured during tip approach. **b,** Selection of the last point for fitting the AFM force-deflection curves, when the experimental data deviate from the value of the slope given by Equation (2).

As previously alluded to, and to consistently fit AFM force-deflection curves obtained from different samples, a set of criteria was established for selecting the region of the curve to be fitted using the linear elastic, membrane deflection model[15]. Based on these criteria, the first point of the fitted region is selected as the point at which the force in the AFM cantilever matches the average force measured as the tip approaches the membrane as shown in Figure 10a. This is the point where the force on the cantilever is zero post-membrane adhesion (*i.e.*, after the cantilever straightens after snapping into the membrane), the adhesion and deflection forces are balanced, and the tip effective force is zero. This selection is reasonable because adhesive effects are eliminated from the fitting process and only loads applied directly on the membrane by the AFM tip are considered. The final point of the fitted region is chosen at first occurrence of non-linear behavior, as determined by manipulating the linear elastic membrane deflection model to the form

$$\ln F \approx 3 \ln \delta + \ln\left(\frac{Eh}{q^3 a^2}\right) \tag{2}$$

for large deflections (Figure 10b). Based on these two points, the force deflection-curves are then fitted to the linear elastic membrane deflection model using an in-house MATLAB code (Version 2012a, MathWorks).

It is noteworthy, from the properties estimated during the analysis of Chapter 5, that the elastic moduli of polymer-covered GO materials is lower than that of GO and in agreement with the rule of mixtures (ROM)[1], attributable to the significant volume fraction occupied by the soft PVA component. As all of the nanolaminate samples probed in Chapter 6 contained equivalent volume fractions of GO and PVA, it is reasonable to expect that their elastic moduli should remain constant under the ROM framework. In terms of the performed analysis, membrane deflection

theory is unable to model the experimental results as the number of layers in the system increases and the measurements approach plate bending theory. In this light, and given that PVA-GO-PVA bi-nanolaminates consist of 6 total material layers, we assume that membrane deflection theory still holds given: i) the low stiffness of PVA[56-59], *i.e.*, the indentation is effectively over two stiff GO layers, and ii) the cubic nature of the force-deflection behavior measured experimentally, *i.e.*, force-deflection is linear when plate bending is dominant[60]. Given our assumptions, the 2D elastic modulus of PVA-GO-PVA bi-nanolaminates should follow the modulus scaling relation $E_{2D,n} = nE_{2D}$, since the 2D modulus of a system containing n layers of 2D elastic modulus E_{2D} should be $E_{2D,n}$. Interestingly, the highest prestresses measured herein for GO-PVA nanolaminates (0.06 GPa $\pm$ 0.03 GPa) are much lower than those previously found for GO (0.7 $\pm$ 0.3 GPa)[11], suggesting that PVA can induce significant lattice relaxation within the GO sheets. This systematic characterization of the properties of GO and GO-based materials led to the discovery of the fundamental behavior of the probed systems, which then inspired the analysis shown in Chapter 6.

Theoretical Analyses

Contributions and credit: **Mr. Rafael A. Soler-Crespo** led all theoretical analysis efforts, **Mr. Hoang Nguyen** co-led the development of the GO-polymer crack bridging model and assisted in performing molecular dynamics calculations, and **Mr. Xu Zhang** assisted in performing molecular dynamics calculations.

As previously alluded to, materials synthesis and nanomechanical characterization yield interesting insight into the mechanistic behavior of materials. However, these methods cannot describe, without a series of assumptions, the deformation and molecular mechanisms that occur

during experimentation. Furthermore, given the lengthy and laborious nature of producing and characterizing materials, it is impractical to develop the next generation of structural materials and engineered devices using experiments; indeed, this is the key vision of the Materials Genome Initiative, which sets to push forward the predictive capability and use of theoretical tools in materials discovery. With these arguments in mind, a central portion of this thesis work centers around the application of theoretical tools to validate experimental observations and discover fundamental knowledge, which can then lead to design rules and principles in the design of materials. This section describes the employed theoretical tools for the work herein.

Configurational Bias Monte Carlo Implementation for GO Monolayer Generation

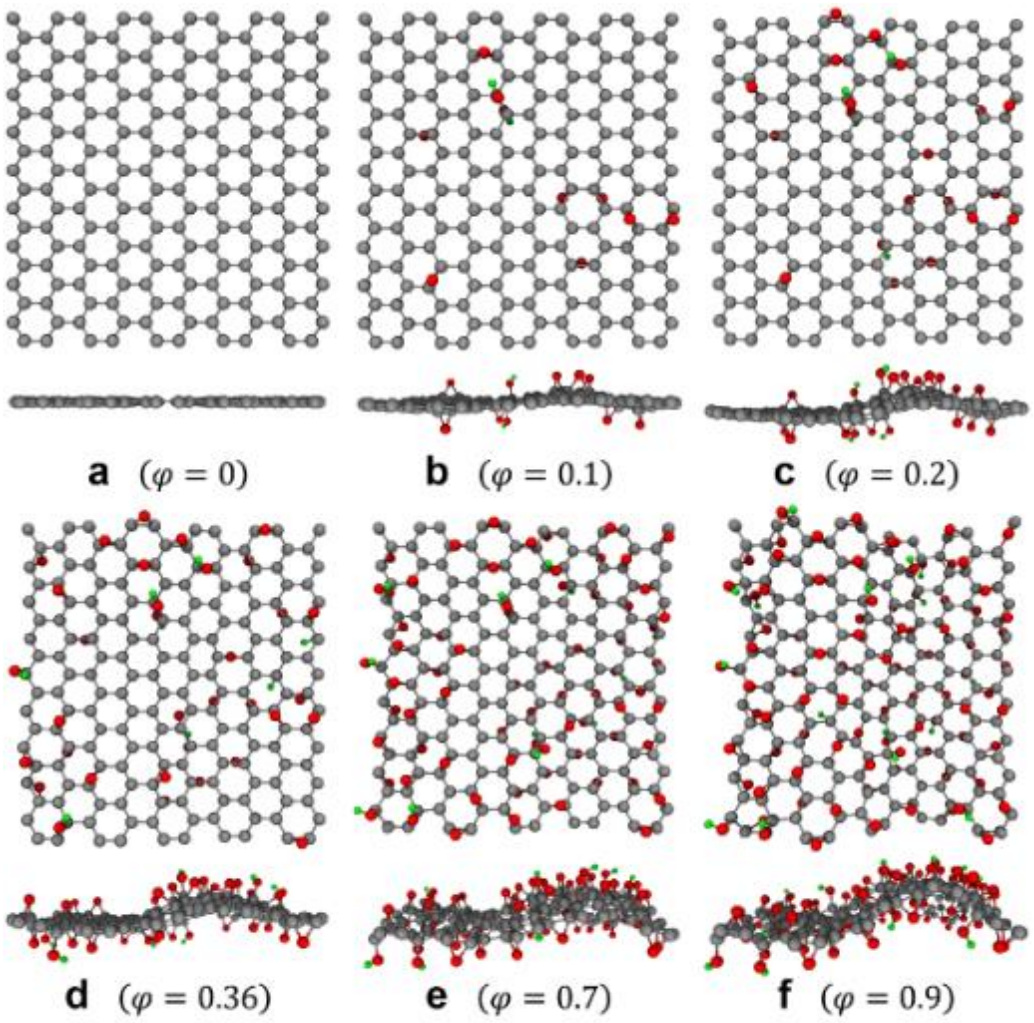

Figure 11. Top and side views of computationally generated models for graphene and GO, as shown along the armchair direction. a, Graphene (with 0% oxygen coverage, *i.e.*, $\varphi = 0$). **b-f,** GO with 10 ($\varphi = 0.1$, (**b**)), 20 ($\varphi = 0.2$, (**c**)), 36 ($\varphi = 0.36$, (**d**)), 70 ($\varphi = 0.7$, (**e**)), and 90 ($\varphi = 0.9$, (**f**)) % oxygen coverage. Gray, red, and green beads represent carbon, oxygen, and hydrogen atoms, respectively.

The configuration of functional groups in GO has great impact on the modeling results, as discussed in previous literature[28, 61-65]. Thus, having physically meaningful GO models that can represent the behavior of realistic GO monolayers is important. Herein, the generation of GO models was carried out using a modified version of the algorithm developed by Paci *et al.*[28] While thermodynamics typically favors the formation of low-energy structures over those of high energies during chemical reactions, the strongly oxidative conditions involved in the synthesis of

GO are more conducive for functional groups to form stochastically (*i.e.*, kinetically driven) regardless of the relative energy associated with different oxidation pathways. In light of this, a configurational-bias Monte Carlo algorithm was modified to introduce a range of functional groups on a graphene sheet to account for both thermodynamically and kinetically driven oxidation processes[28]. The implemented algorithm (with codes provided in Appendix A-C) comprises

1. A graphene sheet is generated employing open source solutions, or the code provided in Appendix A.
2. Functional group atoms are added through a Monte Carlo addition scheme that considers all possible functionalization sites. *N* independent and partially oxidized sheets are generated by adding *A* hydroxyl and *B* epoxide functional groups (one half to each side of each sheet). Epoxide oxygen atoms are placed at a vertical distance of 1.24 Å with respect to the graphene basal planes, and at the midpoints of the lines joining two adjacent carbon atoms. Initially, hydroxyl oxygen atoms are placed at a vertical distance of 1.43 Å over carbon atoms, and its associated hydrogen atoms are placed at a vertical distance of 0.95 Å over those oxygen atoms. The final, optimal C-O-H bond angles are obtained via geometry optimization. To fully explore the oxidation pathways, it is beneficial to keep *A* and *B*, which must be positive even integer values, as low as possible.
3. Each of the *N* sheets is subjected to geometry optimization and stress relaxation using a preferred computational technique. This methodology guarantees extraction of energy from stress-free initial structures and represents the most significant modification of the algorithm proposed by Paci *et al.* Structures obtained by performing geometry optimization alone were found to contain compressive stresses on the order of 3 GPa, which bias

optimization results, leading to inaccurate system minima and the artificial elimination of oxidation pathways via a configurational bias Monte Carlo approach.

4. For each of the *N* sheets, the Rosenbluth factor p_j is calculated using

$$p_j = \exp \frac{-\beta E_j}{\sum_{i=1}^{N} \exp(-\beta E_i)} \quad (3)$$

where

$$\beta = \frac{1}{k_B T_{art}} \quad (4)$$

Here, p_j is the probability of observing the *j*th sheet naturally, E_j is the minimized energy of the *j*th sheet, E_i corresponds to an energy sum over all the *N* generated GO models, k_B is Boltzmann's constant and T_{art} represents an artificial temperature value utilized to weight the effect of temperature in minima selection. This method, known as Rosenbluth sampling, is akin to Boltzmann distributions in statistical mechanics. The artificial temperature, T_{art}, is chosen to be 300 K, the temperature at which membrane-deflection experiments in this study were carried out. The main contribution of T_{art} is to shift the energy comparison reference temperature, to prevent numerical artifacts with the evaluation of typically very small exponential factors.

The Rosenbluth factor for each of the *N* sheets is compared to a random number in the range [0, 1]. This process results in the selection of *M* structures ($M < N$) to be further oxidized, and allows structures with relatively high energies to exist while biasing the selection to structures with relatively low energies[28], as per thermodynamic principles.

5. An additional number of *A* hydroxyl and *B* epoxide functional groups are added (one half to each side of the sheet), resulting in *N* independent sheets from each of the *M* structures.

Then, geometry optimization and stress relaxation was carried out on each of the $M \times N$ sheets and the Rosenbluth factor is calculated.

6. GO sheets with varying chemical composition and degree of oxidation are generated by repeating steps 2-5. In this framework, the ratio of *A* and *B* controls the relative amount of each type of functional groups, *i.e.*, the epoxide-to-hydroxyl functional group ratio, while the magnitude of *A* and *B*, and the number of times that steps 2-5 are repeated, controls the overall degree of oxidation in the representative GO monolayer.

This approach means the GO models generated in this study are disordered and energetically favorable. As an oxygen atom is covalently bound to two carbon atoms in an epoxide group and to one carbon atom in a hydroxyl group, the fraction of oxidized carbon atoms, φ, for each GO model can defined by

$$\varphi = \frac{N_{Carbon,oxidized}}{N_{Carbon,total}} = \frac{2N_{Oxygen} - N_{Hydrogen}}{N_{Carbon}} \quad (5)$$

Top and side snapshots of the relaxed configuration of typical GO models as a function of increasing φ, obtained using the algorithm described above with a 4:1 epoxide-to-hydroxyl functional group ratio, are shown in Figure 11. Models with φ = 0, 0.1, 0.2, 0.36, 0.7, and 0.9 were generated to represent a range of oxidation levels potentially attainable in GO sheets. Specifically, the model with 70% oxygen coverage is consistent with the analysis reported by Marcano *et al.* (69% oxidized C)[34]. After the sheets were geometry-optimized, and the residual stresses eliminated, the microstructures of the models were quite comparable to the Lerf-Klinowski model of GO[46-47] where hydroxyl and epoxides were the dominant functionalities. The placement and directionality of functional groups in our model is consistent with various reports in the literature[18, 47, 52, 62, 64-66]. Specifically, we capture two reported observations. First, hydroxyl groups that appear

on the same side of the basal plane are para-positioned (*i.e.,* on opposite sides of the same hexagonal ring). On the other hand, hydroxyl groups on opposite sides of the basal plane are either meta- or ortho-positioned (*i.e.,* the second hydroxyl group is present in any of the carbon atoms that is not opposite to that bearing the first hydroxyl group). For $\varphi \geq 0.70$, a small number of carbonyl, oxetane, and ether groups were also observed, consistent with the reports of Erickson *et al.*[47] Also, we note that while Erickson *et al.* found evidence for the formation of islands of functional groups in sheets with $\varphi \approx 0.80$, we did not include this "islanding" phenomenon in our models, as the scale on which this is thought to occur is too large to be captured by our calculations[47]. Second, we observe that sheet waviness increases in our models with increasing oxygen coverage, as reported in experiments and computations[12, 67-69].

Density Functional-Based Tight Binding Tension Simulations and Analysis

To explore the effects of composition in the deformation and fracture mechanisms of GO, 2 x 2 nm^2 GO models with different compositions, *i.e.,* varying functional group ratios and degrees of oxidation as per the desired case, were prepared utilizing the configurational bias Monte Carlo algorithm presented in Chapter 2, which accounts for the stochastic oxidation process involved during sample synthesis[28, 38, 47]. Then, the generated models were subjected to a simulated, molecular mechanics (MM) based, displacement controlled tensile experiment by applying uniaxial strain tension along the armchair direction (*i.e.,* tensile strain was applied in the armchair direction, with the zigzag direction atoms held fixed). Simulations were performed employing the CP2K software package (https://www.cp2k.org/) utilizing the *mio-0-1* Slater-Koster parameter set and charge self-consistency[70], as implemented. Charges were treated utilizing a smooth-particle mesh Ewald (SPME) summation, with one grid point per Å. The Ewald convergence parameter

was set to 0.35, and a cutoff radius of 10 Å for the real-space forces was used. Displacements of the unit-cell boundaries were prescribed utilizing 0.5% strain increments between strain steps. Geometry optimizations were performed between each strain step. Stress measures were obtained by calculating virial stresses according to the virial theorem, as implemented in CP2K.

Further supporting simulations with the same models were also performed for validation and completeness, *e.g.,* to distinguish anisotropy and directionality dependence in the behavior of the functional groups, leading to a total of three different displacement controlled conditions: uniaxial strain tension along the i) armchair (*i.e.*, tensile strain was applied in the armchair direction, with the zigzag direction atoms held fixed) and ii) zigzag directions, and iii) equibiaxial strain tension. Simulations were performed by following the same method outlined previously.

In addition to DFTB simulations, we also applied density functional theory (DFT) calculations to verify the DFTB method (see Chapter 4). All DFT calculations in this study were performed using the plane-wave-based Vienna Ab-initio Simulation Package (VASP)[71-72]. Projector augmented waves (PAW)[73-74] were used to represent ionic cores, and the electronic kinetic energy cutoff for the plane-wave basis describing the valence electrons was set to 520 eV. A 5 × 5 × 1 k-point mesh was used for calculations.

After obtaining the stress-strain response of various GO sheets utilizing the DFT and DFTB molecular mechanics simulations employed in this study, we extracted various mechanical properties of interest from the system. First, we were interested in extracting linear elastic properties, which can be estimated from knowledge of material elastic constants[15]. If a material is isotropic linear elastic, the following relationships hold:

$$E = \frac{C_{11}^2 - C_{12}^2}{C_{11}} \quad (6)$$

$$\nu = \frac{C_{12}}{C_{11}} \quad (7)$$

where E is the elastic modulus of the system, ν is the Poisson's ratio of the system and C_{11} and C_{12} are elastic constants.

For each of the uniaxial strain tension results obtained in this study, a set of elastic constants, C_{11} and C_{12} was determined through least-squares fitting of the initial part of the stress-strain curves (*i.e.*, low-strain regime). The two obtained constants determine an elastic modulus and Poisson's ratio along the strained direction independently. Non-linearities in the stress-strain curves at small strains, which arise mainly from increasing waviness in the system as the degree of oxidation increases, are intrinsic in the sheet due to their highly oxidized nature. To alleviate this artifact, stress-strain curves were linearized according to regions where the tangential slope became stable and shifted horizontally such that the linear extrapolation of the curves passed through the origin.

The toughness (Γ) of GO was computed by integrating the stress-strain curve, using the trapezoidal rule on the as-obtained data set, according to the definition:

$$\Gamma = \int_0^{\varepsilon_f} \sigma(\varepsilon) d\varepsilon \quad (8)$$

where ε_f is the failure strain of the material.

Chapter 3 also employs the use of room temperature DFTB-based MD. The simulations were carried out based on DFTB forces. A 0.5 fs time step, and the microcanonical ensemble were used. Temperature was maintained at 300 K with a Nose-Hoover thermostat and a thermostat

relaxation time constant of 25 fs. One picosecond of dynamics was performed between each strain increment. Tensile strains were applied using the same procedure outlined in the molecular mechanics simulation methodology, and the same analysis techniques were utilized to process the obtained stress-strain curves. The only MD simulation carried out in this thesis corresponds to equibiaxial tensile strain for a GO sheet with φ = 0.7 and a 4:1 epoxide to hydroxyl functional group ratio, which is representative of the material studied in this thesis.

Molecular Dynamics Simulations on GO-Polymer Crack Bridging: Extraction of Traction-Separation Behavior

To demonstrate the crack bridging behavior of polymer chains suspended over GO monolayers (see Chapter 5 and 6), it was necessary to develop a continuum mechanics formulation that describes the fracture process in GO-polymer membranes (see below). In particular, atomistic simulations proved essential to extract the traction-separation behavior of polymer chains, which led the continuum analysis. To this end, the Large-scale Atomic/Molecular Massively Parallel Simulator (LAMMPS) software package[75] was employed to carry out all-atom MD simulations as described in Chapters 5 and 6. The ReaxFF force field[16], as parametrized[76] for simulations with hydrocarbons and graphene oxide-based systems, was employed for all simulations described. Systems comprise a single polymer chain, with a contour length of 13 nm, suspended over two 2 x 7 nm^2 GO archetypical sheets, *e.g.*, GO sheets with a 70% degree of oxidation and a 4:1 epoxide to hydroxyl functional group ratio. For clarity, graphene is considered as a GO archetype with no oxidation in Chapter 6. An initial crack opening of 1 nm separates both GO sheets, and is connected only by the polymer chain previously described. Periodic boundary conditions were applied in the

x and y directions, and a timestep of 0.25 fs was employed to consider the vibrational frequency of H atoms present in PVA and GO.

The system was first equilibrated in an NVT ensemble at a temperature of 300 K for 250 ps. The total energy of the system was monitored until convergence is achieved during equilibration, before equilibrated structures are subjected to loading. Then, a displacement-controlled uniaxial tensile strain experiment is performed by deforming the simulation box along the polymer chain's axial direction in an NVT ensemble at 300K at a strain rate between $1x10^{10}$ and $1x10^{8}$ s^{-1}. Per-atom virial stresses for PVA and GO are independently calculated and summed, and subsequently averaged over all the atoms in each phase to obtain average virial stresses. Forces in the PVA chain are obtained by scaling virial stresses considering the polymer chain contour length. The effective crack opening is calculated by measuring the average distance between the atoms present in the GO crack edges.

To calculate the effective area of polymer chains deposited on GO membranes, four PVA chains (critical in the continuum analysis of PVA crack bridging, see below), 45 monomers in length and separated by a lateral distance of 0.5 nm, were suspended over two 2 x 7 nm^2 GO sheets, separated by an initial crack opening of 1 nm, with a 70% degree of oxidation and a 4:1 epoxide to hydroxyl functional group ratio. The system was equilibrated in an NVT ensemble at a temperature of 300 K for 250 ps. The total energy of the system was monitored until convergence is achieved during equilibration, before equilibrated structures were utilized for calculations. The end-to-end distance between PVA chains was calculated to obtain the effective area of PVA chains deposited over GO membranes – as required to estimate the energy release rate of GO-PVA nanolaminates (see below discussion).

Continuum Analysis of GO-Polymer Crack Bridging: Extraction of Composite and Fiber Energy Release Rates

To understand the magnitude of the crack bridging provided by the ultra-thin PVA network deposited over GO monolayers, which will be highlighted in detail in Chapter 5, concepts from fracture mechanics can be used to compare the energy release rate of GO and GO-PVA. In particular, it is well-established in the mechanics community that such bridging effects will result in a crack resistance curve[3]. The starting point of such a curve will be equal to the energy release rate of the matrix, *e.g.*, the supporting substrate for the fiber, or GO in this case. As the crack opens, and when this process reaches a steady state, the curve will plateau at a value that corresponds to the sum of the energy release rate contributions of the matrix and the crack bridging fibers. For GO-PVA, the crack bridging effect of PVA chains can be obtained by considering this plateau value. The total energy release rate of a system where crack bridging manifests, at steady state, is given by[3]

$$G = G_0 + G_f = G_0 + \int_0^{\delta_c} \sigma_t(\delta) d\delta \quad (9)$$

where G is the energy release rate of the composite system, G_0 is the energy release rate of the matrix (*i.e.*, GO) and G_f is the energy release rate of the crack bridging fiber (*i.e.*, the PVA chains). The energy release rate of the PVA chains, G_f, depends in turn on the crack opening δ and their tangential traction, σ_t.

In the derivation of the model, we assumed that: i) PVA chains have a random distribution in location and orientation, ii) the total length of all PVA chains is equal, and iii) the PVA chains are straight when suspended over a crack edge. Additionally, PVA chains are characterized based on the geometry shown in Figure 12a. The total chain length, L_f, and the embedded chain length, z, are critical components in determining the effective length of a PVA chain that can contribute to load bearing and provide reformable hydrogen-bonding with GO.

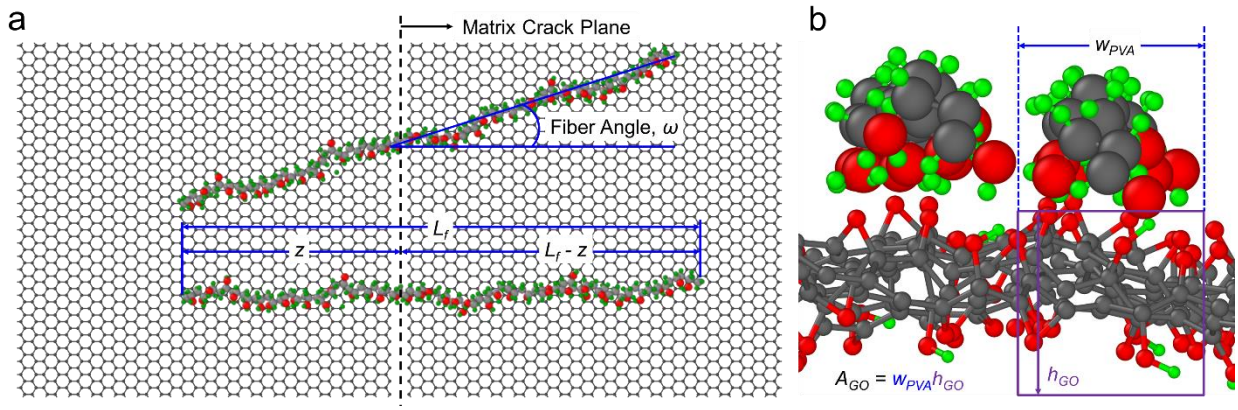

Figure 12. Geometrical definitions for model to estimate energy release rate of GO-PVA nanolaminate materials based on continuum mechanics. a, Schematic of top view of GO-PVA. GO functional groups are hidden for clarity. The geometrical definitions involved in the model are shown. **b,** Schematic of cross-sectional view of GO-PVA showing the definition of effective GO area. In the figure, gray, red and green beads represent carbon, oxygen and hydrogen atoms, respectively.

PVA chains can only be considered as crack bridging elements when subject to the condition $z \geq 0$. For uniform PVA chain lengths, the embedded length probability density function is assumed to be

$$p(z) = \frac{2}{L_f} \text{ for } 0 \leq z \leq \frac{L_f}{2} \tag{10}$$

Similarly, the probability density function for the effective PVA chain angle is given by

$$p(\omega) = \cos(\omega) \text{ for } 0 \leq \omega \leq \frac{\pi}{2} \tag{11}$$

where ω corresponds to the angle between lines normal to the matrix crack plane and a given PVA chain, and symmetry has been utilized to reduce the lower bounds of the system. Based on the molecular dynamics (MD) simulations performed to characterize the GO-PVA system (see previous sub-section and Chapter 5), and assuming that hydrogen bonding operates in an isotropic manner and that PVA chains with the same embedded length *z* have the same tangential traction-crack opening behavior, the stretching force on a PVA chain corresponds to an effective crack opening, δ_{ω}, which is given by

$$\delta_{\omega} = \frac{\delta}{\cos(\omega)} \tag{12}$$

To deduce the tensile behavior of the composite material, it is necessary to capture the tangential traction transmitted across the matrix crack by integrating the tangential traction contributions of each PVA chain over the aforementioned distributions, which corresponds to

$$\sigma_t = \frac{1}{A_{GO}} \int_0^{\pi/2} \left[\int_0^{L_f/2} t(\delta, z, \omega) p(z) dz \right] p(\omega) d\omega \tag{13}$$

where A_{GO} corresponds to the cross-sectional area of GO that is covered by a PVA chain (which can be obtained by calculating the coverage density of PVA chains in the system, see Figure 12b), *t* corresponds to the tangential traction-crack opening behavior of each individual PVA chain and *p* corresponds to probability distribution functions described above.

The MD calculations performed using ReaxFF, described in detail in Chapter 5 and summarized in Figure 13 for illustrative purposes, depict the tangential traction-crack opening behavior of a single PVA chain suspended over GO, and can be used to train a general model towards the numerical integration of Equation (13). The tangential traction-crack opening behavior

obtained from MD simulation results was fitted by an equation of the form $t = C_1\, atan(C_2\delta)$ as shown in Figure 13. For PVA chains, the fitting procedure revealed C_1 = 0.4033 nN and C_2 = 10.

The molecular weight of PVA chains used in Chapter 5 (6 kDa) contain approximately 130 monomers per chain and have a total chain length of approximately 34 nm upon full extension. To ensure the proposed model for the tangential traction-crack opening behavior is physically meaningful and agrees with the constraint enforced by Equation (10), then $L_f/2$ = 14 nm, providing a safety factor to account for PVA chain length distribution in the prepared samples, and to ensure the model does not over-predict energy release rates.

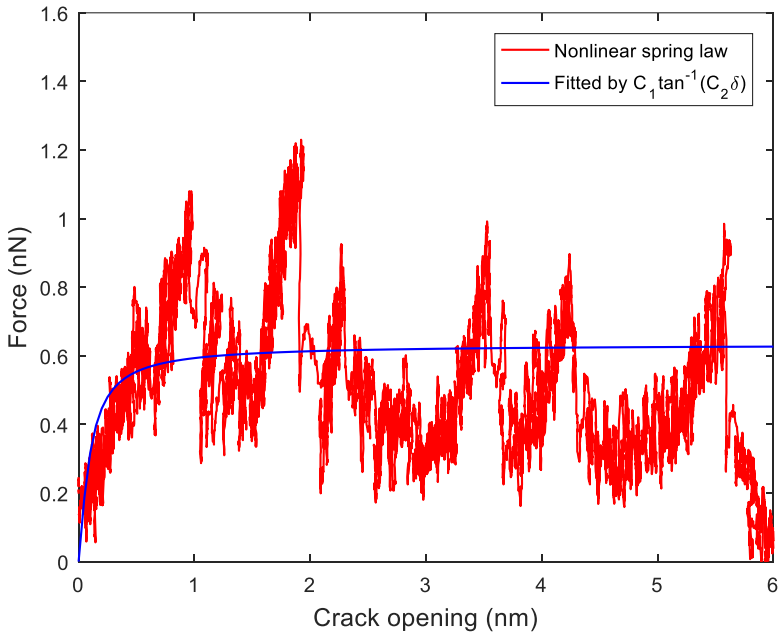

Figure 13. Tangential traction-crack opening behavior of a PVA fiber suspended over GO with a 1 nm crack opening as obtained from all-atom molecular dynamics response. Subsequently, the response is fitted by a mathematical model to approximate the tangential traction-crack opening law.

Based on the fitted traction-separation behavior (Figure 13), a number of scenarios are possible with different chain lengths. The most intuitive scenario occurs when the PVA chain lies completely on only side of the crack, leading to no observable bridging ($z < 0$). Notably, when z

is shorter than the critical length (z < 1 nm), the chain will experience a reduced number of hydrogen-bonding stick-slip events leading to a tangential traction determined by the model, and a short pull-out distance for the chain. However, when z exceeds the critical length (z > 1 nm), the chain will slide and be subjected to a significant number of hydrogen-bonding stick-slip events before being pulled out.

The model derived for the tangential traction-crack opening, when subjected to Equation (12) and based on the physics of the crack opening behavior, has the general form

$$t = t(\delta_\omega) \text{ for } \delta_\omega < z \tag{14}$$

$$t = 0 \text{ for } \delta_\omega \geq z \tag{15}$$

With this general form, the tangential traction of a PVA chain as a function of crack opening can be computed as

$$\sigma_t = \frac{1}{A_{GO}} \int_0^{\frac{\pi}{2}} \left[\int_{\delta/\cos(\omega)}^{L_f/2} 0.4033 \tan^{-1}\left(\frac{10\delta}{\cos(\omega)}\right) \frac{2}{L_f} dz \right] cos(\omega) d\omega \tag{16}$$

or equivalently

$$\sigma_t = \frac{2}{A_{GO} L_f} \int_0^{\pi/2} 0.4033 \tan^{-1}\left(\frac{10\delta}{\cos(\omega)}\right) \left[\frac{L_f}{2} - \frac{\delta}{\cos(\omega)}\right] cos(\omega) d\omega \tag{17}$$

Based on the composition of the system then L_f = 28 nm. Furthermore, based on ReaxFF MD simulations (Figure 12b) then A_{GO} = 0.480 nm^2, providing all the necessary values and enabling numerical integration to obtain the result shown in Figure 14.

The obtained tangential traction-crack opening shows an early development of the shear strength of PVA chains, making PVA chain crack bridging effective when the GO crack opening

is still small and preventing crack blunting in GO. In addition, the tangential traction-crack opening behavior of the composite material shows a gradual release of stress, resulting in a smooth transfer of stress between GO and PVA chains as load is developed. The decrease in stress arises from the reduction in overlap between PVA chains and GO surfaces, and rationalizes the reduction in stress with crack opening. These observations are consistent with the physical picture of crack bridging, and explain features observed in the experiments reported in Chapter 5.

Finally, to obtain a quantification of the increase in energy release rate of the composite material compared to GO, one can employ Equation (9). Numerically integrating the curve shown in Figure 14 reveals G_f = 9.43 nN/nm, comparable to G_0 (4.54-6.11 nN/nm[19]), leading to an energy release rate G for GO-PVA nanolaminates equal to 13.97 nN/nm, a three-fold increase in energy release rate when compared to GO only. Importantly, this calculation likely serves as a lower bound due to the simple geometry assumed for PVA chains, as they can likely interact with one another, and with GO, adapting a more complex morphology than the one assumed herein. Nevertheless, the numerical results are consistent with experimental and theoretical results reported in Chapter 5 and highlight the significant role that PVA chains have in delaying failure and stabilizing the mechanical behavior of GO.

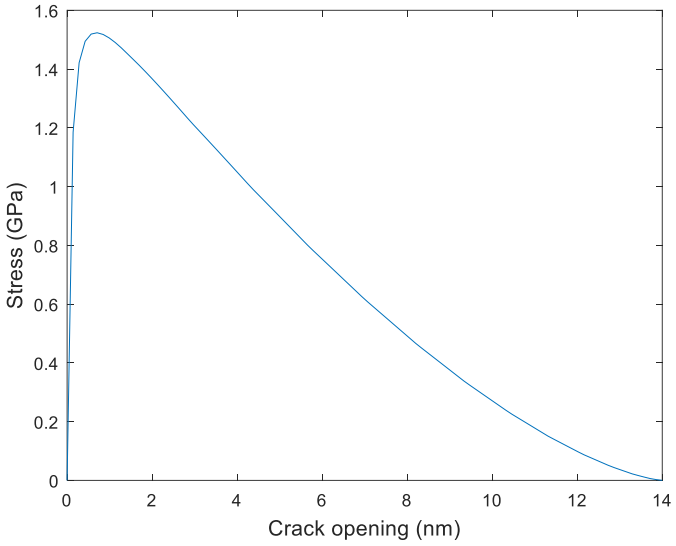

Figure 14. Tangential traction-crack opening behavior of GO bridged by PVA chains at the crack edge, by employing the model derived herein. Numerical integration of this tangential traction-crack opening law yields the energy release rate contribution of PVA chains, G_f.

Estimation of GO-PVA Fracture Process Zone

The failure of materials is intimately linked to their constitutive behavior and the length scales over which fracture processes take place[3]. Given this reasoning, and due to the observation of crack-bridging in GO-PVA nanolaminates (see Chapter 5), we desired to understand the length scale over which failure brittle failure was prevented by the deposited PVA chains. To achieve this fracture process zone estimation, the extended finite element methodology (XFEM)[77], as implemented in ABAQUS 6.14, was applied to model the fracture process in GO-PVA by considering the crack opening traction-separation behavior of GO and PVA. Plane-stress elements (CPS4) as implemented in ABAQUS 6.14 are utilized, with element size of 0.5 nm. To conduct our study, a 10 x 100 nm^2 GO sheet with a 2 nm long slit (represented as a strong discontinuity in the XFEM method) was designed. Simulations of GO, *i.e.*, no PVA is present, are conducted by imposing a linear elastic fracture mechanics failure criteria based on the critical energy release rate of GO[19] ($G_c = G_0$, G_0 ranges between 4.54-6.11 nN/nm). GO is assumed to behave as an isotropic,

linear elastic material with Young's modulus E = 220 GPa and Poisson's ratio ν = 0.2[11]. PVA is then implicitly considered in the system by including the traction-crack opening behavior produced after GO nucleates a flaw. To estimate the process zone, the traction near the crack tip is extracted after steady state crack growth is achieved. The process zone is defined as the distance over which load is being borne by the PVA traction-crack opening law, and is non-zero (see Chapter 5 for further details and results).

Chapter 3: Unusual Plasticity and Damage Tolerance in Graphene Oxide Monolayers

Contributions and credit: **Mr. Rafael A. Soler-Crespo** conducted the theoretical analysis, **Dr. Xiaoding Wei** experimentally measured the mechanical properties of GO monolayers, and **Ms. Lily Mao** synthesized and characterized all materials used.

Introduction

While single atomic layers with large lateral dimensions, such as graphene-based sheets, have attracted significant attention towards structural applications due to their high strengths and elastic moduli[15], their potential as a platform for exploring novel chemical transformations with nanoscale mechanical means has been unexplored. In theory, the combination of large area, tunable chemical functionality, and mechanical robustness should make these materials excellent complements to DNAs and proteins for exploring covalent bond-selective chemistry in two dimensions, extending our current knowledge of mechanically induced chemical transformations beyond these biopolymers, and hydrogen bonding and van der Waals interactions[78-79]. In particular GO, as an oxidized derivative of graphene, offers tremendous opportunity for directly probing how the supporting chemical functionalities on its basal plane, such as epoxide and hydroxyl groups, respond to mechanical perturbations at the atomic level. For example, these various oxygenated functional groups, which are traditionally treated as defects in the sp^2 network of the parent graphene sheet and deemed to have less robust mechanical properties[9, 80-81], would be more likely to respond to activation by mechanical forces without undergoing catastrophic failures.

Herein, we report that the chemical functionalities on GO can indeed confer damage-tolerant deformation mechanisms unattainable in graphene. While defect-free graphene exhibits brittle failure, the cyclic epoxide groups on GO help to dissipate strain energy and hinder crack

propagation through a novel epoxide-to-ether transformation, rendering the material ductile. This chemically induced plasticity in GO is verified through membrane-deflection experiments and rationalized by DFTB calculations. The findings reveal a unique relationship between the chemical structures and mechanical properties of GO at the atomic level, and demonstrate an example of mechanically activated covalent bond-selective chemistry of the epoxide groups that completely differ from its classical type of ring-opening reactions.

Results and Discussion

Mechanical Characterization

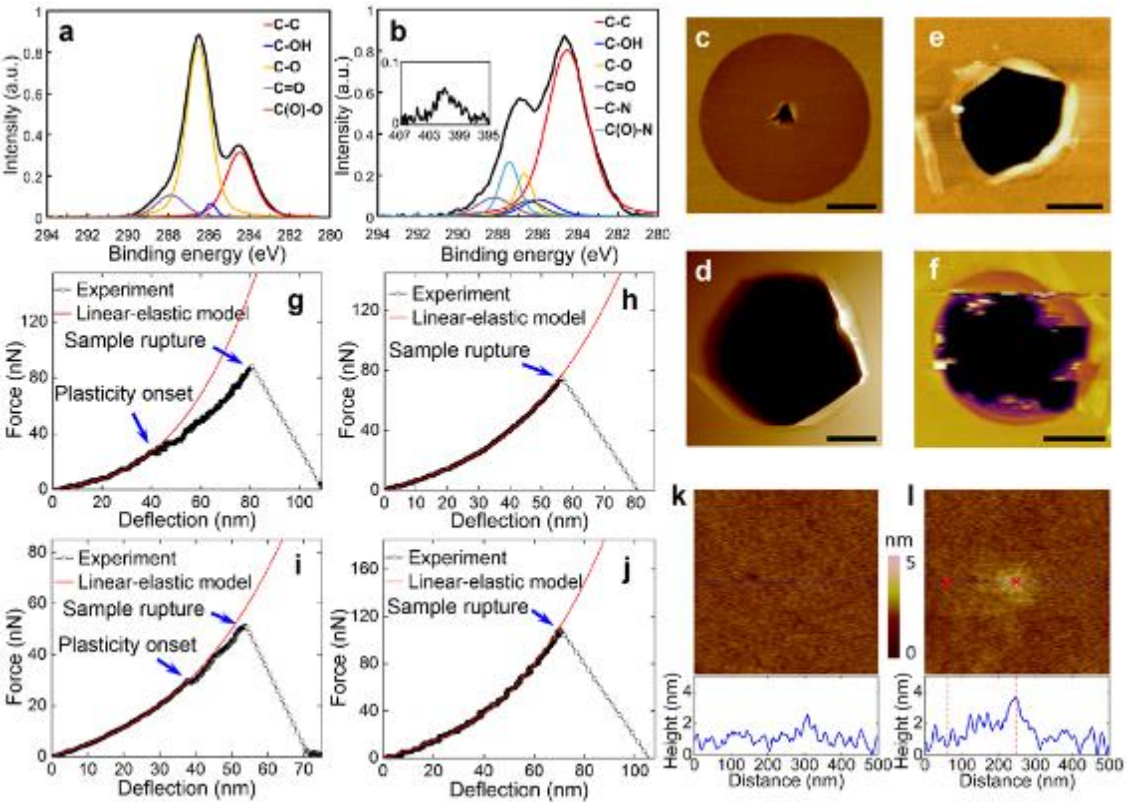

Figure 15. XPS and AFM characterization of GO and amine-modified GO (A-GO). a, **b**, C1s XPS spectra for GO **(a)** and A-GO **(b)**, respectively. Inset in (**b**) is the N1s XPS spectrum for A-GO. **c**,**d**, AFM topology images of ruptured monolayer GO (**c**) and A-GO (**d**) membranes after membrane-deflection tests, respectively. **e**,**f**, AFM topology images of ruptured pristine graphene and less-oxidized GO, respectively, after membrane-deflection tests (images adapted from [15] and [9]). **g**-**j**, typical ductile and brittle force vs. deflection curves for suspended GO (**g** and **h**) and A-GO (**i** and **j**) membranes, respectively. **k**-**l**, AFM scanning images of a 500 nm × 500 nm area at a suspended GO membrane center before (**k**) and after (**l**) testing. Scale bars in (**c**), (**d**) and (**e**) = 500 nm. Scale bar in (**f**) = 1 μm.

The GO nanosheets used in this work were synthesized using a modified Hummers method[34] (see Chapter 2 for details), and are extensively functionalized with epoxide groups based on X-ray photoelectron spectroscopy (XPS) analysis (Figure 15a, also see Chapter 2). To further confirm the epoxide-rich composition, we compared the XPS spectrum of the synthesized GO to two other previously reported materials with well-characterized composition: highly oxidized GO with predominantly epoxide groups[34], and GO with low oxidation level and predominantly hydroxyl groups[9] (Figure 16). We found the composition and C1s XPS spectrum of the synthesized GO to be very similar to those of the epoxide-rich material, and dramatically different from those of the epoxide-poor material. Employing Langmuir-Blodgett deposition[36], GO sheets are deposited over an array of circular microwells that were prefabricated on a silicon substrate (see Chapter 2). GO membranes are then tested utilizing AFM membrane deflection experiments, as described in Chapter 2. Figure 15g and h show the two types of force vs. deflection responses obtained for suspended GO membranes that correspond to ductile and brittle failure modes, respectively. In the ductile failure mode, the force vs. deflection response can only be fit to the linear-elastic membrane solution during initial stages of deflection, beyond which (approximately 40 nm) the suspended GO monolayer deforms inelastically until rupture. In contrast, linear-elastic behavior is observed throughout the deflection in the brittle failure mode. At the peak force, an abrupt increase in deflection occurred, indicating sudden film rupture.

Notably, only one suspended GO monolayer among the nineteen that were tested showed brittle failure, most likely due to the occasional large (*i.e.*, > 10 nm) defects in the basal plane of the GO nanosheet, which comprises relatively uniform, randomly distributed nanometer-sized domains of graphitic and oxygenated carbon atoms[38, 46-47]. A typical AFM image of the ruptured ductile GO monolayer (Figure 15c) clearly shows a localized puncture at the center, which is in

remarkable contrast to the catastrophic rupture of pristine graphene or less-oxidized GO containing mainly hydroxyl groups (Figure 15e and f)[9, 15]. The radius of the tear was approximately 150 nm, which is consistent with the dimension of the tip cross-section at maximum penetration, suggesting the presence of a unique crack-arresting mechanism in GO. This is confirmed in a second set of experiments, where the AFM tip was retracted quickly after reaching the maximum load but before membrane rupture. AFM images of these GO membranes before and after deflection clearly show a "damage" zone at the membrane center (Figure 15k-l), approximately 100 nm in diameter and 1-2 nm higher than the undamaged region, where the material underwent a severe plastic deformation.

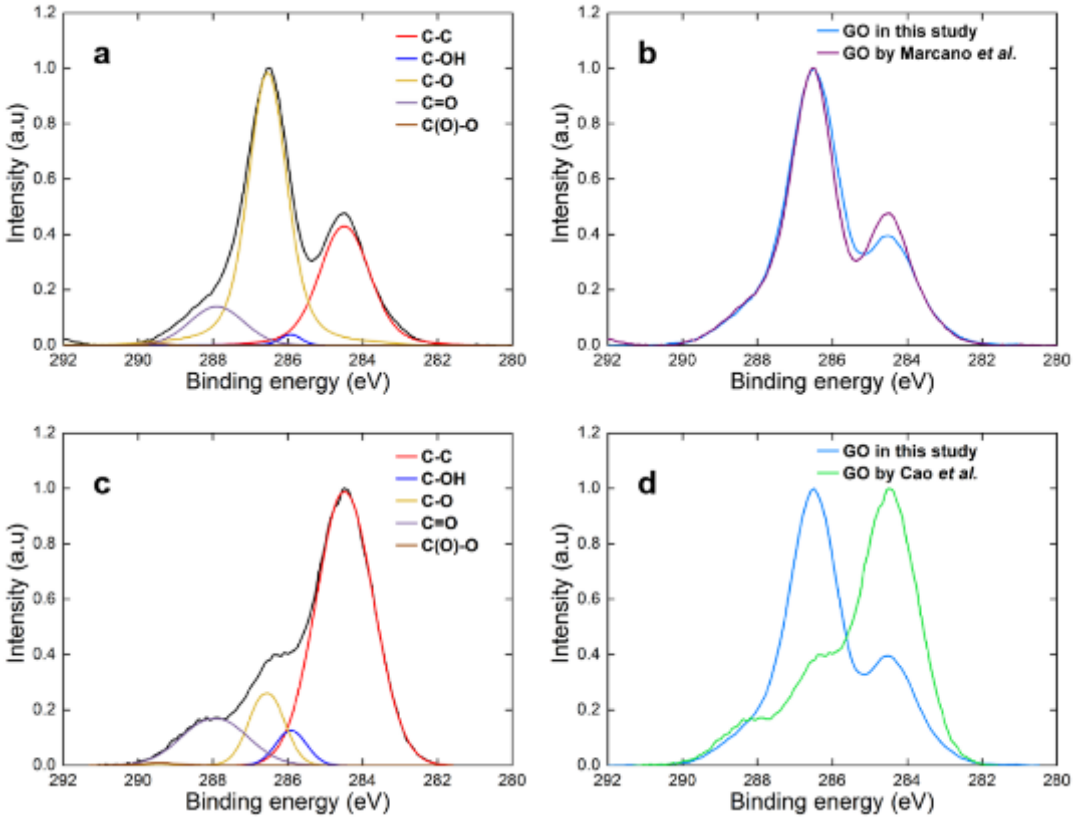

Figure 16. Comparison of C1s XPS spectra of different GO samples. **a,** Deconvoluted C1s XPS spectrum of Marcano *et al.*[34] **b,** Overlaid C1s XPS spectra of our GO and the GO of Marcano *et al.*[34] showing the similarity between the composition of the two materials. **c,** Deconvoluted C1s XPS spectrum of Cao *et al.*[9] **d,** Overlaid C1s XPS spectra

of our GO and the GO of Cao *et al.*[9] showing the clear difference between the composition of the two materials. Data shown in (**a-b**) was obtained from the authors, and data shown in (**c-d**) was digitized from the article.

Theoretical Analysis

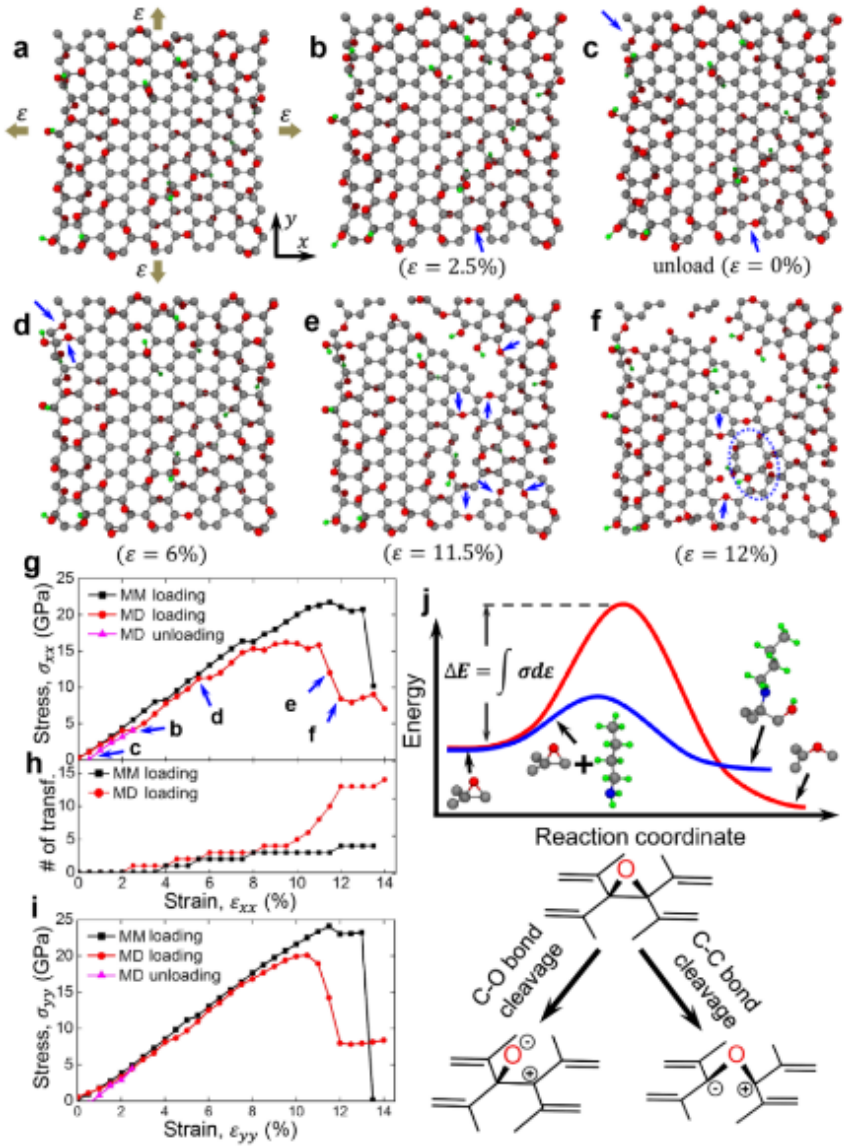

Figure 17. Density functional-based tight binding modeling of a 2 × 2 nm^2 GO sheet (φ = 0.7) subjected to equibiaxial tension. a-f, The first panel (**a**) shows the initial configuration of the GO sheet and the schematic of the constraints. Gray, red, and green beads represent carbon, oxygen, and hydrogen atoms, respectively. The subsequent panels (**b-f**) are the snapshots of the deformed GO sheet during molecular dynamics (MD) simulations. The dark-blue arrows highlight the locations on each snapshot where epoxide-to-ether transformations occurred. The dashed circle in snapshot IV highlights a Stone-Wales defect. **g**, Stress-strain curves in the armchair direction (x-axis in (**a**)) obtained from molecular mechanics and MD simulations. Labels in stress-strain curve refer to MD snapshot panels in Figure 17. **h**, Accumulated number of epoxide-to-ether transformations as a function of strain. **i**, Stress-strain curves along the zigzag direction (y-axis in (**a**)). **j**, An illustration of the relative energetic difference between the mechanochemically induced epoxide-to-ether transformation activated by strain energy (*i.e.*, C-C bond cleavage, red profile) and the epoxide ring-opening by *n*-butylamine (*i.e.*, C-O bond cleavage, blue profile). Gray, red, green and

blue beads represent carbon, oxygen, hydrogen, and nitrogen atoms, respectively. The chemical drawings beneath the profiles are included only to illustrate the key differences between the two chemical pathways without including all the relevant species (water, *n*-butylamine, etc.) that can be involved to facilitate the transformations. As such, the formal charges that are indicated on the drawings should not be taken literally.

To explore the origin of the experimentally observed plasticity, we modeled the tensioning of graphene and GO through a series of semi-empirical DFTB calculations using the open-source code CP2K (http://www.cp2k.org/) as described in Chapter 2. We first generated a molecular model of an approximately 2 × 2 nm^2 GO sheet with a functionalization level $\varphi = 0.7$ (defined as the fraction of oxidized carbon atoms). A 4:1 epoxide-to-hydroxyl functional group ratio was used to resemble the epoxide-rich composition confirmed by XPS analysis. A Monte Carlo based Rosenbluth sampling algorithm was employed to determine the favorable locations of the functional groups from random choices according to a Boltzmann-like distribution (see Chapter 2 for algorithm implementation, and Appendix A-C for employed codes). The obtained model shows excellent agreement with structural features previously reported for theoretically studied GO sheets in the literature[28, 61-65]. Then, we carried out molecular mechanics (MM) and molecular dynamics (MD) calculations to investigate the plasticity mechanism by applying equibiaxial tension on the nanosheet (Figure 17a) similar to the constraint on the material during membrane-deflection experiments. Uniaxial tension experiments were also conducted and analyzed to extract mechanical properties of GO.

As shown in Figure 17g, the stress-strain response of a GO nanosheet along the armchair direction shows strain bursts at 3.5% strain in MM (and 2% strain in MD) simulations that appear to correspond with a mechanochemical epoxide-to-ether transformation reaction (Figure 17b). This reaction, biased by strain energy (Figure 17j), activated at stress levels of 8.0 GPa in MM and 4.0 GPa in MD simulations, respectively. The lower stress obtained from MD (at 300 K) in comparison to MM (at 0 K) suggests that this strain-energy-activated mechanochemical

transformation is more favorable at ambient temperature, where the experiments were carried out. The ether groups that formed remained after unloading from 2.5% strain to 0% strain in our MM simulation (Figure 17c), confirming that this reaction is irreversible and deformation is plastic. In a previous report, using density functional theory (DFT), Li *et al.* studied graphene and carbon nanotube unzipping during oxidative processes[82]. They showed that a spontaneous epoxide-to-ether transformation would happen if multiple epoxide groups align on the opposite ends of benzene rings in the same side of the graphitic basal plane to form a linear fault line. However, this particular configuration of linearly aligned epoxy groups considered by Li *et al.* is only a transient state (*i.e.*, highly unstable), and is statistically unlikely in the case of the stable suspended GO membranes studied herein. The GO models generated in this study using the Monte Carlo algorithm suggest that this fault line of epoxide groups is energetically unfavorable in GO. Rather, our study reveals that epoxide groups in GO are randomly distributed and form a stable structure, in agreement with previous observations[28]. The epoxide-to-ether transformation occurs only when the GO sheet is under a substantial mechanical stress (between 4.0 and 8.0 GPa) and leads to improved material toughness. Thus, considering these essential distinctions, the scenarios discussed by Li *et al.* and herein are significantly different.

As strain increased, more epoxide-to-ether transformations accumulated; at 6% strain, a second major strain burst was observed in the MD stress-strain curve as the result of the strain energy release at the bond transformation locations (Figure 17d). At 9.5% strain, a nanoscale crack appeared in our simulation model (Figure 17e) but did not lead to a catastrophic failure of the material. Rather, it corresponds to a significant number of mechanically induced epoxide-to-ether transformations as the strain was increased (Figure 17h). The accumulation of these transformations led to a plateau in the stress-strain curve, indicating a delay in crack growth. At

the end of this plateau, crack growth led to a stress drop and failure. The transition captured in Figure 17e-f clearly shows that the epoxide-to-ether transformation at the crack front is responsible for energy dissipation, presumably due to the blunting of the crack front by the higher flexibility offered by the C-O-C angle in the newly formed ether group. At 12% strain, a void initiated near the crack tip, and a Stone-Wales defect, commonly observed during failure in graphitic materials[83], formed beside the void (Figure 17f).

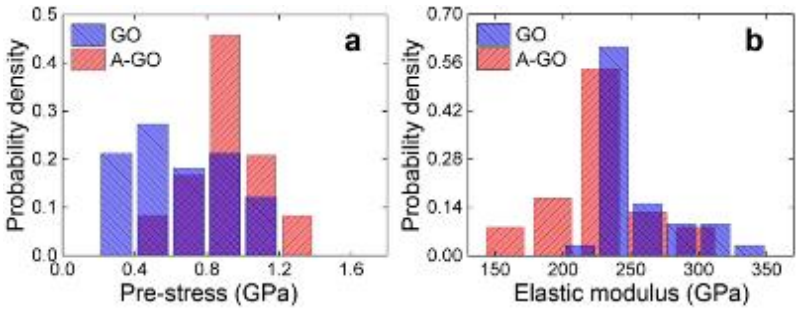

Figure 18. Derived prestress and elastic modulus values for GO monolayers. a, **b**, Histograms of prestress (**a**) and elastic modulus values (**b**) derived for GO and A-GO membranes.

As described above, the MD stress-strain curve shown in Figure 17g clearly demonstrates the plasticity and damage tolerance of GO when being tensioned in the armchair direction. In contrast, the corresponding stress-strain curve in the zigzag direction (Figure 17i) exhibits negligible plastic behavior, suggesting that the mechanochemical response to strain energy in GO is chirality dependent. Together, these results provide an unexpected explanation for the predominantly ductile failure mechanism in our experiment: As shown by the MD snapshots in Figure 17a-f, the novel epoxide-to-ether transformation that occurs on the basal plane of a GO nanosheet upon indentation can readily accommodate a network of nanoscale cracks and prevent it from catastrophic failure until these nanocracks coalesce. This is consistent with the experimental observation of a damage zone in GO membranes after testing (Figure 15l).

Amine Modification of GO Sheets

Our results thus far suggest that the epoxide-to-ether transformation in the basal plane of GO is the origin of the plasticity and the ductile-failure behavior that we observe in our experiments. Therefore, if the epoxide groups are removed such as through amine-induced ring-opening reactions[42], GO should show a more pronounced brittle-failure behavior. To prepare such samples, the GO monolayer-containing Si substrates were placed next to three drops of *n*-butylamine on a glass slide inside of a closed petri dish and left overnight. XPS characterization of the modified samples was carried out after membrane-deflection experiments were performed, and confirmed successful modification of the material (see below). In accordance with our hypothesis, when eighteen samples of *n*-butylamine-modified GO (A-GO) were tested, brittle failure was observed much more frequently than in the case of GO. Eight of the samples exhibited clear brittle failure (Figure 15j), and while the remaining samples showed a ductile-failure behavior, the degree of plastic deformation in them is significantly less than that in the GO membranes discussed earlier (*cf.* Figure 15i and 1g). Furthermore, the typical rupture topology of a suspended monolayer A-GO membrane that exhibited brittle failure (Figure 15d) showed features that are similar to those in pristine graphene and less-oxidized GO containing mainly hydroxyl groups (Figure 15e and f)[9, 15]. Together, these data support our assertion that the presence of epoxide groups, and thus the availability of epoxide-to-ether transformations, is responsible for the plasticity of the original GO samples. Presumably, the ring-opening reactions of the epoxide groups by *n*-butylamine[42], confirmed to occur via XPS (Figure 15a-b), have rendered A-GO more brittle.

The prestress and elastic modulus values of our GO and A-GO as derived from the elastic analysis of the experimental measurements (Figure 18) also support our conclusion. Assuming an effective GO thickness of $h = 0.75$ nm[53], the higher prestress in A-GO (0.9 ± 0.2 GPa) compared

to that for our original GO with φ = 0.7 (0.65 ± 0.3 GPa) suggests that amine modification did indeed increase membrane tension. We note that the value for our original GO was notably higher than that reported by Cao *et al.* (0.14 ± 0.02 GPa by assuming the same GO thickness h = 0.75 nm) with φ = 0.26, presumably due to stronger interactions between the basal planes of our highly oxidized nanosheets and the substrate. In contrast, the elastic modulus of A-GO is 223.3 ± 33.2 GPa, which is slightly lower than that of the original GO with φ = 0.7 (elastic modulus E = 256.4 ± 28.2 GPa; elastic modulus in two-dimensional (2D) form E_{2D} = 192.3 ± 21.2 N m^{-1}) as a result of the ring-opening of the epoxide groups. Both of these values are much lower than those reported by Cao *et al.* (E = 384 ± 31 GPa, E_{2D} = 269 ± 21 N m^{-1}) for a GO sample with φ = 0.26, suggesting that the elastic modulus for GO decreases with increasing levels of functionalization. This conclusion is further supported by the good agreement between our experimental measurements and the predicted elastic properties extracted from uniaxial tension DFTB calculations on GO nanosheets with various functionalization levels (φ = 0.1, 0.2, 0.36, 0.7, and 0.9) (Figure 19a and Figure 20). Furthermore, our DFTB simulations agree very well with DFT predictions by Liu *et al.* for disordered GO models at the same functionalization levels despite differences in functional group ratios (a 1:2 epoxide-to-hydroxyl group ratio was used by Liu *et al.*, evidently different from ours). In addition, we note with interest that the GO studied by Cao *et al.* (with a 20% functionalization level but a hydroxyl-rich composition) yields an elastic modulus also in agreement with our DFTB predictions for the GO model with a 20% functionalization level but an epoxide-rich composition. Therefore, we may reasonably assume that the elastic modulus of GO is mainly affected by the functionalization level, rather than by the relative proportions of different oxygen-containing functional groups. More specifically, the studies by Cao *et al.*, Liu *et al.* and this study contain the same relative amounts of sp^2- vs sp^3–type carbon-carbon bonding in systems

with the same functionalization level, independent of the relative amounts of each functional group present. Thus, one can reasonably expect that the electronic structure of the GO backbone dominates the measured elastic properties of the material, *i.e.*, the identity of the bonded functional groups does not directly influence the aforementioned elastic properties.

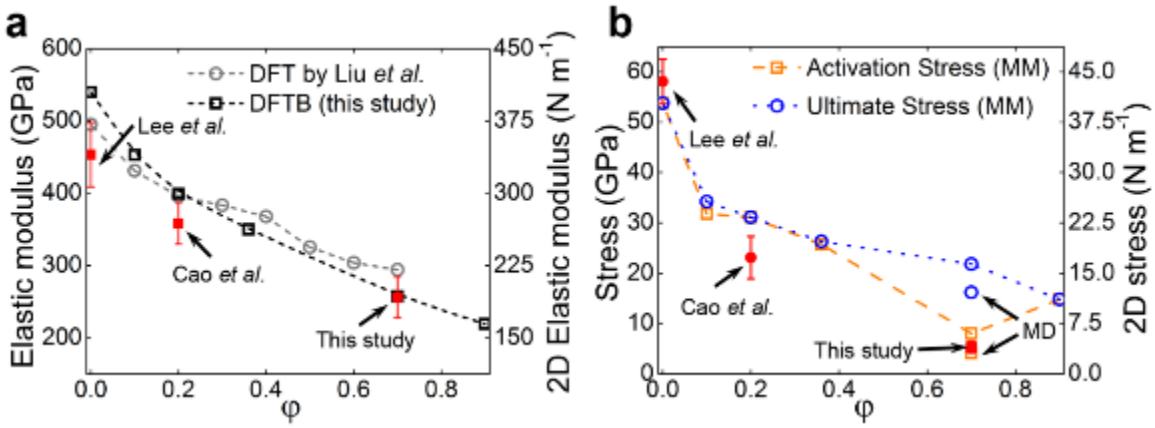

Figure 19. Elastic, plastic, and failure analysis of GO. a, Comparison of elastic moduli predicted by density functional theory (adopted from [63]) and density functional based tight binding (DFTB) for GO with increasing φ with experimental results for graphene (*i.e.*, $\varphi = 0$) from [15], GO with $\varphi = 0.2$ from [9], and GO with $\varphi = 0.7$ (this study). **b**, Comparison of ultimate and activation stresses predicted by MM with values reported for graphene (three-dimensional stress was converted by assuming a GO thickness of $h = 0.75$ nm), GO with $\varphi = 0.2$, and GO with $\varphi = 0.7$. Molecular dynamics predictions of ultimate and activation stresses for GO with $\varphi = 0.7$ are also plotted. Hollow and solid symbols represent DFTB predictions and experimental results, respectively. Error bars in (**a)** and (**b)** refer to standard deviations.

To further elucidate the extent to which epoxide groups, unlike hydroxyl groups, enable GO to deform plastically, we compared the fracture surfaces obtained by Cao *et al.* with those obtained in our study (with a 70% functionalization level and an epoxide-rich composition). Cao *et al.* experimentally showed that the fracture surfaces of hydroxyl-rich GO tend to be brittle. DFT simulations predict that, for membranes of this composition, brittle failure occurs along a path populated by hydroxyl-functionalized carbon atoms. In contrast, our studies show that epoxide-rich GO fails in a ductile manner. Our simulations suggest that crack propagation is hindered due to energy dissipation through epoxide-to-ether transformations. Thus, one can reasonably conclude that the presence of epoxide groups enables GO to exhibit plastic behavior.

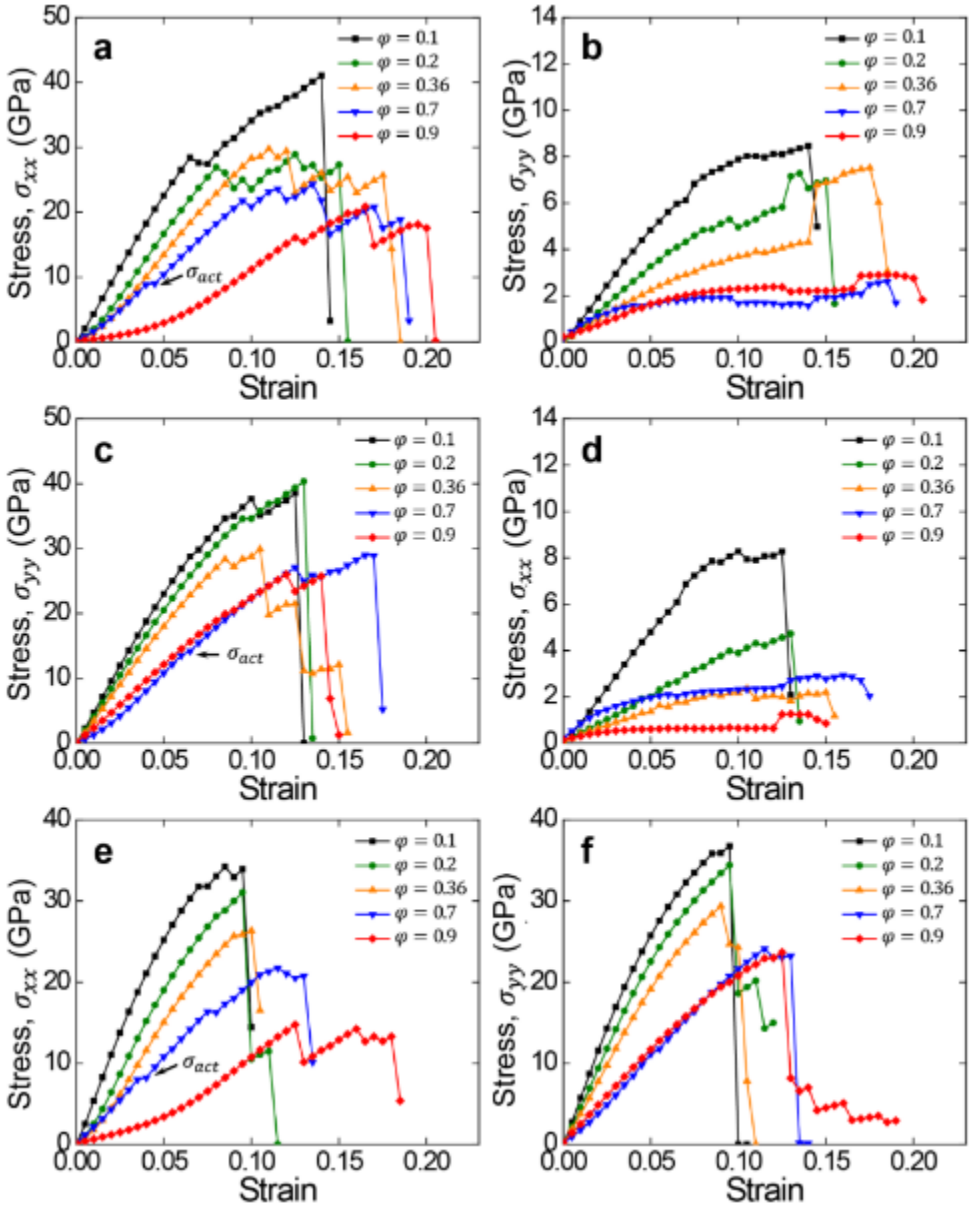

Figure 20. Stress-strain response of GO models as a function of oxygen coverage. a, b, Stress-strain curves along the armchair (**a**) and zigzag (**b**) directions during uniaxial strain tension along the armchair direction. **c, d,** Stress-strain curves along the zigzag (**c**) and armchair (**d**) directions during uniaxial strain tension along the zigzag direction. **e, f,** Stress-strain curves along the armchair (**e**) and zigzag (**f**) directions during equibiaxial tensile strain. Marked by arrows are the activation stresses when the first epoxide-to-ether transformation occurs in 70% functionalized GO under each constraint.

Analyzing the stress at the onset of plasticity allows us to further relate the material strength of GO with its level of functionalization. In contrast to the case of pristine graphene, which is nearly defect-free[15], it is impossible to define an "intrinsic material strength" for GO. Instead, we

used the term “activation stress” to describe the onset of the plastic deformation of GO, which is defined as the stress value at the membrane center when the sample is at the plastic onset point, the last data point where the material behaves linear-elastically (see Chapter 2). Since this is the first point in the stress-strain curve where plastic behavior begins, the activation stress is analogous to the yield stress in metals. Thus, using contact analysis in the linear elastic regime[84], the activation stress is given by

$$\sigma = \sqrt{\frac{FE}{4\pi hR}} \tag{18}$$

where F is the force at the plastic onset point and R = 25 nm is the tip radius of the AFM probe (as determined via SEM, see Chapter 2). The experimentally determined activation stress of a suspended monolayer GO is thus 5.3 ± 1.2 GPa (or 4.0 ± 0.9 N m^{-1}), consistent with the mechanical stress applied in our DFTB simulation at the point where epoxide-to-ether transformations were activated for a GO nanosheet with φ = 0.7. Given this good agreement, further equibiaxial tension simulations on GO samples with varying functionalization levels (Figure 20) then allow us to construct a relationship between the activation stress for the epoxide-to-ether functional group transformation and the material strength of these samples. In particular, the difference between the activation and ultimate stresses can now be used to indicate the extent of GO plasticity. As shown in Figure 19b, while the predicted ultimate stress for GO decreases monotonically with increasing φ, the activation stress decreases up to φ = 0.7 and then increases. This behavior suggests that while the level of plasticity in GO can be increased by increasing its propensity to undergo epoxide-to-ether transformations, its effect is countered by the loss of material heterogeneity for systems with φ > 0.7. Beyond this level of functionalization, further oxidization leads to the removal of graphitic domains (*i.e.,* loss of heterogeneity) so that higher strain energies are required

to activate mechanochemical reactions, and thus, loss of plasticity. This trend may also explain why this epoxide-to-ether transformation induced plasticity was not observed in previous experimental and theoretical studies of GO with either low functionalization levels or low epoxide populations[9, 28, 63]; sufficient functionalization levels and adequate epoxide populations are both needed for GO plasticity to become apparent.

Chapter Summary

In summary, we have established a molecular-level understanding of the unusual plasticity and defect-tolerant properties of suspended GO single layers through a synergistic combination of theoretical and experimental investigation. A novel epoxide-to-ether transformation was found to be responsible for the plasticity and ductility of GO as observed in AFM membrane-deflection experiments. In contrast to the thermodynamically favorable C-O bond-cleavage pathway for epoxide ring-opening in a molecular system, the mechanically actuated ring-opening reaction of epoxides supported on the 2D basal plane of GO actually proceeds through an alternative C-C bond-cleavage pathway. As an example of a rare, if not unprecedented, bond-selective chemical transformation achieved by mechanical activation, this reaction could be used to tune the mechanical properties of GO sheets by transforming epoxide groups to more stable ether groups. We are confident that this mechanochemical approach to studying the chemistry of graphene and its derivatives will stimulate the exploration of covalent-bond-selective chemistry in two-dimensional materials, beyond that offered by proteins and oligonucleotides.

Chapter 4: Atomically Tuning the Mechanical Properties of Graphene Oxide Monolayers

Contributions and credit: **Mr. Rafael A. Soler-Crespo** conducted the theoretical analysis, and **Dr. Wei Gao** conducted select DFT calculations to validate the DFTB potential and the generality of the DFTB observations.

Introduction

Graphene oxide (GO) has shown great potential for various applications in sensing[38, 85-87], energy storage[88-90] and the design of advanced structural materials[12, 26, 30, 58, 91]. While the nanostructure of GO was cause for scientific debate at first, theoretical and experimental evidence available at the time suggested that hydroxyl (-OH) and epoxide (-O-) functional groups dominated the bulk of the material, while carbonyl and carboxylic functional groups preferred to form near free surfaces at the edges of GO flakes[38, 46]. Recently, Erickson *et al.*[47] showed that graphene oxide possesses a graphitic backbone stochastically functionalized by functional group clusters, which form island-like patterns as previously predicted by Lerf and Klinowski[38, 46]. It is expected that surface functional groups on GO have considerable influence on the mechanical properties of the material, which is critical for potential GO applications. For instance, monolayer GO was found to have a lower Young's modulus and strength compared to unfunctionalized carbon based nanomaterials, such as pristine graphene and carbon nanotubes[9, 15, 63, 81, 92]. Moreover, it has been shown that both the Young's modulus and strength monotonically decrease as the degree of oxidation increases[63]. As more oxygen atoms become covalently bound to the carbon backbone, the electronic backbone structure becomes dominated by softer, weaker sp^3 bonding. For instance, introducing one epoxide group onto a pristine graphitic backbone would transform two carbons from sp^2 to sp^3 bonding, while the same effect results from bonding two carbons with a pair of

hydroxyl groups. Even though the same degree of oxidation exists in the backbone of GO for both cases, the nature of the functionalization is very different.

An important question, which has not been answered in previous studies, is the form in which different functionalizations affect the mechanical behavior of GO. In fact, due to the complicated nanostructure of GO, experimental and theoretical studies to date report conflicting trends in the observed behavior for GO-based systems[9, 11, 81]. For instance, Cao *et al.*[9] reported brittle failure mechanisms observed during membrane deflection experiments with GO flakes exhibiting a 20% degree of oxidation. Conversely, Wei *et al.*[11] reported a ductile failure in GO monolayers with a 70% degree of oxidation. Using density functional-based tight binding (DFTB), these authors identified an irreversible epoxide to ether bond transformation as the source for ductility. In light of these distinct mechanical behaviors, a more comprehensive investigation that considers the effect of composition of functional groups on GO is required to elucidate the mechanisms that govern its mechanical behavior. A detailed correlation between GO's structure and its material properties will have significant implications in the design and selection of GO archetypes that are meaningful towards engineering applications.

Here, we apply atomistic simulations to investigate the interplay between GO chemistry and material deformation. To achieve this, we study extreme cases of GO sheets functionalized purely with epoxide and hydroxyl functional groups, as well as combinations between said functional groups. First, a Monte Carlo-based algorithm[11, 28] is employed to generate physical GO models that are both chemically stable and in agreement with previous literature[11, 28, 61-65]. Then, we apply the DFTB method, employing the analysis techniques described in Chapter 2, to study the mechanical properties of GO as a function of the composition of functional groups. In

particular, the intrinsic atomistic mechanism that governs the material deformation and gives rise to the versatility of GO is revealed through a series of comparative calculations. In this way, we identify a multi-dimensional material design space associated with the chemistry intrinsic to GO during its synthesis, suggesting potential ways to engineer GO with tunable mechanical properties.

Results and Discussion

Chemistry-Driven Failure in GO Monolayers

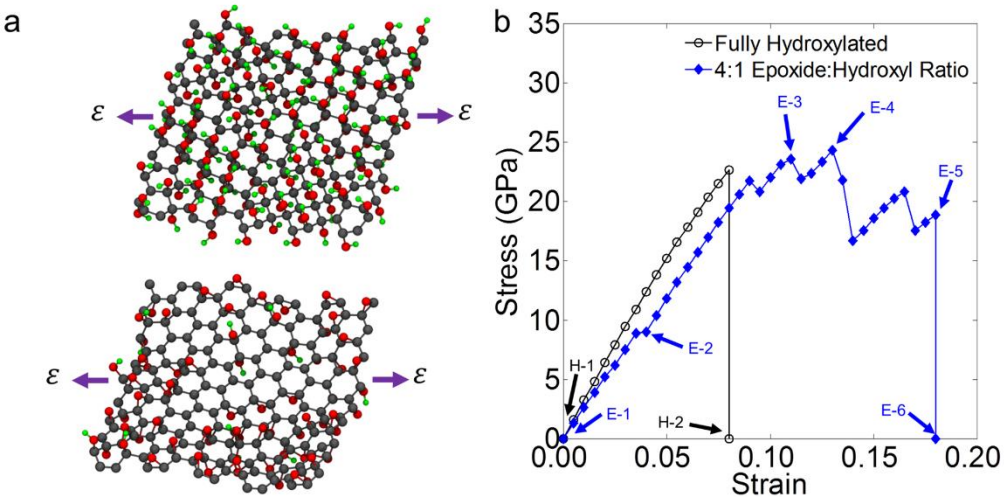

Figure 21. Atomistic configurations and representative stress-strain curves for graphene oxide (GO) monolayers with different chemical composition. a, Atomistic models for hydroxyl-rich (top) and epoxide-rich (bottom) GO configurations. Strain (ε) is applied as indicated in the models. Gray, red and green beads correspond to carbon, oxygen and hydrogen atoms, respectively. **b,** Representative stress-strain curves for hydroxyl- and epoxide-rich GO, tested along the armchair direction. Numbered H and E markers represent atomistic snapshots of interest in Figure 22 and Figure 23, respectively.

Two GO sheets functionalized with representative chemical compositions are considered first (Figure 21a). The first GO sheet has an epoxide-rich composition. According to previous work[11], GO synthesized using a modified Hummers' method can reach a 70% degree of oxidation (defined as the fraction of oxidized carbon atoms), with a 4:1 epoxide-to-hydroxyl functional group ratio. For this structure, a small number of carbonyl, oxetane, and ether groups may also be present, consistent with the electron microscopy reports of Erickson *et al.*[47] The second GO sheet

considered possesses the same degree of oxidation as that reported by Wei *et al.*, but a hydroxyl-rich composition similar to reports by Cao *et al.*, to highlight the difference in deformation mechanisms due to chemical composition[9, 11]. As shown in Figure 21b, we determined the stress-strain (σ-ε) curves for the sheets subjected to uniaxial strain along the armchair direction, preventing contraction along the zigzag direction. From these curves, we obtained the Young's modulus (*i.e.*, the slope of the linear elastic regime), strength (*i.e.*, maximum stress), and toughness (*i.e.*, the area under the stress-strain curve up to failure), as discussed in Chapter 2. The generality of our findings is also further discussed in this Chapter.

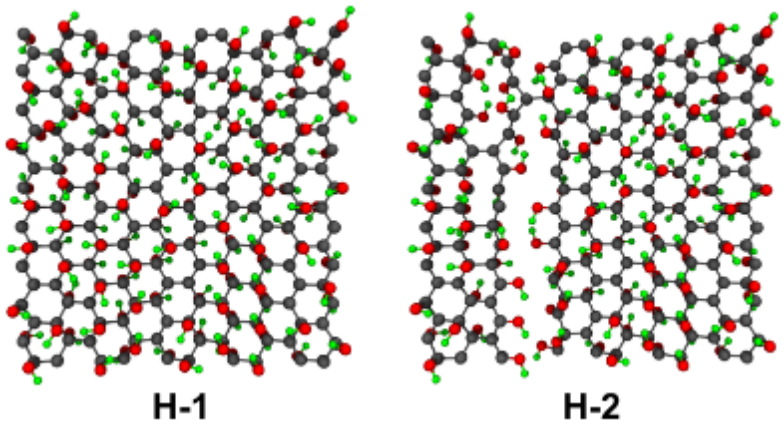

Figure 22. Atomistic configurations of hydroxyl-rich graphene oxide during the deformation process. Numbered H markers represent atomistic snapshots of interest as shown in Figure 21. Gray, red and green beads correspond to carbon, oxygen and hydrogen atoms, respectively.

It is interesting to note that, after applying a small strain (*i.e.*, bottom left of Figure 21b), the stress-strain responses of the two sheets are similar. Deviations from linear elasticity occur for the epoxide-rich GO at approximately 4% strain. Moreover, while the maximum load that the material can bear for both compositions is similar (24.3 GPa for epoxide-rich and 22.7 GPa for hydroxylated), the post-peak stress behavior and failure mechanisms are starkly different. Hydroxyl-rich GO undergoes a sudden, brittle failure near maximum load, while epoxide-rich GO withstands significant additional deformation before its eventual failure. This suggests that

epoxide groups enable a mechanism that enhances material ductility compared to hydroxyl-rich GO. To understand this effect, we investigate atomistic configurations throughout the deformation process. As shown in Figure 22, failure in hydroxyl-rich structures occurs due to the formation of a crack, which propagates abruptly through bonds associated with hydroxyl-functionalized carbon atoms. During failure, hydroxyl groups present along the crack front align with the in-plane direction as captured in snapshot H-2 of Figure 22. During the crack propagation process, as groups present near the crack tip align with the in-plane direction, repulsions from steric effects manifest in the crack tip leading to unstable crack growth. Thus, crack propagation mechanisms present when hydroxyl groups are dominant in GO lead to a brittle and catastrophic failure as observed in experiments reported previously by Cao *et al.*[9]

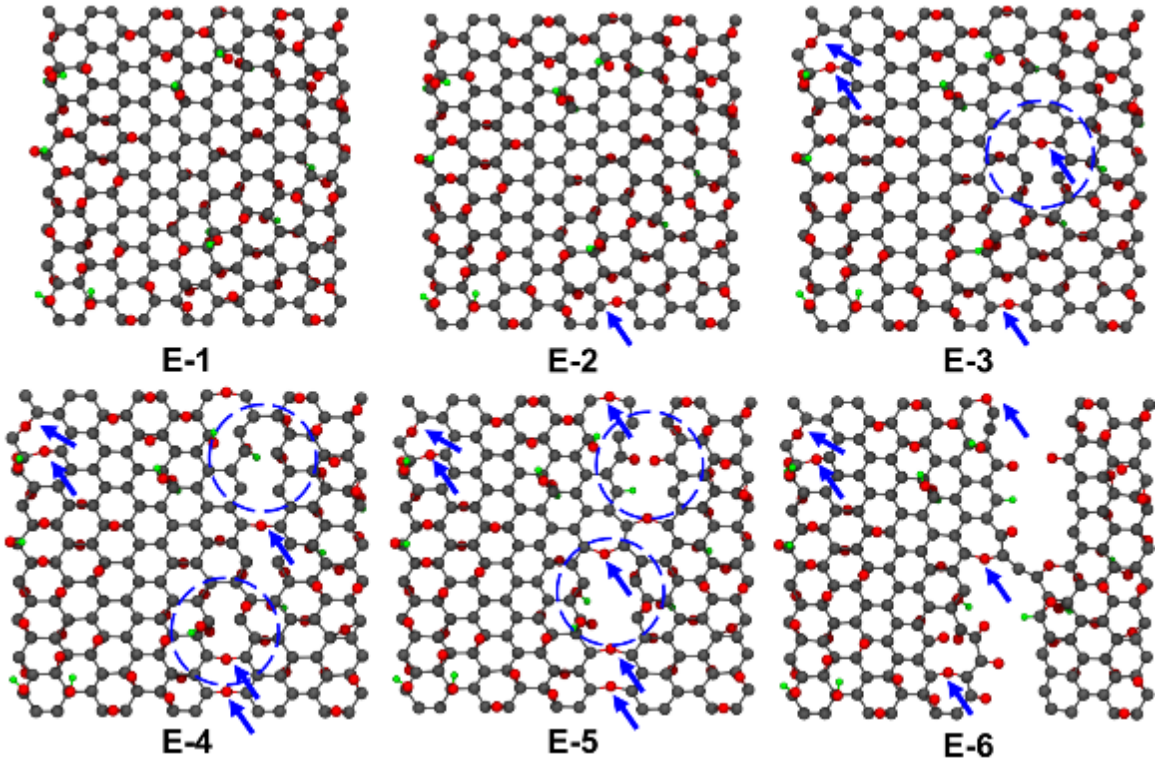

Figure 23. Atomistic configurations of epoxide-rich graphene oxide during the deformation process. Numbered E markers represent atomistic snapshots of interest as shown in Figure 21. Gray, red and green beads correspond to

carbon, oxygen and hydrogen atoms, respectively. In snapshots E-2 to E-6, arrows and dashed circles are used to indicate epoxide-to-ether transformation events and crack nucleation zones, respectively.

In contrast to the brittle failure in hydroxyl-rich GO, epoxide-rich GO exhibits ductile deformation beyond its maximum load. From snapshots E-1 and E-2 on Figure 23, we observe a functional group transformation at 4% strain (marked with a blue arrow), where an epoxide functional group transforms into an ether functional group by cleavage of the C-C bond associated with the epoxide ring, leading to a strain burst shown in Figure 21b. It is important to note that ether groups are covalently bound within the GO sheets, and are more flexible than epoxide rings, allowing GO to bear significantly more deformation than the rest of its graphitic backbone could otherwise achieve. Upon further loading, more epoxide-to-ether transformations take place, as shown in snapshot E-3 of Figure 23. Meanwhile, some sp^3 C-C bonds (not bound within epoxide groups) break in front of the newly-formed ether groups, driving the cleavage of the GO sheet through crack propagation, as highlighted in snapshots E-3, E-4 and E-5 in Figure 23, with dashed blue circles indicating crack nucleation regions. Unlike the case for hydroxyl-rich GO, crack propagation is stabilized due to the energy dissipated through epoxide-to-ether transformations. Moreover, ether groups at the crack tip are highly stretchable due to the flexible C–O–C angles they form, blunting the crack propagation front and enabling the material to withstand significant deformations before final failure (see snapshot E-6 on Figure 23). These observations clearly suggest that epoxide groups enable GO to exhibit and fail in a ductile fashion, consistent with experimental observations from the epoxide-rich GO studied by Wei *et al.*[11]

Influence of Chemical Composition on Mechanical Properties of GO Monolayers

To further elucidate how different compositions of functional groups can affect the mechanical properties of GO, we considered additional configurations that contained a 70% degree

of oxidation but differed in terms of chemical composition. We define the ratio of epoxide and hydroxyl groups as

$$\delta = \frac{N_{epoxides}}{N_{epoxides}+N_{hydroxyls}} \tag{19}$$

where $N_{epoxides}$ and $N_{hydroxyls}$ are the total number of epoxide and hydroxyl groups present in a monolayer. We conducted a series of DFTB calculations on 70% oxidized GO sheets by varying δ from 0 to 1. The stress-strain curves were obtained as before, and representative stress-strain curves are shown in Figure 24a. The stiffness, strength and toughness of the sheets were calculated as a function of δ and are also plotted in Figure 24.

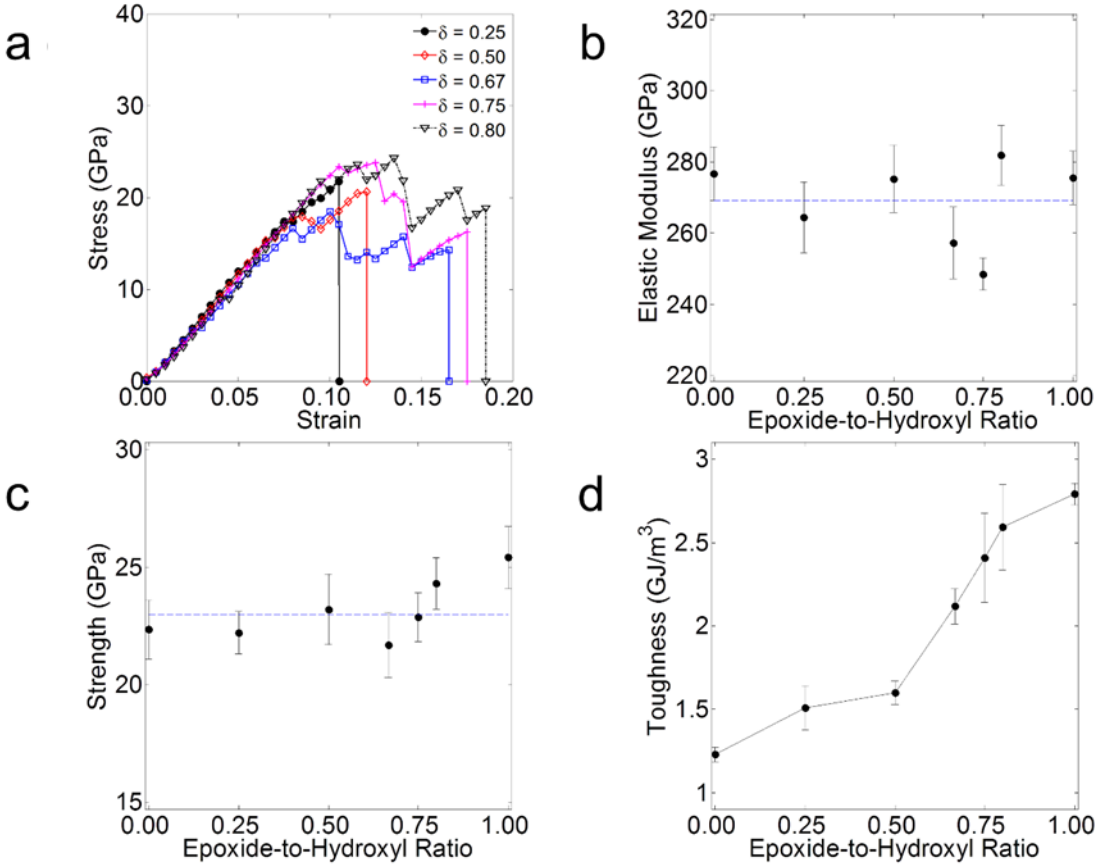

Figure 24. Summary of mechanical properties for 70% oxidized GO monolayers with varying chemical composition a-d, Representative stress-strain curves (**a**) and variation of elastic modulus (**b**), tensile strength (**c**) and

toughness (**d**) with composition. All error bars correspond to $\pm$ 1 standard deviation in material properties obtained from 5 different structures with random spatial distributions of functional groups.

Interestingly, both the stiffness (Figure 24b) and strength (Figure 24c) of the material are almost independent of the composition. At small deformations, the majority of the load on the sheet is carried by the carbon backbone with negligible load-transfer between out-of-plane bonds (*i.e.*, bonds between oxygen and backbone carbon atoms). Although the nature of the functionalization is different in each case, the relative amount of sp^2- vs sp^3-type C-C bonding remains the same when the oxidation density is kept constant. As a result, the stiffness of the sheet should not be affected by the composition, as shown in previous reports[63]. Furthermore, and since all the GO sheets shown in Figure 24b and Figure 24c contain the same degree of oxidation, one should expect the elastic modulus and strength to be approximately constant if *i*) the effect of functional groups in the breakdown of the sp^2 bond network is approximately the same, and *ii*) spatial distribution effects are negligible. Since one can expect functional groups to degrade the electronic network of graphene through similar mechanisms, this serves as potential validation on the second-order nature of the effects of spatial distribution of functional groups.

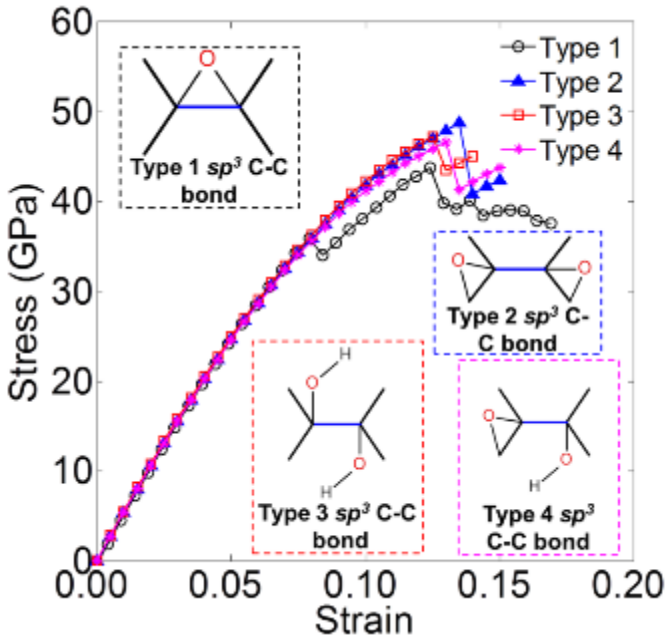

Figure 25. Stress-strain curves for graphene oxide (GO) sheets containing a single sp^3 C-C bond with four different bond types possible in GO.

The strength of GO corresponds to the peak stress on the stress-strain curves. To understand the effect of composition on strength, we analyzed the nanostructures of GO, where four types of sp^3 C-C bond configurations were identified as shown in Figure 25. The majority of sp^3 C-C bonds are type 1 and type 2 in epoxide-rich GO, while type 3 and 4 sp^3 C-C bonds become more dominant as the density of epoxide groups (*i.e.,* δ) decreases. Apparently, these sp^3 C-C bonds are the 'weakest links' in the material from where fracture initiates. The strength of the material is dependent on the maximum loads that these four types of bonds can bear. We built four GO sheets, each one containing only a single sp^3 C-C bond of these four types. The sheets are stretched uniaxially as before, and we record the stress corresponding to the onset of bond breaking of these four types. As shown in Figure 25, types 2, 3, and 4 exhibit similar behavior, as the stress rises to a similar value before a load drop occurs. For each of these bond types, this load drop corresponds to the sp^3 C-C bond breaking followed by unstable crack propagation in the graphitic matrix. By contrast, type 1 sp^3 C-C bonds display two load drops. The first drop corresponds to an epoxide-

to-ether transformation, beyond which the ether functional group withstands additional load up to a second load drop at stress similar to those in types 2, 3, and 4. The second load drop is due to the stress concentration built up in front of the ether group, which in turn drives the crack propagation. Based on the above analysis, the material failure initiated at these four types of sp^3 C-C bonds occurs at the similar stress level. Therefore, the strength of GO does not show notable dependence on the composition of functional groups.

To further quantify the degree of ductility introduced by epoxide-to-ether transformations, we studied the toughness (Γ) of GO, which was computed by integrating the stress-strain curve as described in Chapter 2, using the definition

$$\Gamma = \int_0^{\varepsilon_f} \sigma \, d\varepsilon \tag{20}$$

where ε_f is the ultimate strain upon failure. As shown in Figure 24d, epoxide groups increase the toughness of GO, particularly when δ is above 0.5, allowing the material to absorb energy and deform in a ductile manner before fracturing. The toughening of GO is largely due to the additional material deformation made possible through elastic energy dissipation from epoxide-to-ether transformations and the added flexibility of ether groups. Remarkably, we note that when epoxide content increases, the material becomes more stretchable and ductile without sacrificing its intrinsic strength. This is very interesting since strength and toughness are mutually exclusive for most structural materials[4]. Here, we show the potential for avoiding this tradeoff and enhancing material toughness by engineering the chemical composition of GO.

Table 2. Mechanical properties for GO sheets with a 70% degree of oxidation and a 1:1 epoxide: hydroxyl functional group ratio, with different functional group spatial distributions.

System	Elastic Modulus (GPa)	Strength (GPa)	Toughness (GJ/m^3)
1	253.4	20.7	1.46

2	285.1	26.5	1.60
3	287.3	22.5	1.74
4	264.8	23.2	1.60
5	271.9	24.8	1.58

The spatial distribution of functional groups in GO is largely random due to the stochastic oxidation process, as previously shown by Erickson *et al.*[47] To account for this, five GO structures were generated based on our Monte Carlo algorithm for each oxidation level and composition (*i.e.*, five models with the same degree of oxidation and composition, but different spatial distribution, were subjected to our simulated mechanical experiments). The randomness in the spatial distribution of functional groups introduced scatter in mechanical properties as indicated by the error bars in Figure 24 and as captured in Table 2. However, the general trends in the properties do not change as a result of these deviations. The standard deviation of the measurement, when compared to the magnitude of the properties, clearly highlight the fact that spatial distribution indeed acts as a second-order effect in GO.

As previously alluded to, the material space for monolayer GO is complex due to simultaneous variations in degree of oxidation and chemical composition, which lead to distinct mechanical behavior of various GO archetypes. In this light, and given the large number of systems of interest in this study, simulations that rely on a high level of theory such as DFT would become prohibitively expensive. To circumvent this challenge, we opted to utilize the DFTB approach to quickly and accurately screen the material space accessible to GO (wherein multiple chemical compositions can exist for a given degree of oxidation), and extract material properties of interest. Nevertheless, we validated our results by comparing the in-plane stress-strain behavior of a specific GO sheet with a single epoxide functional group using DFT and DFTB. Our main focus during this exercise was to examine the accuracy of DFTB as compared to DFT in predicting

mechanical properties (*e.g.*, Young's modulus and strength) and deformation mechanisms (*e.g.*, epoxide-to-ether transformations) of the same model system. It is important to note that DFTB has already been previously shown to compare favorably with experiments[2, 4, 9, 10].

As shown in Figure 26, DFT and DFTB are comparable and capture critical deformation mechanisms present in the system. For instance, Figure 26a shows a load drop for both DFT and DFTB, corresponding to an epoxide-to-ether transformation of the functional group in the material, albeit at different stress levels. The strength, failure strain and failure mechanisms along the armchair (Figure 26a) and zigzag (Figure 26b) directions are similar for the case considered. For all the properties of interest in our study (*i.e.*, Young's modulus, strength, toughness), DFTB shows a consistent stiffening of the system when compared to DFT. However, this is not surprising based on previous reports on carbon nanomaterials that rely on DFTB calculations[93] and the fundamental assumptions made to enhance the computational efficiency of the method[70, 94]. Given the reasonable agreement between DFT and DFTB in terms of trends, mechanical properties and deformation mechanisms observed in the material, and the good agreement with experimental findings, we opted to utilize DFTB for our study to benefit from the computational efficiency afforded by the method for the large number of simulations performed in this study.

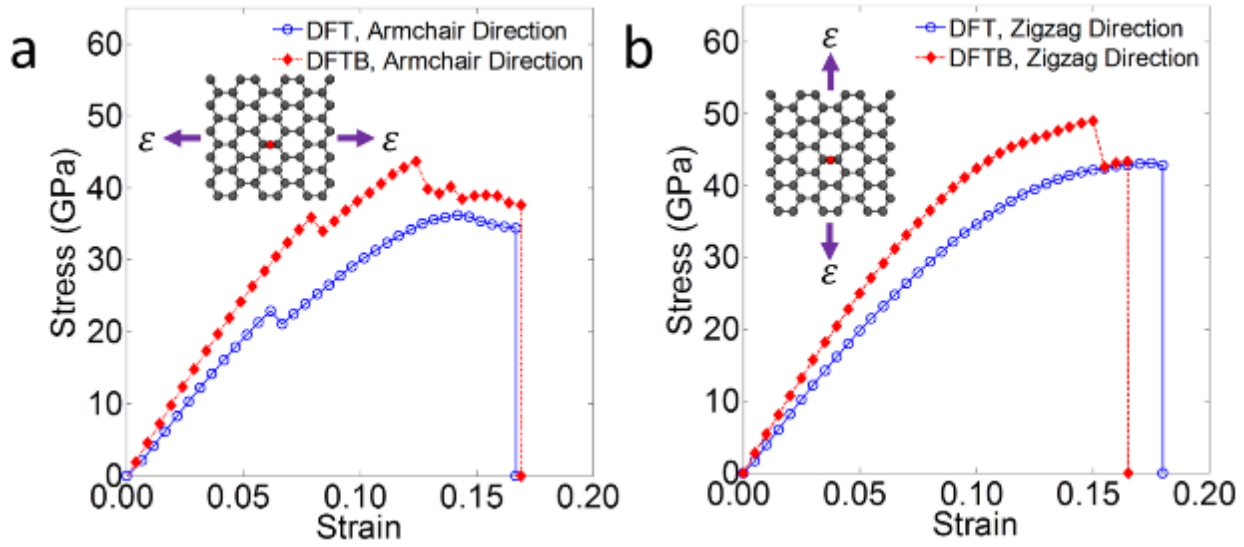

Figure 26. Comparison of stress-strain response for a 1 x 1 nm^2 GO sheet obtained from DFT and DFTB calculations. a, b, Stress-strain curves for applied tension along the armchair (**a**) and zigzag (**b**) direction are shown.

Furthermore, and due to the computational efficiency afforded by DFTB, we also studied the effect of the degree of oxidation on the mechanical properties of GO. Figure 27a and b summarize the elastic properties and strength of systems simulated in this study when subjected to uniaxial tensile strain along the armchair and zigzag directions, respectively. As reported by both theoretical and experimental investigations of unfunctionalized (*i.e.*, carbon nanotubes and graphene) and functionalized (*i.e.*, GO) carbon nanomaterials, the mechanical properties of functionalized carbon nanomaterials degrade as a function of increasing degree of oxidation[9, 11, 15, 63, 81, 92]. Perhaps much more interestingly, from this study it becomes apparent that elasticity and strength at a certain degree of oxidation are seemingly independent of the composition of the system. This is in agreement with our findings on the effects of the epoxide-to-hydroxyl ratio, δ, where we found that average values of elastic modulus and strength, at a given degree of oxidation, can capture such properties for a diverse set of GO archetypes.

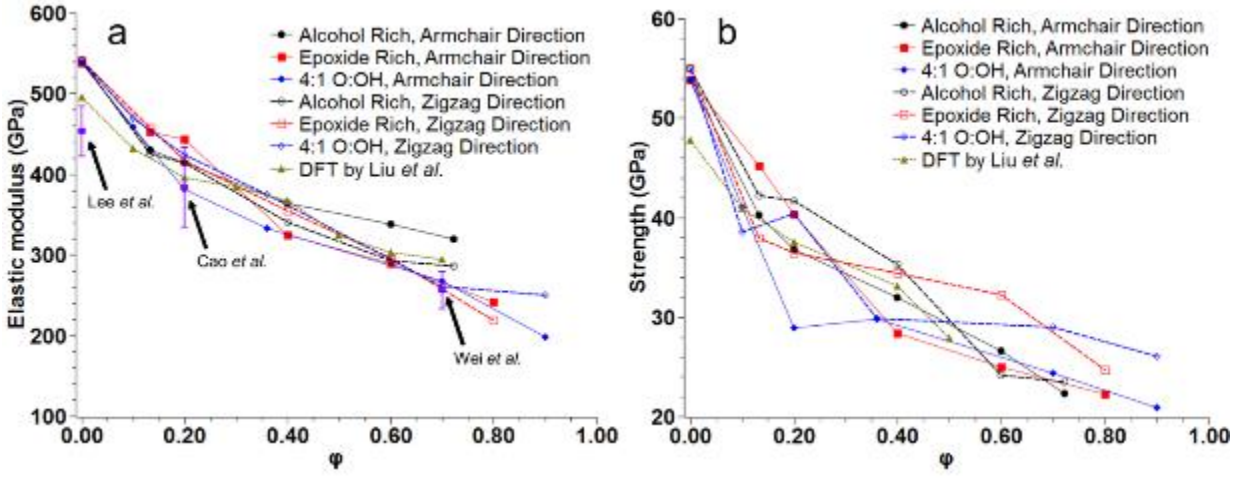

Figure 27. Mechanical properties of GO monolayers with varying chemical composition and degree of oxidation, *φ*. a, b, Summary of the elastic modulus (**a**) and strength (**b**) for GO monolayers with varying composition. DFT curve from Liu *et al.* obtained from [63] for amorphous GO. Error bars correspond to standard deviations from experimental measurements in [9, 11, 15].

The results obtained herein suggest the existence of a large design space in which multiple GO properties vary simultaneously, as a function of the composition of functional groups. It is shown that epoxide-rich GO outperform hydroxyl-rich GO, in terms of in-plane mechanical properties, by virtue of increasing toughness without forfeiting strength and stiffness. However, the selection of an "optimal" archetype may be more complicated when other aspects have to be considered. For example, in GO-based nanocomposite materials, interfacial interactions between stacked sheets are critical to understand composite deformation and failure[12, 26, 29-30, 58, 91, 95]. It is noted that functional groups without terminal hydrogen atoms require the presence of a chemical "mediator" (e.g., water or polymeric materials) to allow for effective hydrogen bonding networks to form in the out-of-plane direction[26, 29]. Furthermore, the chemical reactions that are accessible to epoxide functional groups are quite limited as compared to hydroxyl functional groups. In this light, the presence of hydroxyl groups may add increased reactivity, opening the door for further chemical interactions to occur, and making their utility critical for engineering applications. While beyond the scope of this Chapter, it is important to understand the role of functional groups in GO

interlayer interactions, as well as the interactions between GO and various polymeric materials, which add additional layers of intricacy to the design of the atomistic structure of GO.

Chapter Summary

In summary, the mechanical properties of GO as a function of chemical composition were studied through a large number of atomistic simulations based on DFTB and selectively validated through DFT studies. It was found that the mechanical behavior of GO strongly depends on the ratio between epoxide and hydroxyl functional groups. Brittle fracture was observed in hydroxyl-rich GO, while epoxide-rich GO favors ductile failure due to a mechanically driven epoxide-to-ether group transformation, enabling GO to absorb energy and prevent failure through crack blunting. Moreover, through this effect, GO exhibits significantly enhanced toughness without loss in material strength and stiffness, in contrast to typical engineering materials. The results highlight the potential to utilize GO as a tunable building block in nanocomposites and many other applications by engineering the chemical composition and, in turn, the mechanical properties of GO monolayers.

Chapter 5: Optimizing the Fracture Toughness and Stiffness of Graphene Oxide Monolayers with an Atomically Thin Polymer Layer

Contributions and credit: **Mr. Rafael A. Soler-Crespo** experimentally measured the mechanical properties of PVA-GO-PVA monolayers and bilayers, analyzed all experimental datasets, co-led HRTEM imaging efforts and co-led the theoretical analysis, **Dr. Xiaoding Wei** experimentally measured the mechanical properties of GO-PVA monolayers, **Ms. Lily Mao** synthesized and characterized all materials used, co-led HRTEM imaging efforts and performed imaging analysis, **Dr. Jianguo Wen** and **Dr. Dean Miller** led HRTEM imaging efforts and assisted in imaging analysis, **Mr. Hoang Nguyen** co-led the theoretical analysis, and **Mr. Xu Zhang** assisted in performing molecular dynamics calculations to train the crack bridging model.

Introduction

Engineered composite materials are ubiquitously comprised of interfaces, which ultimately play a critical role in defining their mechanical performance[2]. Given that the behavior of these interfaces largely determines the effective strength of such materials, research avenues that enable mechanical property optimization through interfacial engineering have garnered significant research interest. In principle, such an ideal interface will be reformable by employing interaction mechanisms such as hydrogen bonding, lead to strong cohesion, *i.e.*, strong bonding between dissimilar materials to take advantage of their properties, and significantly enhance toughness[2-3, 29]. This stringent set of requirements on the behavior of the interface similarly leads to constraints on the properties of the bonded materials, in order to fully optimize interfacial interactions and yield ideal performance. In this light, graphene oxide (GO), an atomically thin material comprised of numerous surface functional groups that are capable of extensive interfacial interactions[2, 38],

e.g., hydrogen bonding[26, 38], presents a unique opportunity to tailor and facilitate the engineering of interfaces[2, 10].

The engineering of interfaces is essential since crack propagation through interfaces largely determines the effective performance of materials, and this design process allows significant control over the length scales at which failure-resistance mechanisms, *e.g.*, crack bridging, stopping and blunting, become effective[3]. In this regard, and inspired by a recent discovery regarding nanoscale crack blunting in GO[10-11], we were compelled to examine if macroscopic crack-bridging can be extended to the mesoscale (100 nm to 1 μm) using a nanoconfined polymer interface, given their low dimensionality and weight, to design stiff and tough interfaces which in turn lead to enhanced material performance. Indeed, based on the rule of mixtures and experimental observations, an atomically-thin layer of polymer provides the best opportunity to significantly enhance toughness by providing crack bridging, while optimizing stiffness as the polymer's volume fraction is reduced[1, 3]. To this end, we envisioned utilizing an ultra-thin layer of poly(vinyl alcohol) (PVA), which is capable of strongly interacting with the oxidized domains of GO through hydrogen bonds, to mechanically reinforce a GO nanosheet at the mesoscale through the formation of an extended, nanostructured polymer network that increases the fracture toughness of GO nanosheets while maximizing stiffness.

Herein, we engineer GO-PVA interfaces inspired by chemical and mechanistic principles and find that the addition of an ultra-thin PVA layer significantly enhances the fracture toughness of GO nanosheets, through a mesoscale polymer chain crack-bridging mechanism, granting control over the length scale at which GO failure resistance manifests. Nanoscale characterization reveals the presence of an extended, nanostructured hydrogen-bonding network on the surface of GO,

which is the origin of a three-fold increase in the load-bearing capacity of GO nanosheets, as found through nanomechanical membrane deflection experiments. The crucial role of reformable hydrogen bonds between GO and PVA in enhancing fracture toughness and failure resistance of GO is revealed by a detailed fracture mechanics model, guided by atomistic molecular dynamics (MD) calculations. Through this approach, we identify for the first time the "mesoscale" version of a typically macroscopic mechanism[3] in which nanoconfined polymers delay load localization and fracture[96-100], illustrating how GO-polymer nanolaminates can serve as effective constituents in GO-based composite materials and revealing how interfacial engineering can be further exploited to tailor and optimize the behavior of engineered materials.

Results and Discussion

Due to the thickness (< 2 nm) of the PVA layer, and the length scale (100 nm to 1 μm) at which crack-bridging was expected to occur, the mechanical properties of suspended GO-PVA nanolaminates were interrogated via atomic force microscopy (AFM) membrane deflection experiments. GO nanosheets modified with a ~1.5-nm thick layer of PVA (total thickness of 2.5 nm) were fabricated by sequential Langmuir-Blodgett (LB) deposition of GO[36] and PVA onto a patterned Si substrate (see Figure 28a and Chapter 2). Prior to nanomechanical testing, the formation of a nanostructured PVA network on GO was confirmed through high-resolution transmission electron microscopy (HRTEM) techniques (Figure 29), and the polymer microstructure was studied via AFM characterization (Figure 28b). Notably, the load-deflection behavior of GO-PVA nanolaminates revealed a three-fold increase in load bearing capacity, as compared to single GO nanosheets, accompanied by permanent deformation and bulging of polymer near regions where the membranes were loaded (Figure 30 and Figure 31), suggesting the

existence of a toughening mechanism later identified as crack bridging (schematized in Figure 28c). The atomistic basis of this crack-bridging mechanism in GO-PVA was validated through molecular and continuum modeling techniques (Figure 32), revealing that reformable hydrogen-bonding interactions between GO and PVA chains lead to effective interfacial load transfer, resulting in a significant increase of GO's load bearing capacity.

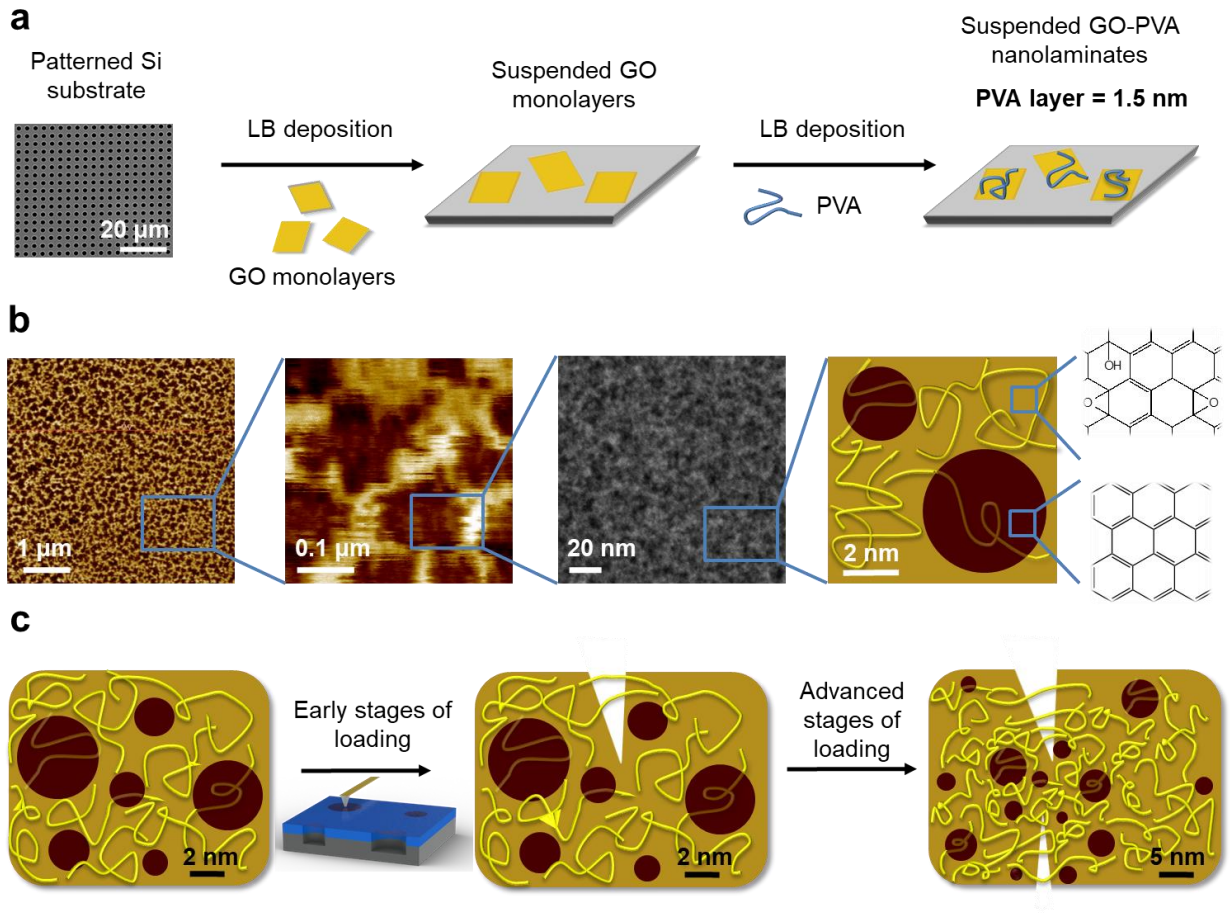

Figure 28. Fabrication, structure, and crack-bridging mechanism of GO-PVA nanolaminates. a, Langmuir-Blodgett (LB) fabrication of suspended GO-PVA nanolaminates. **b,** Hierarchical structure of GO-PVA nanolaminates. The AFM images in the first two panels show the microscale structure, and the STEM image in the third panel shows the nanoscale structure. The proposed molecular structure based on HRTEM and EELS characterization is shown in the schematic of the fourth panel. **c,** Schematic of mesoscale crack-bridging in GO-PVA nanolaminates during AFM membrane deflection experiments. In (**b**) and (**c**), brown and gold represent graphitic and oxidized domains, respectively, while yellow denotes PVA chains.

HRTEM and STEM Characterization of GO-PVA Nanolaminates

We assumed that PVA chains of ~130 repeat units (~34 nm extended chain length) can suitably interact with and bridge across multiple GO oxidized domains (separated by graphitic domains of ~3-6- nm^2 in size, as reported by Erickson *et al.*[47]). The acquired AFM images confirmed that this is indeed the case, as the use of longer PVA chains results in lowered coverage of PVA on the GO surface (see Appendix D); and as revealed by HRTEM and electron energy-loss spectroscopy (EELS) characterization (see discussion below). Based on HRTEM images, the nanoscale structure of the investigated GO-PVA nanolaminate is not readily distinguishable from that of GO in both this work and previous literature[47], since both PVA and the oxidized GO domains are amorphous (Figure 29a and b). To overcome this limitation, we employed a spectroscopic technique that is sensitive to differences in local chemical composition, together with microscopy imaging studies, to elucidate the structure of GO-PVA nanolaminates, as discussed in Chapter 2.

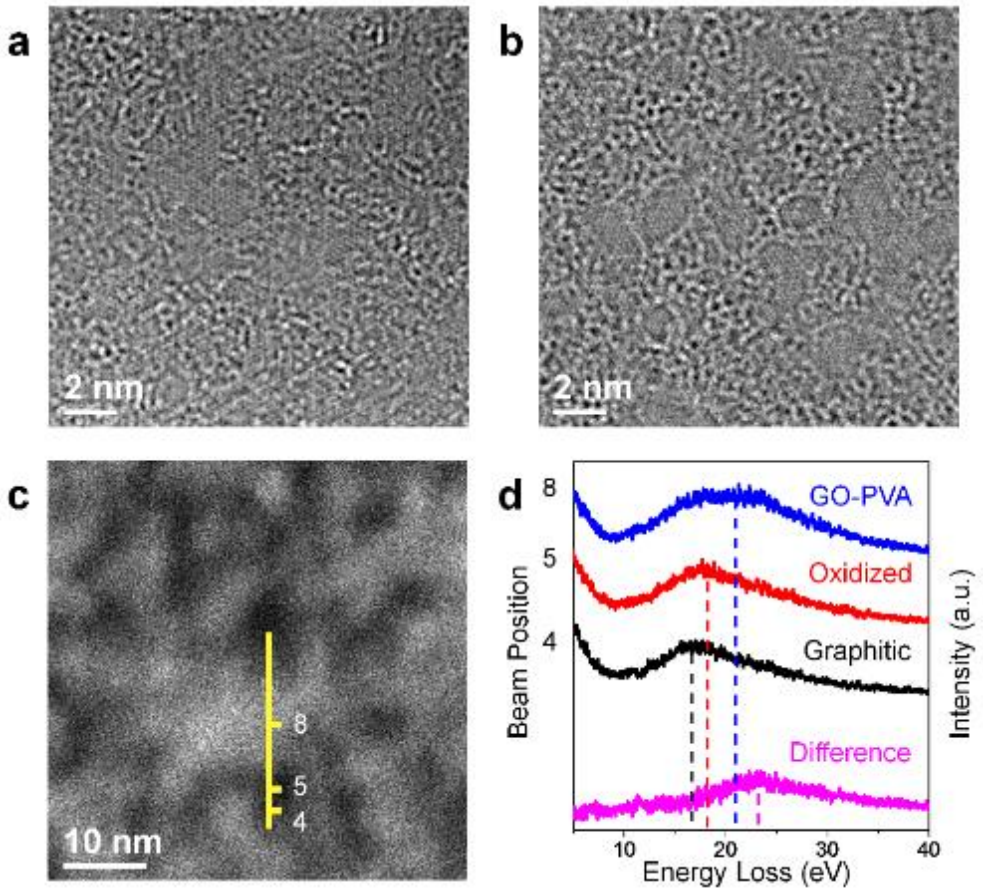

Figure 29. HRTEM and EELS characterization of GO-PVA nanolaminates. a, HRTEM image of GO. **b,** HRTEM image of GO-PVA nanolaminate. **c,** EELS line scan across HAADF-STEM image of GO-PVA nanolaminate. The yellow line represents the line scan pathway, with the numbers corresponding to the beam position at individual points along the line scan. **d,** EELS spectra corresponding to the line scan in (**c**).

The close association of PVA chains with the oxidized domains of GO was verified by analyzing the plasmon peak position in the low loss region of EELS spectra. We utilized EELS in TEM mode to characterize a series of reference samples to establish peak positions for the graphitic, oxidized, and PVA-covered regions present in GO-PVA nanolaminates (see Chapter 2). The locations of PVA adsorption with respect to the oxidized and graphitic domains of GO were then determined through an EELS line scan in scanning transmission electron microscopy (STEM) mode, given the finer lateral resolution of STEM (in our experiments, ~0.25 nm spot size, compared to a 500 nm region in TEM). In the high-angle annular dark-field (HAADF) image of

the GO-PVA nanolaminate (Figure 29c), an EELS line scan across regions of varying z-contrast revealed changes in chemical composition. As the line scan moves from the low-z-contrast region to the high-z-contrast region, across a distance of 10 nm, the π + σ plasmon peak in the corresponding EELS low-loss spectra shifts from 15 (low-z-contrast) to 17 eV (moderate-z-contrast), and then to 21 eV (high-z-contrast), as shown in Figure 29d. These values correspond to the π + σ peak positions for graphitic, oxidized, and GO-PVA domains, respectively. In addition, subtracting the EELS low-loss spectrum corresponding to the oxidized domain of GO, from the spectrum of GO-PVA, provides the spectral contribution from pure PVA, a peak at 23 eV (Figure 29d). These data suggest that PVA is mostly present on the oxidized domains of the GO sheet (*i.e.*, the high-z-contrast areas) and confirms the hypothesis that hydrogen-bonding interactions lead to the formation of a nanostructured PVA network on the oxidized domains, which extends over the entire surface of GO.

Interestingly, atomic force microscopy (AFM) imaging of the GO-PVA nanolaminates reveals a much larger microscale pattern of interconnected PVA-dense regions (~20-150 nm in size), consistent with features that arise from polymer dewetting (Figure 28b)[101]. Similar to nanoscale dewetting of liquid films on substrates with micron-scale chemical heterogeneities[101], the heterogeneity of the GO-PVA surface (*i.e.,* graphitic and PVA-covered regions as described above), can support differential growth of PVA. Such growth presumably leads to visible PVA dewetting on the microscale as observed by AFM (Figure 28a and b, and Appendix D), and a 1-2 order of magnitude difference between the length scale of the chemical heterogeneity and that of the dewetting pattern, comparable to previous literature[102]. In contrast, when PVA is deposited on a predominantly graphitic surface, a dewetting pattern at the micron scale is not observed by AFM imaging (see Appendix D).

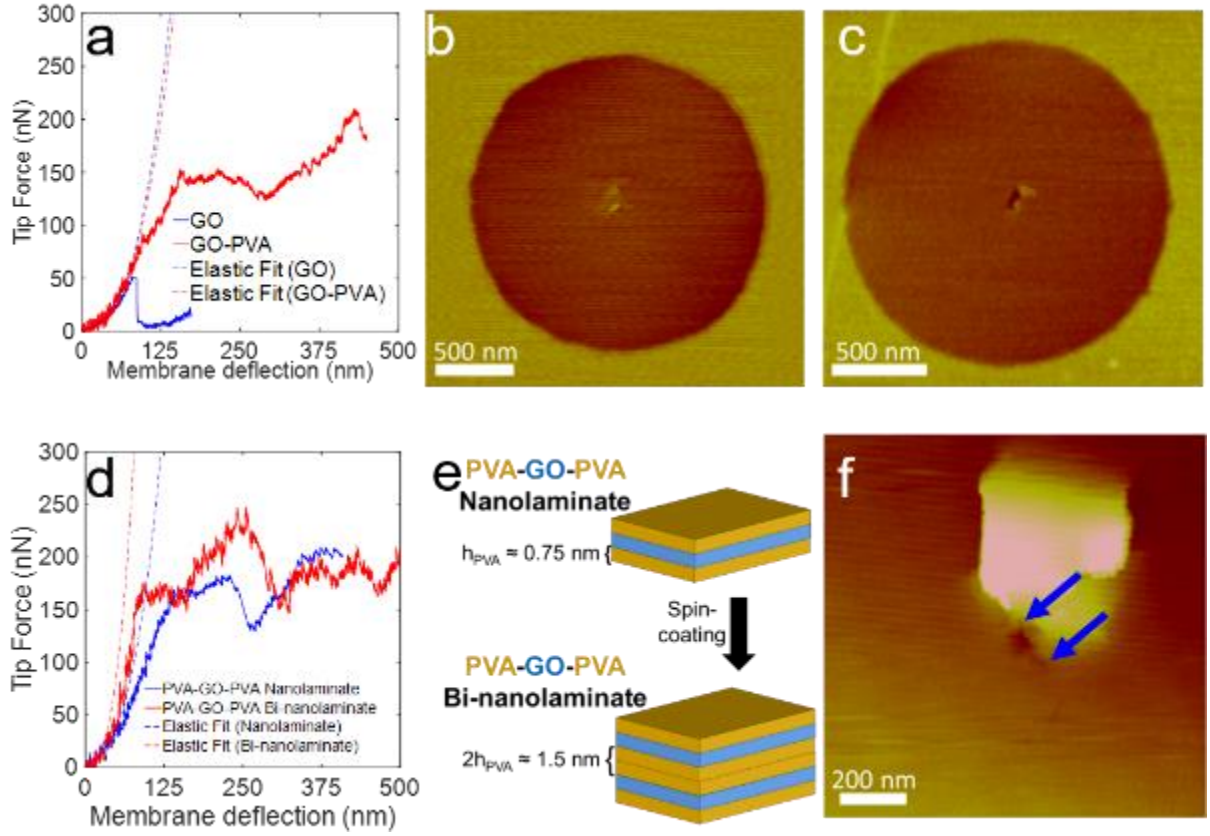

Figure 30. Mechanical characterization of GO-PVA nanolaminate systems. a, Force-deflection curve for GO and GO-PVA. **b, c,** Rupture surface for GO-PVA (**b**) and GO (**c**). **d,** Force-deflection curve for PVA-GO-PVA nano- and bi-nanolaminates. **e,** Schematic depicting PVA-GO-PVA nanolaminates, obtained by premixing GO and PVA in solution, with PVA thickness *h*. The thickness of the resulting interface in PVA-GO-PVA nano- and bi-nanolaminates is shown in brackets as a multiple of the thickness of the constituent nanolaminate. **f,** Rupture surface for PVA-GO-PVA bi-nanolaminates. Nanocracks are highlighted by blue arrows. Regions with brighter color represent larger features in the topology, attributable to bulging of PVA chains near the indented region due to plastic deformations in PVA.

Together, the AFM, HRTEM, and EELS data obtained in this study confirm the presence of a hierarchical PVA network structure comprised of nanoscale and microscale features, which is expected to lead to differences in mechanical behavior. The ultra-thin, nanostructured PVA network observed here through HRTEM characterization is evidence of strong interactions between GO and PVA, which can lead to crack bridging at the GO-PVA interface. Beyond an ultra-thin layer that arises as a combination of polymer deposition and compression during membrane deflection experiments, PVA that does not directly interact with the GO surface is not

expected to contribute significantly to crack-bridging, unless readily spread due to the pressure exerted by the indenter surface. In this sense, the thick, microscale PVA pattern found in AFM images is not directly responsible for the mesoscale crack-bridging that we report herein. As described in the next section, where we perform nanomechanics experiments to interrogate this behavior, we show that the toughening observed in GO nanosheets can only arise if nanoconfined PVA chains extend across graphitic domains to connect oxidized domains and enable crack-bridging.

Mechanical Characterization of GO-PVA Nanolaminates

The polymer nanostructure of GO-PVA nanolaminates, punctuated by a hydrogen bond network, suggests that mechanical reinforcement will lead to a synergistic redistribution of nanomechanical loads as PVA chains bear forces, reducing the effective stress in GO, and delaying the initiation of cracks. As flaws nucleate in the relatively weaker, oxidized domains of GO, PVA chains will bridge these domains (discussed below), enable mesoscale reinforcement mechanisms, and increase the toughness of GO (*i.e.*, load-bearing capacity). Indeed, the force-deflection profile for a suspended GO-PVA nanolaminate (Figure 30a) exhibits an impressive rupture force of 155 $\pm$ 31 nN, a large three-fold increase in the maximum load that it can bear before rupture, in comparison to unmodified GO (47 $\pm$ 12 nN)[11]. In contrast to a rule of mixtures (ROM) prediction, these results clearly demonstrate that the adsorption of relatively weaker PVA chains (strength of 40-140 MPa for bulk PVA[56-59] versus 25 GPa for GO[9-11]) to the relatively stronger oxidized domains of GO significantly increases toughness.

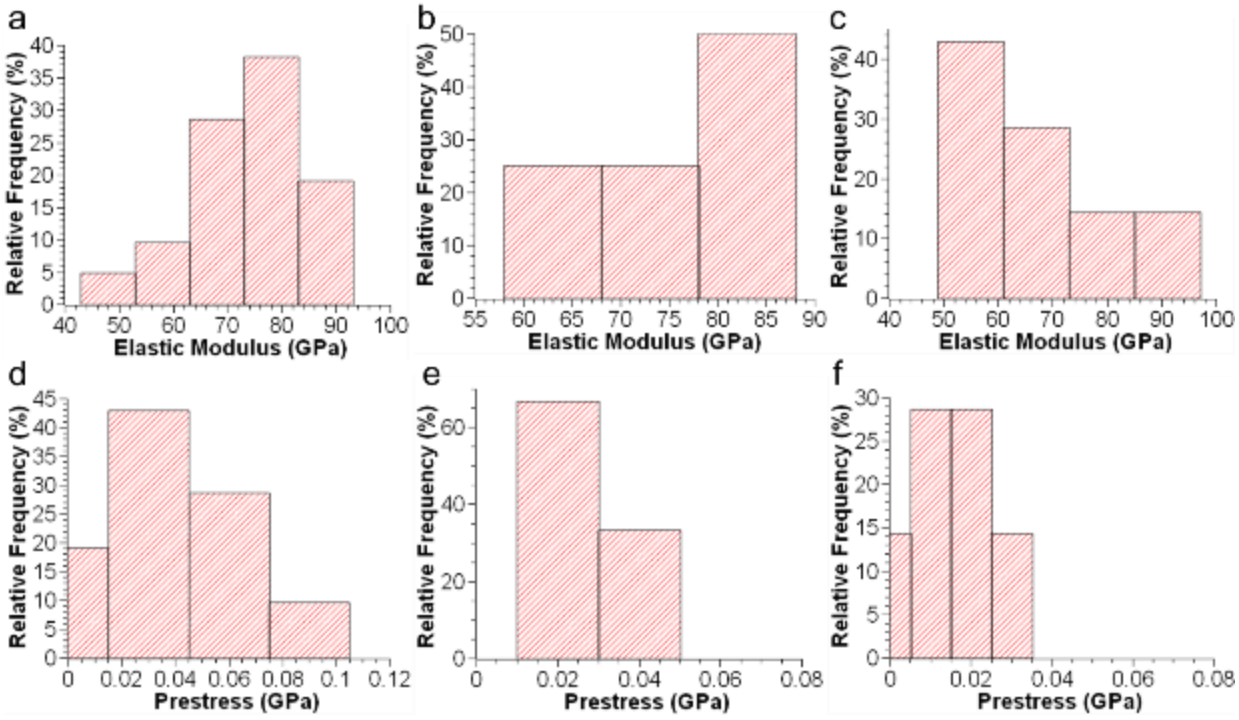

Figure 31. Elastic modulus and pre-stress values obtained from membrane deflection experiments. a-c, Elastic modulus as obtained from linear elastic fit for GO-PVA nanolaminate (**a**), PVA-GO-PVA nanolaminate (**b**) and PVA-GO-PVA bi-nanolaminate (**c**) samples. **d-f,** Prestress as obtained from linear elastic fit for GO-PVA nanolaminate (**d**), PVA-GO-PVA nanolaminate (**e**) and PVA-GO-PVA bi-nanolaminate (**f**) samples.

Ideally, GO-PVA nanolaminates will be tough and stiff, and thus achieve an ideal combination of mechanical properties. When the force-deflection profile for GO-PVA nanolaminates (Figure 30a) is fit to a linear elastic membrane solution over the early stages of deformation (deflection of 25-50 nm), an elastic modulus $E = 78 \pm 11$ GPa is obtained (see Table 3 and Figure 31). This is in good agreement with ROM predictions, and rapidly approaches the theoretical maximum for GO-PVA nanolaminates as PVA becomes atomically thin. Together with the increase in rupture force described above, this reasserts that the nanostructured polymer network provides excellent load transfer and increases toughness while achieving high stiffness. Importantly, the stiffness of the GO-PVA nanolaminate in this work is 2-10 times higher than that of GO-polymer nanocomposites reported in the literature[2, 26, 30, 58, 103], which highlights the benefit

of utilizing ultra-thin polymer layers that approach atomic thickness to optimize toughness (via crack-bridging) and stiffness.

Table 3. Elastic modulus and prestress obtained in GO-PVA and PVA-GO-PVA experiments based on linear elastic analysis from force-deflection curves.

System	2D elastic modulus (N/m)	Modulus (GPa)	Prestress (GPa)
GO[11]	192 ± 21	256 ± 28	0.7 ± 0.3
GO-PVA	196 ± 28	78 ± 11	0.06 ± 0.03
PVA-GO-PVA Nanolaminate	196 ± 26	78 ± 10	0.03 ± 0.01
PVA-GO-PVA Bi-nanolaminate	365 ± 72	72 ± 14	0.02 ± 0.01

Crack-bridging in GO-PVA nanolaminates further manifests through their highly inelastic behavior after rupture, as they continue to bear significant load for an additional 350 nm of deflection, unlike GO (Figure 30a). As shown in Figure 32 and discuss below, in the discussion of the atomistic modeling of the fracture process, such behavior is only possible if the reinforcing, nanostructured PVA network limits crack growth during the loading process (Figure 28c). If the crack length is comparable to the bridging zone length (on the order of the extended length of an adsorbed PVA chain), it is possible to stabilize the developing flaw and limit its growth[3]; specifically, when PVA chain and crack length are comparable, the hydrogen bond network formed between PVA chains and GO is able to transfer load and lead to further crack-bridging at the mesoscale. Indeed, the rupture of the indented GO-PVA nanolaminates (Figure 30b), is confined to the area in direct contact with the AFM tip (< 25 nm radius), in stark contrast to the more prominent rupture typically observed for a single GO nanosheet (Figure 30c), suggesting that mechanical energy is dissipated during crack growth. Such a phenomenon can be considered the "mesoscale" version of crack-bridging mechanisms shown for fiber-reinforced ceramics and

concretes[3, 98, 104-105], and provides a practical mechanism to greatly increase the toughness of GO-based materials.

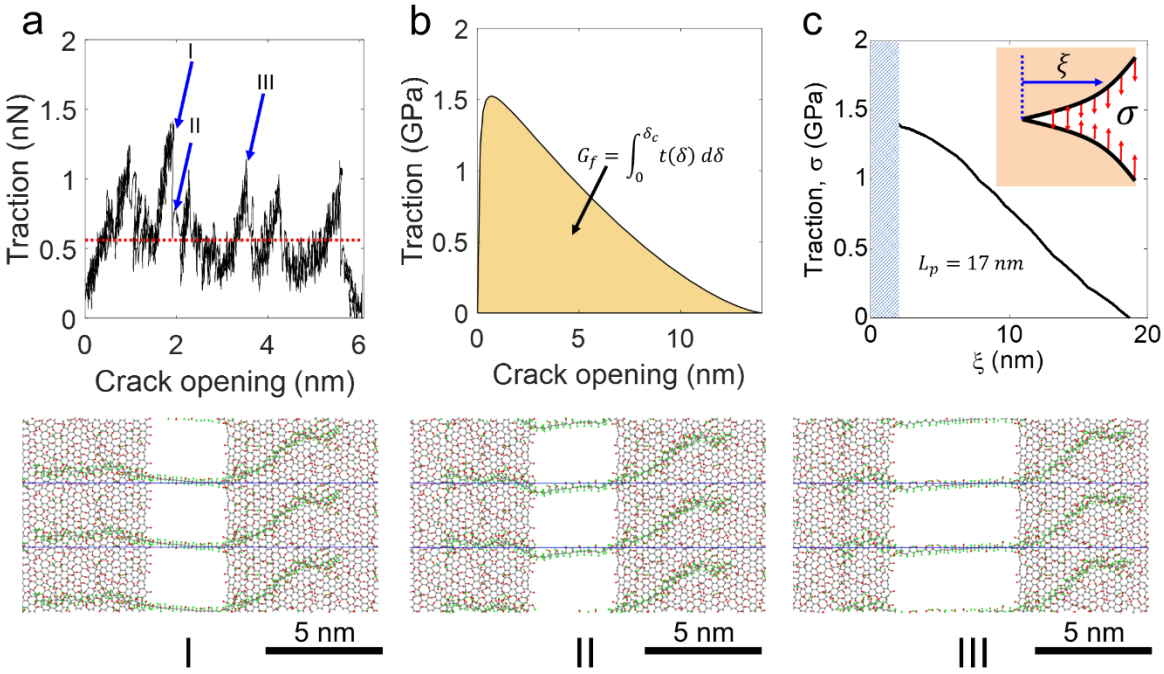

Figure 32. Atomistic and fracture mechanics analysis of GO-PVA nanolaminates. **a,** Tangential traction-crack opening (Mode II) behavior of a single PVA chain suspended over two GO sheets. Labels denote deformation in the atomistic model, as shown in bottom row of Figure 32. Gray, red and green beads represent carbon, oxygen and hydrogen atoms, respectively. The simulation domain, bound by solid blue lines, and two periodic images are shown for clarity. **b,** Average stress-crack opening behavior of PVA chains suspended over GO sheets as obtained from fracture mechanics model. The integration of this curve reveals the energy release rate contribution from PVA chains. **c,** Calculation of process zone length, L_p, from notch test by employing the extended finite element methodology. Inset shows traction-separation contributions, represented by red arrows, accounted for in the solid by explicitly modeling GO normal stress-crack opening (Mode I), and including PVA tangential stress-crack opening contributions after cracks nucleate in GO as smeared Mode I contributions. The shaded region from $\xi = 0$ nm to $\xi = 0.5$ nm corresponds to the region where traction contributions are transferred from GO to the PVA chain.

Importantly, the mesoscale crack-bridging mechanism observed in GO-PVA nanolaminates implies that a small amount of PVA is needed to toughen GO. The nanoscale indentation experiments reported here were carried out on a GO nanosheet coated with an ultra-thin (1.5 nm, see Chapter 2) PVA layer, in contrast to previous studies where thicker polymer layers (> 10 nm) were utilized[26, 103], resulting in diminished mechanical properties due to the high volume fraction occupied by the polymer. Furthermore, as computations reveal (see discussion

below), the effectiveness of mesoscale crack-bridging mechanisms is readily dependent on the interface formed between GO and the crack-bridging PVA chains. Taken together, the current results and previous literature suggest the GO-PVA nanolaminate in this work is a synergistic configuration of the building blocks. Indeed, as the thickness of PVA in GO-PVA nanolaminates approaches atomic thickness, PVA chains enable significant toughness enhancement mechanisms and limit the negative effects of increasing polymer volume fraction on stiffness.

Atomistic Basis of Crack-Bridging and Quantification of Energy Release Rate

To further elucidate the synergistic relationship between nanoconfined PVA and GO nanosheets, it becomes crucial to probe interfacial load transfer mechanisms between GO and PVA by quantifying the evolution of tangential traction, *i.e.,* load on a PVA chain when subjected to displacements parallel with GO surfaces, as a function of crack opening, *i.e.,* the distance between the two surfaces that form a crack. To achieve this, we conducted all-atom MD simulations (see Chapter 2) implementing the ReaxFF force field[16], which has been parametrized[76] for predictions with hydrocarbons and graphene oxide-based systems. Briefly, a single PVA chain (45 monomers, 13 nm contour length) was suspended over two GO sheets, with an initial crack opening of 1 nm, and the sheets were pulled apart to increase crack opening while measuring the tangential traction-crack opening response of PVA. Theoretically, PVA chains should display a significantly strong tangential traction-crack opening response, punctuated by stick-slip tangential traction signatures, due to the reformable nature of interfacial hydrogen bonds between GO and the backbone of the PVA chain. In agreement with this hypothesis, PVA shows significant tangential traction when suspended over GO (Figure 32a). An average tangential traction of 0.6 nN was measured for GO-PVA due mainly to the presence of functional groups capable of forming hydrogen bonds.

Interestingly, PVA chains load to a peak tangential traction when suspended over GO (~1 nN, see Figure 32a) and slip, unloading tangential traction in the chain and forming new hydrogen bonds at the GO-PVA interface (see Figure 32). Then, the PVA chain is able to bear further load before hydrogen bonds break once more and subsequent slippage occurs (Figure 32a). In stark contrast, such strong tangential traction effects cannot presumably be observed for graphene-PVA as van der Waals interaction dominate in this system, and hydrogen bonds cannot be formed due to the lack of oxygen-containing surface functional groups. This last point motivates results shown in Chapter 6.

This hydrogen-bonding, tangential stick-slip mechanism, made possible by the strong interactions between GO and PVA, suggests the atomic basis of the crack-bridging phenomena observed in membrane deflection experiments. To confirm this hypothesis, the tangential traction-crack opening behavior captured for PVA suspended over GO sheets is introduced in a fracture mechanics framework[3], successfully shown to predict the traction-crack opening response and the energy release rate involved during crack-bridging (see Chapter 2). Indeed, our analysis reveals that the energy release rate G of GO-PVA-which arises as a sum of the energy release rates of GO and PVA chains, G_0 and G_f, respectively-is G = 13.97 nN/nm, in contrast to that of single GO nanosheets[19] (G_0 = 4.54-6.11 nN/nm, see Figure 32b). The employed model reveals that the average stress-crack opening response of PVA suspended over GO crack edges, as a consequence of reformable stick-slip hydrogen-bonding, is responsible for increasing the energy release rate of GO-PVA nanolaminates. Indeed, this average stress-crack opening response (Figure 32b) develops with small crack openings and is accompanied by a gradual release of stress, stabilizing energy release during crack growth. Notably, the process zone for GO-PVA, *i.e.*, region around the GO crack tip with significant PVA traction that impedes crack opening, measured employing finite

element analysis (see Chapter 2 for details) is ~17 nm and in stark contrast to that of quasi-brittle GO (~0.5 nm, see Figure 32c). In this light, our observations reveal the importance of interfacial load transfer near the crack tip, provided by PVA chains near the GO surface capable of forming strong, reformable hydrogen bonds, and show our system to be analogous to ceramics where strong tangential tractions from fibers are critical to promote crack bridging[3].

Mechanical Characterization of PVA-GO-PVA Nano- and Bi-Nanolaminates

The crack-bridging mechanism observed for the GO-PVA nanolaminate investigated here suggests that depositing PVA on both faces of the GO nanosheet should lead to further improvements in strength, without affecting stiffness, if polymer volume fraction is kept constant. Such PVA-GO-PVA nanolaminates can be prepared by spin coating a pre-mixed GO-PVA solution[106] on a patterned substrate (as discussed in Chapter 2). Remarkably, this method allows us to reduce the thickness of the polymer layer beyond 1 nm, as AFM imaging suggests both sides of the GO nanosheet are covered by a PVA monolayer with thickness of only ~0.75 nm (total sample thickness = 2.5 nm; see Chapter 2 for thickness characterization). Notably, the force-deflection profile of the PVA-GO-PVA nanolaminate (Figure 30d) shows a rupture force of 176 $\pm$ 24 nN, a 15% increase with respect to that of GO-PVA nanolaminates (155 $\pm$ 31 nN). As anticipated, and since the volume fraction of PVA in the system remains constant, the elastic modulus (E = 78 $\pm$ 10 GPa) of PVA-GO-PVA nanolaminates remains unchanged from that of GO-PVA (E = 78 $\pm$ 11 GPa, see Figure 31 for comparison of fitted properties for experiments).

The success in extending the crack-bridging mechanism to PVA-GO-PVA nanolaminates prompted us to explore whether nanoconfined polymer reinforcement still applies to a thicker system, such as PVA-GO-PVA bi-nanolaminates. Through spincoating, we can obtain a mix of

nanolaminates and bi-nanolaminates on patterned Si substrates. The 5-nm-thickness of the latter is consistent with the stacking of two PVA-GO-PVA nanolaminates of 2.5 nm thickness (see Figure 30e and Chapter 2). To ensure the validity of the experimental results analysis we have compared membrane deflection behavior, applicable to PVA-GO-PVA bi-nanolaminates, to bending in thicker plates (see Chapter 2 for discussion on validity of membrane deflection model for nanolaminates). The 2D elastic modulus of bi-nanolaminate PVA-GO-PVA (E_{2D} = 365 $\pm$ 72 N/m) scales with the number of PVA-GO-PVA nanolaminates (E_{2D} = 196 $\pm$ 26 N/m) (see Table 3, and Chapter 2 for discussion on 2D elastic modulus scaling behavior), suggesting there is excellent load transfer between PVA-GO-PVA nanolaminates. This strongly implies that GO-based nanocomposite materials with excellent mechanical properties may be obtained by stacking PVA-GO-PVA nanolaminates, as the mechanical properties of individual PVA-GO-PVA nanolaminates are maintained.

Consistent with inter-laminate load transfer, a "rupture force" of 201 $\pm$ 53 nN was measured for PVA-GO-PVA bi-nanolaminates. While this 15% increase in rupture force over PVA-GO-PVA nanolaminates (176 $\pm$ 24 nN) is beneficial, force-deflection curves and AFM surface analysis suggest that it does not reflect the true load-bearing capacity of the system. The post-test surface of PVA-GO-PVA bi-nanolaminates distinctly contains a heightened feature, presumably an accumulation of plastically deformed PVA chains (*e.g.*, bulging of the loaded polymer region), in the center of the membrane after significant loading. Closer inspection of this feature (Figure 30f) reveals the presence of surrounding nano-cracks (~75-100 nm) which presumably do not penetrate through the thickness of the bi-nanolaminate assembly. Based on these observations, we attribute this "rupture force" to the puncture of the top PVA-GO-PVA nanolaminate, which explains why no force scaling is observed. Presumably, a visible fissure is

not observed because the bottom PVA-GO-PVA nanolaminate behaves as a “reinforcing net” in the indentation experiments, which have a limitation in producing larger membrane deflections for bi-nanolaminates. Ideally, if the bi-nanolaminate could be further deflected, a progressive failure of the layers should occur in the assembly, thereby suggesting the presence of a crack arrest mechanism – a highly desirable feature in the design of nanocomposites.

Chapter Summary

In summary, this study probed the structure-property relationships present in GO-PVA nanolaminates, and revealed interfacial engineering pathways by which GO’s toughness was significantly enhanced. The materials characterization, mechanical experiments, and computational studies conducted herein confirmed that the presence of a layer of PVA, which approached atomic thickness (~0.75 nm thick), deposited over GO leads to tremendous toughening due to mesoscale crack-bridging, attributable to hydrogen bond-mediated stick-slip behavior during crack growth. Importantly, the mechanism shown here resembles macroscopic crack-bridging observed in ceramic, fiber-reinforced composites and uncovered strong interfacial synergies between atomically thin polymers and 2D materials that can be exploited in future interfacial designs. Based on our findings, we are confident that interfacial engineering will be leveraged to enhance the mechanical performance of a variety of 2D materials towards controlling failure and, in turn, stimulating the design of the next-generation of materials and advanced composite systems.

Chapter 6: Concluding Remarks and Outlook

The work presented herein initially set out to validate molecular modeling as a powerful toolbox that could realize the principles set forth by the Materials Genome Initiative, and lead to a revolution in the approach by which fundamental knowledge is discovered and materials are designed. In this light, a combination of experimental tools were used to validate the molecular modeling predictions in this thesis, which confirmed the powerful capabilities and unparalleled degree of tailoring that GO presents as a material. Clearly the results shown here, complemented by the critical work of other researchers in the field, underpins the upcoming importance of GO as a critical constituent block in engineered materials.

Initially, the discovery of mechanochemical transformations in GO showcased it as a critical test bed for studying the interplay between chemistry and mechanics, and revealed the possibility of engineering its in-plane mechanical properties. Particularly, preliminary observations made by studying the mechanical properties of monolayer GO, experimentally and computationally, elucidated the conditions and chemical behavior of epoxide-to-ether functional group transformations, which endow certain GO archetypes with inelastic and ductile constitutive behavior. The computational observations were fully validated by designing focused experiments, which considered the chemistry of the material and took advantage of established knowledge regarding its chemical reactivity – just as anticipated by the Materials Genome Initiative.

The aforementioned observations, coupled with existing reports at the time[9], motivated a careful investigation of the complex structure-property space on which GO can be tailored. In particular, due to its complex microstructure, the chemistry (*i.e.*, ratio of functional groups) and degree of functionalization (*i.e.*, oxidation level) often can be manipulated independently and,

based on literature, lead to distinct mechanical behavior[9-11]. A study of the effect of these factors, which was found to be feasible *in silico* and is contained within this thesis, revealed the critical interplay between fracture pathways and mechanical properties of GO, and its chemistry. DFTB calculations performed in this thesis revealed how hydroxyl functional groups in GO lead to brittle failure, while epoxide functional groups lead to ductile failure and significantly increase toughness in the material. Thereby, using computational methodologies, the materials envelope of GO was characterized, and idealized GO archetypes to optimize in-plane mechanical performance were uncovered.

The previously referenced studies revealed intrinsic toughening mechanisms which GO can leverage, due to its complex chemistry, to increase its resilience and prevent catastrophic failure. Inspired by these atomic-level intrinsic toughening mechanisms, we then investigated how such toughening mechanisms can be extended to a combination of a GO monolayer with an atomically thin PVA sheet, which resulted in an extrinsic crack bridging mechanism which increased the energy release rate of the material three-fold. A developed fracture mechanics continuum theory, complemented by atomistic molecular simulations, demonstrated how the stick-slip behavior of hydrogen bonds across the GO-PVA interface facilitates extensive load transfer and mechanical bridging. Furthermore, by achieving the deposition of such an atomically thin PVA layer, we demonstrated how this GO-PVA nanosheet optimizes toughness and stiffness, and can be considered as an outstanding candidate constituent material towards the design of future engineered devices and structural materials.

The findings contained herein reveal fascinating interplays in the mechanical and interfacial behavior of GO and GO-based systems, and reveal the power of computational tools in

predicting their performance. However, the work in this thesis does not directly address how the developed tools can be employed to push forward the tenets of the Materials Genome Initiative and aid in the design of the next generation of deployed, engineered materials. To demonstrate the power of the developed tools, and to start addressing this question with an outlook to the future, we briefly turn to exploring how different substrate-polymer systems can take advantage of the crack bridging behavior revealed herein.

Insight into the Design of Crack Bridging Substrate-Polymer Systems

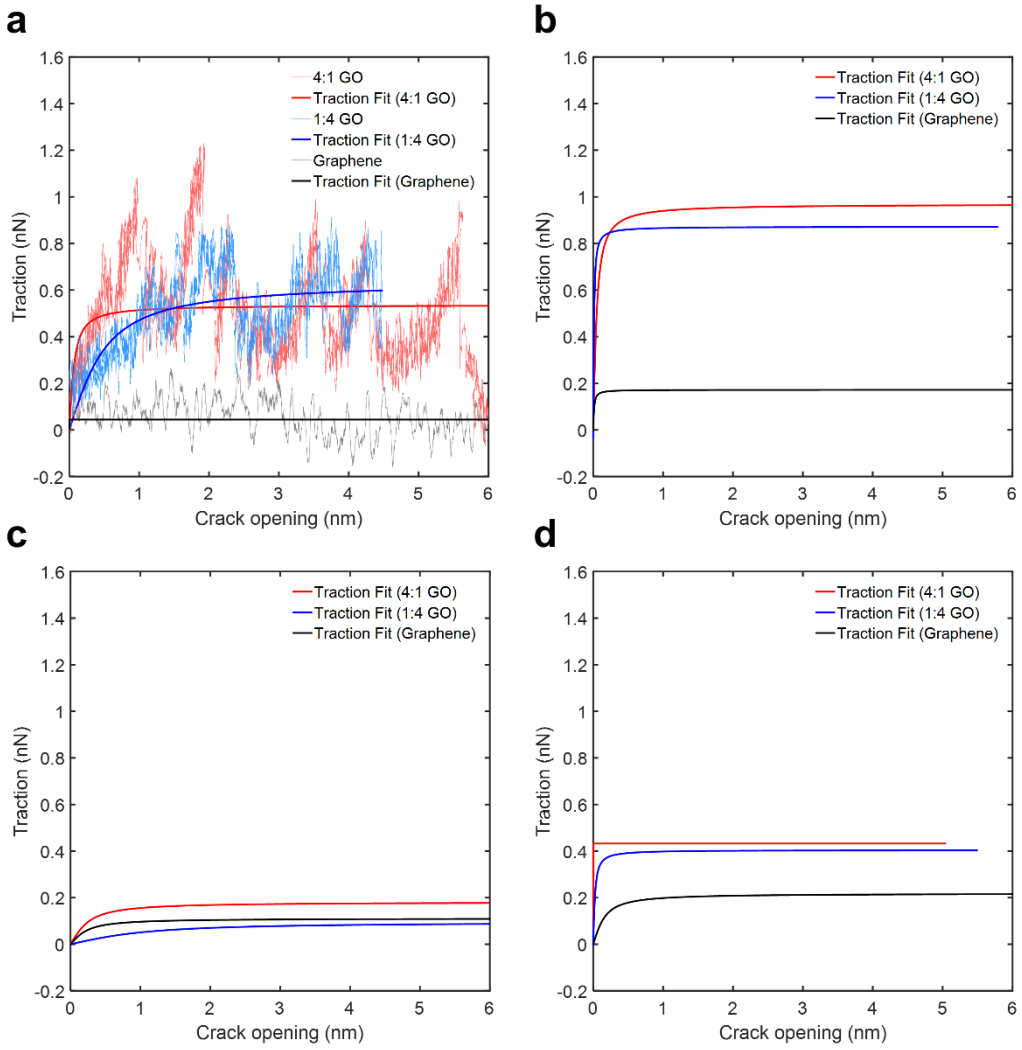

Figure 33. Traction-separation behavior for combinations of GO archetypes and polymers. a-d, Traction-separation response for 70% oxidized 4:1 epoxide:hydroxyl GO, 70% oxidized 1:4 epoxide:hydroxyl GO and graphene when interacting with PVA (**a**), cellulose (**b**), poly(ethylene) (**c**) and poly(styrene) (**d**). Raw traction-separation and fitting behavior is shown only for GO-PVA, with the other polymer types showing only fitted response.

The knowledge disseminated herein sets an important foundation towards the discovery of design rules and guiding principles that can inform nanocomposite fabrication trends. In particular, two key aspects arise from the work performed herein: i) the composition and arrangement of functional groups in GO has a powerful impact on the mechanical and chemical behavior of the material (as shown in Chapter 4), and ii) the interfaces which the material can form can lead to tremendous toughening characteristics, at the expense of a modest reduction in the overall mechanical properties of the assembled structure, if designed appropriately (as shown in Chapter 5). Instinctively, one may question if the GO-PVA combination maximizes performance given the immense library of GO archetypes and polymers. This question is intrinsically linked to the core of this thesis, given it is in line with the tenets set forth by the Materials Genome Initiative, and can be preliminarily answered by extending the frameworks and knowledge developed herein.

Part of our current efforts are centered on answering this question by extending the crack bridging model, developed as part of Chapter 5, to consider the multiple GO and polymer archetypes that can occur. In particular, one may broadly divide GO archetypes as hydroxyl-rich, epoxide-rich and graphitic (*e.g.,* 70% oxidized 1:4 hydroxyl-epoxide GO, 70% oxidized 4:1 hydroxyl:epoxide GO and graphene, respectively) while polymer archetypes can be broadly subdivided as hydrogen bonded, van der Waals dominated and pi-stacking/conjugation capable (*e.g.,* poly(vinyl alcohol) and cellulose, poly(ethylene) and poly(styrene), respectively). In particular, to determine the crack bridging and cohesive behavior of different GO-polymer systems, we performed molecular dynamics simulations with combinations of the aforementioned systems to obtain their tangential traction-crack opening behavior, and calculated their respective

G_f and G values. We hypothesized that, across a broad range of GO archetypes, polymers capable of extensive intermolecular hydrogen bonding would achievethe strongest interactions with GO in a dry environment. By confirming this observation, and based on the observations in such a study, simple design rules that correlate the structure of GO to polymer classes can be extracted and utilized towards the design of nanocomposite systems.

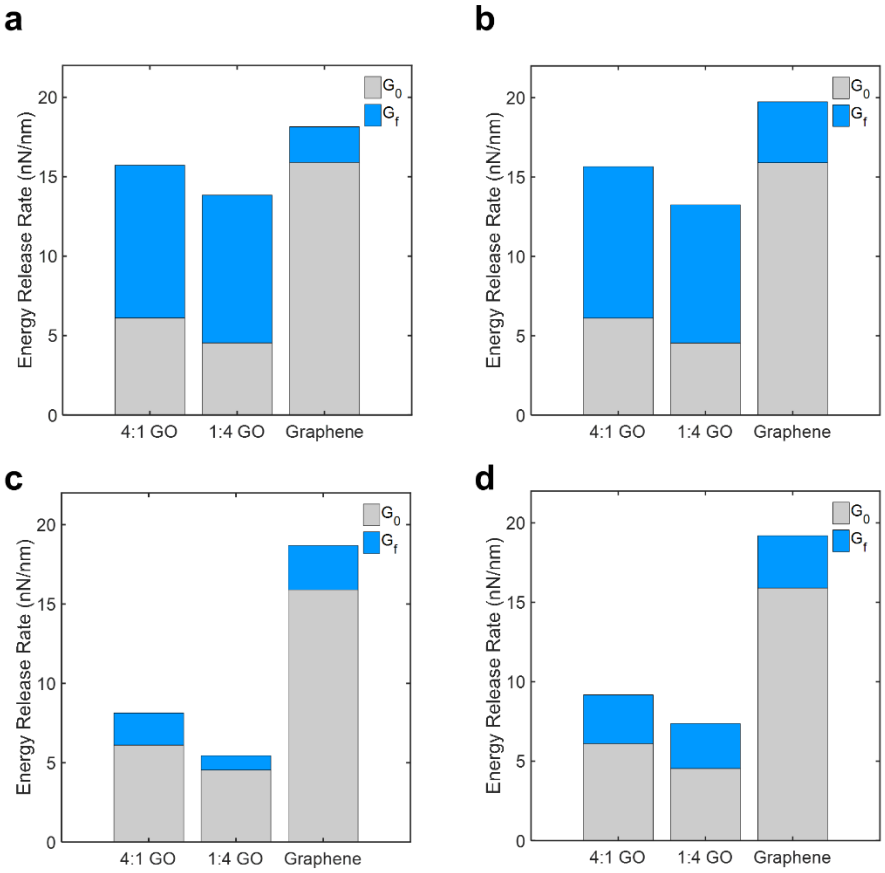

Figure 34. Contributions from fiber and substrate to effective composite energy release rate, *G*. a-d, Energy release rate contributions from the substrate (G_0) and the fiber (G_f) into the effective energy release rate are shown for all considered substrates combinations when PVA (**a**), cellulose (**b**), poly(ethylene) (**c**) and poly(styrene) (**d**) are suspended over an initial crack and pulled.

The fitted traction-separation behavior of various polymer types with different substrate materials is shown in Figure 33. As expected, and due to the relatively strong behavior of hydrogen bonds as compared to van der Waals interactions, it is unsurprising that materials with a high

hydrogen bond density (*i.e.*, GO's that interact with PVA and cellulose) show a significantly stronger traction-separation response due to the cohesion formed at the interface. Indeed, the overall traction for PVA (Figure 33a) is lower than that of cellulose (Figure 33b), given that the monomer for cellulose contains a significantly higher fraction of species capable of hydrogen bonding. In this light, it appears initially advantageous to favor polymers with high hydrogen bonding densities to take advantage of crack bridging mechanisms in GO-polymer systems. Notably, the obtained traction-separation laws can be utilized to numerically obtain an estimate of the energy release rate contribution from the fiber, G_f, as discussed in Chapter 2.

To obtain this estimate of G_f, however, it is important to recall the definition of the effective area of GO covered by the polymer of interest, *i.e.*, A_{GO}. While molecular dynamics simulations can yield an estimate of this value, we desire to consider an upper bound on G_f. To achieve this, we consider a situation of maximum packing whereby the end-to-end cross-sectional length of a polymer is utilized to estimate an effective packing diameter (Table 4), which is used in the calculation for A_{GO}. Notably, this assumes all polymer will interact favorably with the substrate. In this light, it is important to note the key juxtaposition of a variety of chemical effects in the substrate-polymer response. For instance, while cellulose shows significantly higher traction for each individual chain, its considerably larger volume leads to substantially lower density of functional groups capable of hydrogen bonding (*e.g.*, PVA has ~10 groups/nm^2 vs ~8.5 groups/nm^2 for cellulose) which makes other polymer systems with higher hydrogen bond density, like PVA, much more attractive and mechanistically favorable. This last point can be verified by comparing the G_f contributions, after accounting for A_{GO}, for different material systems.

Table 4. Effective packing radius for considered polymers system.

Polymer	Packing Diameter (nm)

PVA	0.40
Cellulose	0.69
Poly(ethylene)	0.31
Poly(styrene)	1.10

Estimates for G and G_f for the various probed combinations, as well as the values for G_0, are shown in Figure 34. It is important to note that the estimated G for different GO archetypes that interact with PVA or cellulose is indistinguishable. This is due to a competition of mechanisms, as previously discussed: while PVA is more compact and can pack a higher number of polymer chains per unit volume, each chain can bear a lower traction and this effect balances the contribution to G. Furthermore, for all hydrogen bonding capable polymers studied, *i.e.,* PVA and cellulose, it is clear that 4:1 and 1:4 GO archetypes are functionally indistinguishable. This is due to the fact that, as long as a hydrogen bond donor/acceptor species is present near the GO substrate, the material interacts with a high hydrogen bond density, which balance the differences in interfacial behavior from the functional groups. It is also noteworthy that no polymer provides graphene with a significant increase in G due to the weak, van der Waals interactions that occur for each system. Indeed, polymers that are more compact and thus able to interact with the surface more strongly (*i.e.*, poly(ethylene) in our case) increase the amount of interfacial interactions per unit volume with graphene, thereby increasing the overall value of G, much more significantly than any hydrophobic polymer-GO combination achieves. However, from an applications perspective, the limited chemistry and interaction capability of graphene does not make it attractive as a potential building block in engineered materials, as its poor interfacial interactions, evidenced by the poor traction responses observed in Figure 33, limits its viability.

Clearly, the approaches developed throughout this work contribute and validate the observations reported herein. Importantly, the validation of molecular simulations as tools that can

provide significant insight into the deformation and failure processes in the material have allowed the development of design rules and guiding principles which enable meaningful materials discovery and manufacturing. In this perspective, there is still much to be gained from the tenets of the Materials Genome Initiative and the application of theoretical tools in materials design. Aiming towards the future and as experimental techniques and molecular simulations become more powerful, the ideology behind the Materials Genome Initiative will be accessible to scientists who seek to employ computational tools as a predictive toolbox leading to a revolution in how materials are discovered, designed and manufactured.

Outlook into the Future

The findings in these studies, and our preliminary analyses on the behavior of substrate-polymer systems, revealed promising pathways for enhancing the behavior of GO-based devices by employing chemical, physical and computational principles. In particular, the work conducted herein reveals how GO, as a building block capable of being significantly tailored, can be designed to take advantage of a rich library of materials that can strongly interact through its functional groups. Based on computational exercises, and inspired by the chemistry of GO and certain polymer types, we quickly arrived at basic design rules and principles that can initially contextualize the search for pathways to modify GO in search of novel materials. However, there are two key points worth mentioning which affect this last point: first, many of the principles discovered in this work are widely applicable to GO due to its rich chemistry, which is not the case for a wide variety of 2D materials. Additionally, it is worthwhile to note that the intuition to select specific theoretical studies arose after a significant number of experiments and simulations were performed, where the fundamental behavior of materials was probed and the characterization

facilitated by these methods provided a new understanding on mechanisms which occurred in GO. In this light, it is critical to understand that the tenets proposed by the Materials Genome Initiative truly only become meaningful once a sufficient amount of fundamental information of the proposed constituents is understood, which then enables the selection of focused experiments and calculations that consider the behavior of the envisioned building blocks and can yield interesting insight.

In terms of techniques, the tools developed here and computational methods in general open the doors to further materials discovery, but it is essential to keep in mind that their promise is often impeded by extraordinarily high computational costs and limitations in the empirical force fields used to describe the molecular systems of interest. For instance, the ReaxFF force field, as applied to GO-based systems[76], is a significant step forward in the development of molecular dynamics tools that can enable the exploration of complex deformations and physics. Our studies revealed that the ReaxFF description of highly oxidized GO archetypes significantly deviates from the microstructure predicted by DFT and DFTB calculations, but the interfacial description of the system was qualitatively reasonable. In this light, the use of these molecular tools as a black box – with improper validation and accuracy verification – can lead to the establishment of principles which may not represent the reality that experiments can probe. Thus, it is critical for researchers to carefully study, and be acutely aware of, the advantages and disadvantages of the computational methods that are applied in research. This will increasingly become a point of major scrutiny as theoretical methods become the foundation of materials research, and the Materials Genome Initiative becomes critical to the mission and vision of materials design and discovery in research communities.

In terms of materials development, it is also important to contextualize that nanomechanical properties are a subset of the features which must be studied and optimized to conceptualize and manufacture the next generation of structural materials, a key focus of the work presented herein. For instance, a significant portion of the work in this thesis revolves around discovering and exposing the key mechanisms that lead to specific in-plane mechanical responses for GO and GO-based systems. However, as these systems are scaled to the structural level, the presence of interfaces, the necessity for hierarchical structures and the critical role of porosity and defects, amongst others, will strongly influence the mechanical response of engineered materials; this will require separate investigations that develop meaningful tools, which elucidate the role of aforementioned factors in mechanical performance. For instance, it has been previously shown that the structure and interfaces of biological materials critically contribute to their superior mechanical behavior[4]. Similarly, 2D materials-based structural systems must be carefully considered from a multiscale perspective given the issues they face in transferring loads across interfaces and assembling hierarchical structures, in contrast to natural materials.

Finally, to validate the empirical tools utilized to achieve the previously described investigations, it is critical to consider the accuracy and power of experimental tools. While the last decade has provided significant advancements in indirect characterization of nanomaterials, a significant amount of headway remains to develop tools that can bridge temporal (*i.e.*, high strain rate testing) and length scales (*i.e.*, monolayer tensioning) differences between experimental and computational studies. Only by directly contrasting experiments and theory will the time spent to develop, characterize and validate simulation tools become drastically reduced, and lead to the advent of the Materials Genome Initiative in materials design.

References

1. Daniel, I. M.; Ishai, O., *Engineering Mechanics of Composite Materials*. 2nd ed.; Oxford University Press: New York, NY, 2005.

2. Gong, S.; Ni, H.; Jiang, L.; Cheng, Q., Learning from nature: constructing high performance graphene-based nanocomposites. *Mater. Today* **2016**, In Press.

3. Bao, G.; Suo, Z., Remarks on crack-bridging concepts. *Appl. Mech. Rev.* **1992,** *45* (8), 355-366.

4. Wegst, U. G. K.; Bai, H.; Saiz, E.; Tomsia, A. P.; Ritchie, R. O., Bioinspired structural materials. *Nat. Mater.* **2015,** *14* (1), 23-36.

5. Akinwande, D.; Brennan, C. J.; Bunch, J. S.; Egberts, P.; Felts, J. R.; Gao, H.; Huang, R.; Kim, J.-S.; Li, T.; Li, Y., A review on mechanics and mechanical properties of 2D materials—Graphene and beyond. *Extreme Mech. Lett.* **2017**.

6. Xia, F.; Farmer, D. B.; Lin, Y.-m.; Avouris, P., Graphene field-effect transistors with high on/off current ratio and large transport band gap at room temperature. *Nano Lett.* **2010,** *10* (2), 715-718.

7. Novoselov, K. S.; Geim, A. K.; Morozov, S. V.; Jiang, D.; Zhang, Y.; Dubonos, S. V.; Grigorieva, I. V.; Firsov, A. A., Electric field effect in atomically thin carbon films. *Science* **2004,** *306* (5696), 666-669.

8. Radisavljevic, B.; Radenovic, A.; Brivio, J.; Giacometti, i. V.; Kis, A., Single-layer MoS_2 transistors. *Nat. Nanotechnol.* **2011,** *6* (3), 147-150.

9. Cao, C.; Daly, M.; Singh, C. V.; Sun, Y.; Filleter, T., High strength measurement of monolayer graphene oxide. *Carbon* **2015,** *81*, 497-504.

10. Soler-Crespo, R. A.; Gao, W.; Xiao, P.; Wei, X.; Paci, J. T.; Henkelman, G.; Espinosa, H. D., Engineering the mechanical properties of monolayer graphene oxide at the atomic level. *J. Phys. Chem. Lett.* **2016,** *7* (14), 2702-2707.

11. Wei, X.; Mao, L.; Soler-Crespo, R. A.; Paci, J. T.; Huang, J.; Nguyen, S. T.; Espinosa, H. D., Plasticity and ductility in graphene oxide through a mechanochemically induced damage tolerance mechanism. *Nat. Commun.* **2015,** *6*.

12. Dikin, D. A.; Stankovich, S.; Zimney, E. J.; Piner, R. D.; Dommett, G. H.; Evmenenko, G.; Nguyen, S. T.; Ruoff, R. S., Preparation and characterization of graphene oxide paper. *Nature* **2007,** *448* (7152), 457-460.

13. Gao, Y.; Liu, L.-Q.; Zu, S.-Z.; Peng, K.; Zhou, D.; Han, B.-H.; Zhang, Z., The effect of interlayer adhesion on the mechanical behaviors of macroscopic graphene oxide papers. *ACS Nano* **2011,** *5* (3), 2134-2141.

14. Ward, C. In *Materials Genome Initiative for Global Competitiveness*, 23rd Advanced Aerospace Materials and Processes (AeroMat) Conference and Exposition, ASM: 2012.

15. Lee, C.; Wei, X.; Kysar, J. W.; Hone, J., Measurement of the elastic properties and intrinsic strength of monolayer graphene. *Science* **2008,** *321* (5887), 385-388.

16. Van Duin, A. C.; Dasgupta, S.; Lorant, F.; Goddard, W. A., ReaxFF: a reactive force field for hydrocarbons. *J. Phys. Chem. A* **2001,** *105* (41), 9396-9409.

17. Wei, X.; Fragneaud, B.; Marianetti, C. A.; Kysar, J. W., Nonlinear elastic behavior of graphene: Ab initio calculations to continuum description. *Phys. Rev. B* **2009,** *80* (20), 205407.

18. Bagri, A.; Mattevi, C.; Acik, M.; Chabal, Y. J.; Chhowalla, M.; Shenoy, V. B., Structural evolution during the reduction of chemically derived graphene oxide. *Nat. Chem.* **2010,** *2* (7), 581-587.

19. Meng, Z.; Soler-Crespo, R. A.; Xia, W.; Gao, W.; Ruiz, L.; Espinosa, H. D.; Keten, S., A coarse-grained model for the mechanical behavior of graphene oxide. *Carbon* **2017,** *117*, 476–487.

20. Ruiz, L.; Xia, W.; Meng, Z.; Keten, S., A coarse-grained model for the mechanical behavior of multi-layer graphene. *Carbon* **2015,** *82*, 103-115.

21. Leach, A. R., *Molecular Modelling - Principles and Applications*. 2 ed.; Pearson - Prentice Hall: Dorchester, 2001.

22. Kurzak, J.; Buttari, A.; Luszczek, P.; Dongarra, J., The playstation 3 for high-performance scientific computing. *Comput. Sci. Eng.* **2008,** *10* (3), 84-87.

23. Nickolls, J.; Dally, W. J., The GPU computing era. *IEEE Micro* **2010,** *30* (2), 56-69.

24. Hu, K.; Gupta, M. K.; Kulkarni, D. D.; Tsukruk, V. V., Ultra-Robust Graphene Oxide-Silk Fibroin Nanocomposite Membranes. *Adv. Mater.* **2013,** *25* (16), 2301-2307.

25. Geim, A. K.; Novoselov, K. S., The rise of graphene. *Nat. Mater.* **2007,** *6* (3), 183-191.

26. Compton, O. C.; Cranford, S. W.; Putz, K. W.; An, Z.; Brinson, L. C.; Buehler, M. J.; Nguyen, S. T., Tuning the mechanical properties of graphene oxide paper and its associated polymer nanocomposites by controlling cooperative intersheet hydrogen bonding. *ACS Nano* **2012,** *6* (3), 2008-2019.

27. Naraghi, M.; Bratzel, G. H.; Filleter, T.; An, Z.; Wei, X.; Nguyen, S. T.; Buehler, M. J.; Espinosa, H. D., Atomistic investigation of load transfer between DWNT bundles “crosslinked” by PMMA oligomers. *Adv. Funct. Mater.* **2013,** *23* (15), 1883-1892.

28. Paci, J. T.; Belytschko, T.; Schatz, G. C., Computational studies of the structure, behavior upon heating, and mechanical properties of graphite oxide. *J. Phys. Chem. C* **2007,** *111* (49), 18099-18111.

29. Roenbeck, M. R.; Furmanchuk, A.; An, Z.; Paci, J. T.; Wei, X.; Nguyen, S. T.; Schatz, G. C.; Espinosa, H. D., Molecular-Level Engineering of Adhesion in Carbon Nanomaterial Interfaces. *Nano Lett.* **2015,** *15* (7), 4504-4516.

30. Beese, A. M.; An, Z.; Sarkar, S.; Nathamgari, S. S. P.; Espinosa, H. D.; Nguyen, S. T., Defect-Tolerant Nanocomposites through Bio-Inspired Stiffness Modulation. *Adv. Funct. Mater.* **2014,** *24* (19), 2883-2891.

31. An, Z.; Compton, O. C.; Putz, K. W.; Brinson, L. C.; Nguyen, S. T., Bio-inspired borate cross-linking in ultra-stiff graphene oxide thin films. *Adv. Mater.* **2011,** *23* (33), 3842-3846.

32. Chen, J.; Yao, B.; Li, C.; Shi, G., An improved Hummers method for eco-friendly synthesis of graphene oxide. *Carbon* **2013,** *64*, 225-229.

33. Hummers Jr, W. S.; Offeman, R. E., Preparation of graphitic oxide. *J. Am. Chem. Soc.* **1958,** *80* (6), 1339-1339.

34. Marcano, D. C.; Kosynkin, D. V.; Berlin, J. M.; Sinitskii, A.; Sun, Z.; Slesarev, A.; Alemany, L. B.; Lu, W.; Tour, J. M., Improved synthesis of graphene oxide. *ACS Nano* **2010,** *4* (8), 4806-4814.

35. Kim, J.; Cote, L. J.; Kim, F.; Yuan, W.; Shull, K. R.; Huang, J., Graphene oxide sheets at interfaces. *J. Am. Chem. Soc.* **2010,** *132* (23), 8180-8186.

36. Cote, L. J.; Kim, F.; Huang, J., Langmuir−Blodgett assembly of graphite oxide single layers. *J. Am. Chem. Soc.* **2008,** *131* (3), 1043-1049.

37. Yang, D.; Velamakanni, A.; Bozoklu, G.; Park, S.; Stoller, M.; Piner, R. D.; Stankovich, S.; Jung, I.; Field, D. A.; Ventrice, C. A., Chemical analysis of graphene oxide films after heat and chemical treatments by X-ray photoelectron and Micro-Raman spectroscopy. *Carbon* **2009,** *47* (1), 145-152.

38. Dreyer, D. R.; Park, S.; Bielawski, C. W.; Ruoff, R. S., The chemistry of graphene oxide. *Chem. Soc. Rev.* **2010,** *39* (1), 228-240.

39. Pulido, A.; Concepción, P.; Boronat, M.; Botas, C.; Alvarez, P.; Menendez, R.; Corma, A., Reconstruction of the carbon sp 2 network in graphene oxide by low-temperature reaction with CO. *J. Mater. Chem.* **2012,** *22* (1), 51-56.

40. Koinuma, M.; Tateishi, H.; Hatakeyama, K.; Miyamoto, S.; Ogata, C.; Funatsu, A.; Taniguchi, T.; Matsumoto, Y., Analysis of reduced graphene oxides by X-ray photoelectron spectroscopy and electrochemical capacitance. *Chem. Lett.* **2013,** *42* (8), 924-926.

41. Ganguly, A.; Sharma, S.; Papakonstantinou, P.; Hamilton, J., Probing the thermal deoxygenation of graphene oxide using high-resolution in situ X-ray-based spectroscopies. *J. Phys. Chem. C* **2011,** *115* (34), 17009-17019.

42. Compton, O. C.; Dikin, D. A.; Putz, K. W.; Brinson, L. C.; Nguyen, S. T., Electrically conductive "alkylated" graphene paper via chemical reduction of amine-functionalized graphene oxide paper. *Adv. Mater.* **2010,** *22* (8), 892-896.

43. Yumitori, S., Correlation of C1s chemical state intensities with the O1s intensity in the XPS analysis of anodically oxidized glass-like carbon samples. *J. Mater. Sci.* **2000,** *35* (1), 139-146.

44. Pireaux, J.; Riga, J.; Caudano, R.; Verbist, J.; Delhalle, J.; Delhalle, S.; Andre, J.; Gobillon, Y., Polymer primary structures studied by ESCA and EHCO methods. *Phys. Scr.* **1977,** *16* (5-6), 329.

45. Williams, D. B.; Carter, C. B., The transmission electron microscope. In *Transmission electron microscopy*, Springer: 1996; pp 3-17.

46. Lerf, A.; He, H.; Forster, M.; Klinowski, J., Structure of graphite oxide revisited. *J. Phys. Chem. B* **1998,** *102* (23), 4477-4482.

47. Erickson, K.; Erni, R.; Lee, Z.; Alem, N.; Gannett, W.; Zettl, A., Determination of the local chemical structure of graphene oxide and reduced graphene oxide. *Adv. Mater.* **2010,** *22* (40), 4467-4472.

48. Meyer, J. C.; Kisielowski, C.; Erni, R.; Rossell, M. D.; Crommie, M.; Zettl, A., Direct imaging of lattice atoms and topological defects in graphene membranes. *Nano Lett.* **2008,** *8* (11), 3582-3586.

49. Ramachandramoorthy, R.; Gao, W.; Bernal, R.; Espinosa, H., High strain rate tensile testing of silver nanowires: rate-dependent brittle-to-ductile transition. *Nano Lett.* **2015,** *16* (1), 255-263.

50. Varlot, K.; Martin, J.; Quet, C., EELS analysis of PMMA at high spatial resolution. *Micron* **2001,** *32* (4), 371-378.

51. Gass, M. H.; Bangert, U.; Bleloch, A. L.; Wang, P.; Nair, R. R.; Geim, A., Free-standing graphene at atomic resolution. *Nat. Nanotechnol.* **2008,** *3* (11), 676-681.

52. Mkhoyan, K. A.; Contryman, A. W.; Silcox, J.; Stewart, D. A.; Eda, G.; Mattevi, C.; Miller, S.; Chhowalla, M., Atomic and electronic structure of graphene-oxide. *Nano Lett.* **2009,** *9* (3), 1058-1063.

53. Rezania, B.; Severin, N.; Talyzin, A. V.; Rabe, J. P., Hydration of bilayered graphene oxide. *Nano Lett.* **2014,** *14* (7), 3993-3998.

54. Xiong, R.; Hu, K.; Zhang, S.; Lu, C.; Tsukruk, V. V., Ultrastrong freestanding graphene oxide nanomembranes with surface-enhanced Raman scattering functionality by solvent-assisted single-component layer-by-layer assembly. *ACS Nano* **2016,** *10* (7), 6702-6715.

55. Tortonese, M.; Kirk, M. In *Characterization of application specific probes for SPMs*, Proc. SPIE, 1997; pp 53-60.

56. Abd El-Kader, K. A. M.; Abdel Hamied, S. F., Preparation of poly (vinyl alcohol) films with promising physical properties in comparison with commercial polyethylene film. *J. Appl. Polym. Sci.* **2002,** *86* (5), 1219-1226.

57. Abd El-Kader, K. A. M.; Hamied, S. F. A.; Mansour, A. B.; El-Lawindy, A. M. Y.; El-Tantaway, F., Effect of the molecular weights on the optical and mechanical properties of poly (vinyl alcohol) films. *Polym. Test.* **2002,** *21* (7), 847-850.

58. Xu, Y.; Hong, W.; Bai, H.; Li, C.; Shi, G., Strong and ductile poly (vinyl alcohol)/graphene oxide composite films with a layered structure. *Carbon* **2009,** *47* (15), 3538-3543.

59. Konidari, M.; Papadokostaki, K.; Sanopoulou, M., Moisture-induced effects on the tensile mechanical properties and glass-transition temperature of poly (vinyl alcohol) films. *J. Appl. Polym. Sci.* **2011,** *120* (6), 3381-3386.

60. Reddy, J. N., *Theory and Analysis of Elastic Plates and Shells*. 2nd ed.; CRC Press: Boca Raton, FL, 2006.

61. Lahaye, R. J. W. E.; Jeong, H. K.; Park, C. Y.; Lee, Y. H., Density functional theory study of graphite oxide for different oxidation levels. *Phys. Rev. B* **2009,** *79* (12), 125435.

62. Liu, L.; Wang, L.; Gao, J.; Zhao, J.; Gao, X.; Chen, Z., Amorphous structural models for graphene oxides. *Carbon* **2012,** *50* (4), 1690-1698.

63. Liu, L.; Zhang, J.; Zhao, J.; Liu, F., Mechanical properties of graphene oxides. *Nanoscale* **2012,** *4* (19), 5910-5916.

64. Wang, L.; Sun, Y.; Lee, K.; West, D.; Chen, Z.; Zhao, J.; Zhang, S., Stability of graphene oxide phases from first-principles calculations. *Phys. Rev. B.* **2010,** *82* (16), 161406.

65. Yan, J.-A.; Xian, L.; Chou, M., Structural and electronic properties of oxidized graphene. *Phys. Rev. Lett.* **2009,** *103* (8), 086802.

66. Boukhvalov, D.; Katsnelson, M., Tuning the gap in bilayer graphene using chemical functionalization: density functional calculations. *Phys. Rev. B* **2008,** *78* (8), 085413.

67. Incze, A.; Pasturel, A.; Peyla, P., Mechanical properties of graphite oxides: Ab initio simulations and continuum theory. *Phys. Rev. B* **2004,** *70* (21), 212103.

68. Wei, N.; Lv, C.; Xu, Z., Wetting of graphene oxide: A molecular dynamics study. *Langmuir* **2014,** *30* (12), 3572-3578.

69. Qiu, L.; Zhang, X.; Yang, W.; Wang, Y.; Simon, G. P.; Li, D., Controllable corrugation of chemically converted graphene sheets in water and potential application for nanofiltration. *Chem. Commun.* **2011,** *47* (20), 5810-5812.

70. Elstner, M.; Porezag, D.; Jungnickel, G.; Elsner, J.; Haugk, M.; Frauenheim, T.; Suhai, S.; Seifert, G., Self-consistent-charge density-functional tight-binding method for simulations of complex materials properties. *Phys. Rev. B* **1998,** *58* (11), 7260.

71. Kresse, G.; Furthmuller, J., Efficient iterative schemes for ab initio total-energy calculations using a plane-wave basis set. *Phys. Rev. B* **1996,** *54* (16), 11169-11186.

72. Kresse, G.; Hafner, J., Ab initio molecular dynamics for liquid metals. *Phys. Rev. B* **1993,** *47* (1), 558.

73. Kresse, G.; Joubert, D., From ultrasoft pseudopotentials to the projector augmented-wave method. *Phys. Rev. B* **1999,** *59* (3), 1758-1775.

74. Blochl, P. E., Projector Augmented-Wave Method. *Phys. Rev. B* **1994,** *50* (24), 17953-17979.

75. Plimpton, S., Fast parallel algorithms for short-range molecular dynamics. *J. Comput. Phys.* **1995,** *117* (1), 1-19.

76. Huang, L.; Seredych, M.; Bandosz, T. J.; Van Duin, A. C.; Lu, X.; Gubbins, K. E., Controllable atomistic graphene oxide model and its application in hydrogen sulfide removal. *J. Chem. Phys.* **2013,** *139* (19), 194707.

77. Sukumar, N.; Chopp, D. L.; Moës, N.; Belytschko, T., Modeling holes and inclusions by level sets in the extended finite-element method. *Comput. Methods in Appl. Mech. Eng.* **2001,** *190* (46), 6183-6200.

78. Lee, G. U.; Chrisey, L. A.; Colton, R. J., Direct measurement of the forces between complementary strands of DNA. *Science* **1994,** *266* (5186), 771-773.

79. Rief, M.; Gautel, M.; Oesterhelt, F.; Fernandez, J. M.; Gaub, H. E., Reversible unfolding of individual titin immunoglobulin domains by AFM. *Science* **1997,** *276* (5315), 1109-1112.

80. Gómez-Navarro, C.; Burghard, M.; Kern, K., Elastic properties of chemically derived single graphene sheets. *Nano Lett.* **2008,** *8* (7), 2045-2049.

81. Suk, J. W.; Piner, R. D.; An, J.; Ruoff, R. S., Mechanical properties of monolayer graphene oxide. *ACS Nano* **2010,** *4* (11), 6557-6564.

82. Li, J.-L.; Kudin, K. N.; McAllister, M. J.; Prud'homme, R. K.; Aksay, I. A.; Car, R., Oxygen-driven unzipping of graphitic materials. *Phys. Rev. Lett.* **2006,** *96* (17), 176101.

83. Ma, J.; Alfè, D.; Michaelides, A.; Wang, E., Stone-Wales defects in graphene and other planar sp^2-bonded materials. *Phys. Rev. B* **2009,** *80* (3), 033407.

84. Bhatia, N. M.; Nachbar, W., Finite indentation of an elastic membrane by a spherical indenter. *Int. J. Nonlin. Mech.* **1968,** *3* (3), 307-324.

85. Robinson, J. T.; Perkins, F. K.; Snow, E. S.; Wei, Z.; Sheehan, P. E., Reduced graphene oxide molecular sensors. *Nano Lett.* **2008,** *8* (10), 3137-3140.

86. Dua, V.; Surwade, S. P.; Ammu, S.; Agnihotra, S. R.; Jain, S.; Roberts, K. E.; Park, S.; Ruoff, R. S.; Manohar, S. K., All-organic vapor sensor using inkjet-printed reduced graphene oxide. *Angew. Chem., Int. Ed. Engl.* **2010,** *49* (12), 2154-2157.

87. Ryoo, S.-R.; Lee, J.; Yeo, J.; Na, H.-K.; Kim, Y.-K.; Jang, H.; Lee, J. H.; Han, S. W.; Lee, Y.; Kim, V. N., Quantitative and multiplexed microRNA sensing in living cells based on peptide nucleic acid and nano graphene oxide (PANGO). *ACS Nano* **2013,** *7* (7), 5882-5891.

88. Xu, J.; Wang, K.; Zu, S.-Z.; Han, B.-H.; Wei, Z., Hierarchical nanocomposites of polyaniline nanowire arrays on graphene oxide sheets with synergistic effect for energy storage. *ACS Nano* **2010,** *4* (9), 5019-5026.

89. Luo, Z.; Vora, P. M.; Mele, E. J.; Johnson, A. C.; Kikkawa, J. M., Photoluminescence and band gap modulation in graphene oxide. *Appl. Phys. Lett.* **2009,** *94* (11), 111909.

90. Kuila, T.; Mishra, A. K.; Khanra, P.; Kim, N. H.; Lee, J. H., Recent advances in the efficient reduction of graphene oxide and its application as energy storage electrode materials. *Nanoscale* **2013,** *5* (1), 52-71.

91. Medhekar, N. V.; Ramasubramaniam, A.; Ruoff, R. S.; Shenoy, V. B., Hydrogen bond networks in graphene oxide composite paper: structure and mechanical properties. *ACS Nano* **2010,** *4* (4), 2300-2306.

92. Peng, B.; Locascio, M.; Zapol, P.; Li, S.; Mielke, S. L.; Schatz, G. C.; Espinosa, H. D., Measurements of near-ultimate strength for multiwalled carbon nanotubes and irradiation-induced crosslinking improvements. *Nat. Nanotechnol.* **2008,** *3* (10), 626-631.

93. Zhao, H.; Min, K.; Aluru, N. R., Size and chirality dependent elastic properties of graphene nanoribbons under uniaxial tension. *Nano Lett.* **2009,** *9* (8), 3012-3015.

94. Frauenheim, T.; Seifert, G.; Elstner, M.; Niehaus, T.; Köhler, C.; Amkreutz, M.; Sternberg, M.; Hajnal, Z.; Di Carlo, A.; Suhai, S., Atomistic simulations of complex materials: ground-state and excited-state properties. *J. Phys.: Condens. Matter* **2002,** *14* (11), 3015.

95. Liu, Y. L.; Xie, B.; Zhang, Z.; Zheng, Q. S.; Xu, Z. P., Mechanical properties of graphene papers. *J Mech Phys Solids* **2012,** *60* (4), 591-605.

96. Li, T.; Huang, Z.; Xi, Z.; Lacour, S. P.; Wagner, S.; Suo, Z., Delocalizing strain in a thin metal film on a polymer substrate. *Mech. Mater.* **2005,** *37* (2), 261-273.

97. Li, T.; Suo, Z., Ductility of thin metal films on polymer substrates modulated by interfacial adhesion. *Int. J. Solids Struct.* **2007,** *44* (6), 1696-1705.

98. Budiansky, B.; Evans, A. G.; Hutchinson, J. W., Fiber-matrix debonding effects oncracking in aligned fiber ceramic composites. *Int. J. Solids Struct.* **1995,** *32* (3-4), 315-328.

99. Evans, A. G.; He, M. Y.; Hutchinson, J. W., Interface debonding and fiber cracking in brittle matrix composites. *J. Am. Ceram. Soc.* **1989,** *72* (12), 2300-2303.

100. Budiansky, B.; Hutchinson, J. W.; Evans, A. G., Matrix fracture in fiber-reinforced ceramics. *J Mech Phys Solids* **1986,** *34* (2), 167-189.

101. Stannard, A., Dewetting-mediated pattern formation in nanoparticle assemblies. *J. Phys.: Condens. Matter* **2011,** *23* (8), 083001.

102. Konnur, R.; Kargupta, K.; Sharma, A., Instability and morphology of thin liquid films on chemically heterogeneous substrates. *Phys. Rev. Lett.* **2000,** *84* (5), 931-934.

103. Putz, K. W.; Compton, O. C.; Palmeri, M. J.; Nguyen, S. T.; Brinson, L. C., High-nanofiller-content graphene oxide–polymer nanocomposites via vacuum-assisted self-assembly. *Adv. Funct. Mater.* **2010,** *20* (19), 3322-3329.

104. Budiansky, B.; Amazigo, J. C., Toughening by aligned, frictionally constrained fibers. *J Mech Phys Solids* **1989,** *37* (1), 93-109.

105. Budiansky, B.; Amazigo, J. C.; Evans, A. G., Small-scale crack bridging and the fracture toughness of particulate-reinforced ceramics. *J Mech Phys Solids* **1988,** *36* (2), 167-187.

106. Kou, L.; Gao, C., Bioinspired design and macroscopic assembly of poly (vinyl alcohol)-coated graphene into kilometers-long fibers. *Nanoscale* **2013,** *5* (10), 4370-4378.

Appendix A: Python Function for Graphene Model Generation

Below is a copy of the Python function written to generate graphene models for the work presented herein.

```
def model_gen(a, lx_flake, ly_flake, z_coord):
	# Import the relevant libraries
	import os
	import math
	import numpy
	#----------------------------------
	# Input the desired system lengths
	lx = lx_flake;
	ly = ly_flake;
	z = z_coord;
	filename = 'graphene.xyz';
	#----------------------------------
	# Define the C-C bond length (in angstroms)
	ao_cc = a;

	# Perform internal calculations
	lx_pos = lx/2+0.5*ao_cc;
	lx_neg = -lx/2;
	ly_pos = ly/2;
	ly_neg = -ly_pos;

	# Define dummy blank arrays
	xn_pos = [];
	xn_neg = [];

	# PRESCRIBED INITIAL POSITION
	# DO NOT CHANGE THIS UNDER ANY CIRCUMSTANCES
	xn_pos.insert(0, 0);
	xn_pos.insert(1, 1);
	xn_neg.insert(0, -2);
	xn_neg.insert(1, -3);

	# Counter initialization
	xn_pos_current = 0;
	xn_neg_current = 0;
	yn_pos_current = 0;
	yn_neg_current = 0;
	#-----------------------------------
	# Even x-coordinates generation block

	nx_pos = 0;

	while (xn_pos_current * ao_cc) <= lx_pos:
		xn_pos_current = xn_pos[nx_pos + 1] + (2)/( xn_pos[nx_pos + 1] - xn_pos[nx_pos] );
		xn_pos.append(xn_pos_current);
		nx_pos = nx_pos + 1;
```

```
nx_neg = 0;

while (xn_neg_current * ao_cc) >= lx_neg:
      xn_neg_current = xn_neg[nx_neg + 1] - (2)/( xn_neg[nx_neg] - xn_neg[nx_neg + 1] );
      xn_neg.append(xn_neg_current);
      nx_neg = nx_neg + 1;
#-----------------------------------
# Even y-coordinate generation block

ny_pos = 0;
yn_pos = [];

while (yn_pos_current * ao_cc) <= ly_pos:
            yn_pos_current = 2 * ny_pos * math.sin(math.pi/3);
            yn_pos.append(yn_pos_current);
            ny_pos = ny_pos + 1;

ny_neg = 1;
yn_neg = [];

while (yn_neg_current * ao_cc) >= ly_neg:
            yn_neg_current = -2 * ny_neg * math.sin(math.pi/3);
            yn_neg.append(yn_neg_current);
            ny_neg = ny_neg + 1;
#-------------------------------------------------------------
# Global even x-coordinate amd y-coordinate generation block

# Generate empty arrays
xeven = [];
yeven = [];

for xglob in range (0, len(xn_pos)):
            xeven.append(ao_cc * xn_pos[xglob]);

for xglob in range (0, len(xn_neg)):
            xeven.append(ao_cc * xn_neg[xglob]);

for yglob in range (0, len(yn_pos)):
            yeven.append(ao_cc * yn_pos[yglob]);

for yglob in range (0, len(yn_neg)):
      yeven.append(ao_cc * yn_neg[yglob]);

xeven = sorted(xeven);
yeven = sorted(yeven);
#-------------------------------------------------------------
# Global odd x-coordinate and y-coordinate generation block

# Generate empty arrays
xodd = [];
yodd = [];

for xglob in range (0, len(xeven) - 1):
            xodd.append(xeven[xglob] + 3 * ao_cc * math.cos(math.pi/3));
```

```
        for yglob in range (0, len(yeven)):
                yodd.append(yeven[yglob] + ao_cc * math.sin(math.pi/3));
        #-------------------------------------------------------------
        # Assemble even coordinates

        # Declare empty data array
        numat = ( len(xeven)-1 ) * len(yeven) + len(xodd) * len(yodd);
        printarray = numpy.zeros((numat, 4));

        # Declare counter
        printat = 0;

        for printy in range (0, len(yeven)):
                for printx in range (1, len(xeven)):
                        printarray[printat][0] = printat + 1;
                        printarray[printat][1] = xeven[printx];
                        printarray[printat][2] = yeven[printy];
                        printarray[printat][3] = z;
                        printat = printat + 1;
        #-------------------------------------
        # Assemble odd coordinates

        for printy in range (0, len(yodd)):
        for printx in range (0, len(xodd)):
              printarray[printat][0] = printat + 1;
              printarray[printat][1] = xodd[printx];
              printarray[printat][2] = yodd[printy];
              printarray[printat][3] = z;
              printat = printat + 1;
        # -------------------------------------
        # Print data file

        # Obtain system information
        num_c_atoms = len(printarray);

        # Open output file
        output = open(filename, 'w');
        output.write(str(num_c_atoms));
        output.write('\n');

        for at_print in range (0, num_c_atoms):
                output.write('\nC ' + str(printarray[at_print][1]) + ' ' + str(printarray[at_print][2]) + ' ' +
str(printarray[at_print][3]));

        output.close();
    #-----------------------------
        # Find coordinates of interest
        x_m = min(printarray[:, 1]);
        x_p = max(printarray[:, 1]);
        x_p = x_p + a;
        y_m = min(printarray[:, 2]);
        y_p = max(printarray[:, 2]);
        y_p = y_p + math.sqrt(3)/2*a;

        lx = (x_p - x_m);
```

```
ly = (y_p - y_m);

return [x_m, x_p, y_m, y_p, lx, ly];
```

The execution code for this function is as follows

```
import make_graphene
import oxidation_fun
import math

a = 1.42;
lx_flake = 202;
ly_flake = 202;
z_coord = 0;

[x_m, x_p, y_m, y_p, lx, ly] = make_graphene.model_gen(a, lx_flake, ly_flake, z_coord);

lx_p = lx
ly_p = ly

print 'Minimum x'
print x_m
print 'Maximum x'
print x_p
print 'Minimum y'
print y_m
print 'Maximum y'
print y_p
print '\n\nBox Length, x'
print lx_p
print 'Box Length, y'
print ly_p
print '\n\nCODE EXECUTION COMPLETE\n\n'
```

Appendix B: Python Code for Addition of Hydroxyl Groups to Graphene Basal Plane

Below is a copy of the Python function written to add hydroxyl functional groups to graphene or GO models for the work presented herein.

```
# Import the relevant libraries
import os
import math
import numpy
import random
import sys

def oxi_fun(filename, output_name, epox_side, alc_side, x_max, y_max, do_square, lx_p, ly_p):
    #-----------------------------------------------
    # Convert the xyz dataset to a temporary dataset
    # THIS COULD BE GENERALIZED IN THE FUTURE FOR VERY BROAD APPLICATIONS.

    # Open data file and load information temporally
    temp_file = open(filename, 'r');
    temp_data = temp_file.readlines();

    # Read number of atoms
    num_at = int(temp_data[0].split(' ')[0]);

    # Initialize the recipient array
    dataset = numpy.zeros((num_at, 5));

    # Load the data set using Python functions
    # Here, we adopt the atom ID numeration:
    # 1 - C atom
    # 2 - O atom
    # 3 - H atom
    for line in range (2, num_at + 2):
        dataset[line - 2][0] = (line - 1);
        dataset[line - 2][2] = temp_data[line].split()[1];
        dataset[line - 2][3] = temp_data[line].split()[2];
        dataset[line - 2][4] = temp_data[line].split()[3];
        atom_type = temp_data[line].split()[0];
        if atom_type == 'C':
            dataset[line - 2][1] = 1;
        elif atom_type == 'O':
            dataset[line - 2][1] = 2;
        elif atom_type == 'H':
            dataset[line - 2][1] = 3;
        else:
            sys.exit('Unexpected atom atom_type. Could not write information.')
    #-----------------------------------------------
    # Calculate the species present in the system
    num_c_atoms = len(numpy.where(dataset[:, 1] == 1)[0]);
    num_o_atoms = len(numpy.where(dataset[:, 1] == 2)[0]);
    num_h_atoms = len(numpy.where(dataset[:, 1] == 3)[0]);
    num_alc_g = num_h_atoms;
```

```
num_epox_g = num_o_atoms - num_h_atoms;
#--------------------------------------
# Define GO characteristics
ao_cc = 1.42;
ao_co = 1.43;
ao_oh = 0.95;
h_epox = math.sqrt(math.pow(ao_co, 2) - math.pow(ao_cc / 2, 2));

# Define oxidation parameters
atoms_added = 2 * epox_side + 4 * alc_side;
#---------------------------------------------
# Generate neighbor list for the current system

# Generate empty neighbor list for C atoms only (connectivity)
neigh_list = numpy.zeros((num_c_atoms, 5));

for c_counter in range (0, num_c_atoms):
      neigh_num = 2;
      neigh_list[c_counter, 0] = dataset[c_counter, 0];
      neigh_list[c_counter, 1] = neigh_num - 2;
      for neigh_check in range (0, num_c_atoms):
            if neigh_check != c_counter:
               bonds = [];
               dist_x = dataset[neigh_check, 2] - dataset[c_counter, 2];
               dist_x_p = dataset[neigh_check, 2] - dataset[c_counter, 2] + lx_p;
               dist_x_m = dataset[neigh_check, 2] - dataset[c_counter, 2] - lx_p;
               dist_y = dataset[neigh_check, 3] - dataset[c_counter, 3];
               dist_y_p = dataset[neigh_check, 3] - dataset[c_counter, 3] + ly_p;
               dist_y_m = dataset[neigh_check, 3] - dataset[c_counter, 3] - ly_p;
               r1 = math.sqrt(math.pow(dist_x, 2) + math.pow(dist_y, 2));
               r2 = math.sqrt(math.pow(dist_x_p, 2) + math.pow(dist_y, 2));
               r3 = math.sqrt(math.pow(dist_x_m, 2) + math.pow(dist_y, 2));
               r4 = math.sqrt(math.pow(dist_x, 2) + math.pow(dist_y_p, 2));
               r5 = math.sqrt(math.pow(dist_x, 2) + math.pow(dist_y_m, 2));
               bonds.insert(0, r1);
               bonds.insert(1, r2);
               bonds.insert(2, r3);
               bonds.insert(3, r4);
               bonds.insert(4, r5);
               r = min(bonds);
               if (r - ao_cc <= 1.0E-3):
                  neigh_num = neigh_num + 1;
                  neigh_list[c_counter, 1] = neigh_num - 2;
                  neigh_list[c_counter, neigh_num - 1] = dataset[neigh_check, 0];

max_x = numpy.amax(dataset[:, 2]);
min_x = numpy.amin(dataset[:, 2]);
max_y = numpy.amax(dataset[:, 3]);
min_y = numpy.amin(dataset[:, 3]);
x_shift = (max_x + min_x) * 0.5;
y_shift = (max_y + min_y) * 0.5;
#-----------------------------------------------------------------------------------
# Generate list of system C atoms
if do_square == 1:
      c_atom_avail = numpy.zeros((num_c_atoms, 4));
```

```
        avail = 0;
        for k in range (0, num_c_atoms):
            x = dataset[k, 2] - x_shift;
      y = dataset[k, 3] - y_shift;
      if ((abs(x) - x_max) <= 1E-3) and ((abs(y) - y_max) <= 1E-3):
            c_atom_avail[avail, 0] = dataset[k, 0];
            avail = avail + 1;
        random.seed();
        loc_switch = 0;
        for k in range (0, num_c_atoms):
      loc = c_atom_avail[k, 0];
      if loc == 0 and loc_switch == 0:
          loc_switch = 1;
            loc_array = k;

        c_atom_avail = c_atom_avail[0 : loc_array, :];
        c_atom_avail[:, 0] = sorted(c_atom_avail[:, 0], key=lambda k: random.random());
else:
   c_atom_avail = numpy.zeros((num_c_atoms, 4));
   random.seed();
   c_atom_avail[:, 0] = sorted(dataset[0 : num_c_atoms, 0], key=lambda k: random.random());
#---------------------------------------------------------------------------
# Generate used (functionalized) C atoms list

# First, generate the arrays
num_occ_c = 2 * num_epox_g + num_alc_g;
used_c_atoms = numpy.zeros((num_occ_c + 4 * epox_side + 2 * alc_side, 1));
used_counter = -1;

for c_counter in range (0, num_c_atoms):
      for used_check in range (num_c_atoms, len(dataset)):
            dist_x = dataset[used_check, 2] - dataset[c_counter, 2];
            dist_y = dataset[used_check, 3] - dataset[c_counter, 3];
            dist_z = dataset[used_check, 4] - dataset[c_counter, 4];
            r = math.sqrt(math.pow(dist_x, 2) + math.pow(dist_y, 2) + math.pow(dist_z, 2));
            if (abs(r - ao_co) <= 1.0E-3 and r > 0 and abs(abs(dataset[used_check, 4]) - ao_co) <= 1.0E-3):
                  used_counter = used_counter + 1;
                  used_c_atoms[used_counter, 0] = c_counter + 1;
                  pos = numpy.where(c_atom_avail[:, 0] == (c_counter + 1))[0];
                  c_atom_avail[pos, 1] = 1;
                  if (dataset[used_check, 4] > 0):
                        c_atom_avail[pos, 3] = 1;
                  elif (dataset[used_check, 4] < 0):
                        c_atom_avail[pos, 3] = 2;
                  else:
                        c_atom_avail[pos, 3] = 0;
      for used_check in range (num_c_atoms, len(dataset)):
            dist_x = dataset[used_check, 2] - dataset[c_counter, 2];
            dist_y = dataset[used_check, 3] - dataset[c_counter, 3];
            dist_z = dataset[used_check, 4] - dataset[c_counter, 4];
            r = math.sqrt(math.pow(dist_x, 2) + math.pow(dist_y, 2) + math.pow(dist_z, 2));
            if (abs(r - ao_co) <= 1.0E-3 and r > 0 and abs(abs(dataset[used_check, 4]) - h_epox) <= 1.0E-6):
                  used_counter = used_counter + 1;
                  used_c_atoms[used_counter, 0] = c_counter + 1;
                  pos = numpy.where(c_atom_avail[:, 0] == (c_counter + 1))[0];
```

```
                    c_atom_avail[pos, 2] = 1;
#-------------------------------------------------
# Addition of top alcohol groups

# Initialize arrays and counters
alc_pos_top = numpy.zeros((alc_side, 1));
atom_num = 0;

for atom_gen in range (1, alc_side + 1):
      overlap_check = 1;
      while overlap_check == 1:
            conflict_check = 0;
            atom_id = c_atom_avail[atom_num, 0];
            usage_check = len(numpy.where(used_c_atoms == atom_id)[0]);
            neigh_num = neigh_list[atom_id - 1, 1];
            for counter in range (1, int(neigh_num + 1)):
                  neigh_id = neigh_list[atom_id - 1, counter + 1];
                  pos = numpy.where(c_atom_avail[:, 0] == neigh_id)[0];
                  if (c_atom_avail[pos, 3] != 1):
                        conflict_check = conflict_check + 1;
            if ((conflict_check == neigh_num) and (usage_check == 0)):
                  alc_pos_top[atom_gen - 1, 0] = atom_id
                  c_atom_avail[atom_num, 1] = 1;
                  used_counter = used_counter + 1;
                  used_c_atoms[used_counter] = c_atom_avail[atom_num, 0];
                  overlap_check = 0;
                  c_atom_avail[atom_num, 3] = 1;
                  atom_num = atom_num + 1;
            else:
                  atom_num = atom_num + 1;
#-------------------------------------------------
# Addition of bottom alcohol groups

# Initialize arrays and counters
alc_pos_bottom = numpy.zeros((alc_side, 1));
atom_num = 0;

for atom_gen in range (1, alc_side + 1):
      overlap_check = 1;
      while overlap_check == 1:
            conflict_check = 0;
            atom_id = c_atom_avail[atom_num, 0];
            usage_check = len(numpy.where(used_c_atoms == atom_id)[0]);
            neigh_num = neigh_list[atom_id - 1, 1];
            for counter in range (1, int(neigh_num + 1)):
                  neigh_id = neigh_list[atom_id - 1, counter + 1];
                  pos = numpy.where(c_atom_avail[:, 0] == neigh_id)[0];
                  if (c_atom_avail[pos, 3] != 2):
                        conflict_check = conflict_check + 1;
            if ((conflict_check == neigh_num) and (usage_check == 0)):
                  alc_pos_bottom[atom_gen - 1] = atom_id
                  c_atom_avail[atom_num, 1] = 1;
                  used_counter = used_counter + 1;
                  used_c_atoms[used_counter] = c_atom_avail[atom_num, 0];
                  overlap_check = 0;
```

```
                c_atom_avail[atom_num, 3] = 2;
                atom_num = atom_num + 1;
        else:
                atom_num = atom_num + 1;
#-----------------------------------------------
# Addition of top epoxide groups

# Initialize arrays and counters
epox_pos_top = numpy.zeros((epox_side, 2));
atom_num = 0;

for atom_gen in range (1, epox_side + 1):
    overlap_check = 1;
    while overlap_check == 1:
        neigh_toggle = 0;
        atom_id = c_atom_avail[atom_num, 0];
        usage_check = len(numpy.where(used_c_atoms == atom_id)[0]);
        neigh_num = neigh_list[atom_id - 1, 1];
        temp_array = numpy.zeros((neigh_num, 1));
        for neigh_curr in range (1, int(neigh_num + 1)):
            neigh_check = len(numpy.where(used_c_atoms == (neigh_list[atom_id - 1, 1 + neigh_curr]))[0]);
            if (usage_check == 0 and neigh_check == 0):
                temp_array[neigh_toggle, 0] = neigh_list[atom_id - 1, 1 + neigh_curr];
                neigh_toggle = neigh_toggle + 1;
        temp_array = temp_array[temp_array != 0];
        if len(temp_array) != 0:
            rand_neigh = random.randint(0, neigh_toggle - 1);
            epox_pos_top[atom_gen - 1, 0] = atom_id;
            epox_pos_top[atom_gen - 1, 1] = temp_array[rand_neigh];
            used_counter = used_counter + 1;
            used_c_atoms[used_counter] = epox_pos_top[atom_gen - 1, 0];
            used_c_atoms[used_counter + epox_side] = epox_pos_top[atom_gen - 1, 1];
            c_atom_avail[atom_num, 2] = 1;
            pos = numpy.where(temp_array[rand_neigh] == c_atom_avail);
            c_atom_avail[pos, 2] = 1;
            atom_num = atom_num + 1;
            overlap_check = 0;
        else:
            atom_num = atom_num + 1;
#-----------------------------------------------
# Addition of bottom epoxide groups

# Initialize arrays and counters
epox_pos_bottom = numpy.zeros((epox_side, 2));
used_counter = used_counter + epox_side;
atom_num = 0;

for atom_gen in range (1, epox_side + 1):
    overlap_check = 1;
    while overlap_check == 1:
        neigh_toggle = 0;
        atom_id = c_atom_avail[atom_num, 0];
        usage_check = len(numpy.where(used_c_atoms == atom_id)[0]);
        neigh_num = neigh_list[atom_id - 1, 1];
        temp_array = numpy.zeros((neigh_num, 1));
```

```
            for neigh_curr in range (1, int(neigh_num + 1)):
                neigh_check = len(numpy.where(used_c_atoms == (neigh_list[atom_id - 1, 1 + neigh_curr]))[0]);
                if (usage_check == 0 and neigh_check == 0):
                    temp_array[neigh_toggle, 0] = neigh_list[atom_id - 1, 1 + neigh_curr];
                    neigh_toggle = neigh_toggle + 1;
            temp_array = temp_array[temp_array != 0];
            if len(temp_array) != 0:
                rand_neigh = random.randint(0, neigh_toggle - 1);
                epox_pos_bottom[atom_gen - 1, 0] = atom_id;
                epox_pos_bottom[atom_gen - 1, 1] = temp_array[rand_neigh];
                used_counter = used_counter + 1;
                used_c_atoms[used_counter] = epox_pos_bottom[atom_gen - 1, 0];
                used_c_atoms[used_counter + epox_side] = epox_pos_bottom[atom_gen - 1, 1];
                c_atom_avail[atom_num, 2] = 1;
                pos = numpy.where(temp_array[rand_neigh] == c_atom_avail);
                c_atom_avail[pos, 2] = 1;
                atom_num = atom_num + 1;
                overlap_check = 0;
            else:
                atom_num = atom_num + 1;
    #-----------------------------------------------
    # Generation of oxygen atom coordinates

    # Generate the new printing array
    printarray = numpy.zeros((len(dataset) + atoms_added, 5));
    printarray[0 : len(dataset), :] = dataset;

    # Initialize the counter in appropiate location
    print_atom = (len(dataset) + 1) - 1;

    # Assemble the top basal plane oxygen atoms for OH groups
    for alc_top_count in range (1, alc_side + 1):
        printarray[print_atom, 0] = print_atom + 1;
        printarray[print_atom, 1] = 2;
        printarray[print_atom, 2] = printarray[alc_pos_top[alc_top_count - 1, 0] - 1, 2];
        printarray[print_atom, 3] = printarray[alc_pos_top[alc_top_count - 1, 0] - 1, 3];
        printarray[print_atom, 4] = printarray[alc_pos_top[alc_top_count - 1, 0] - 1, 4] + ao_co;
        print_atom = print_atom + 1;

    # Assemble the bottom basal plane oxygen atoms for OH groups
    for alc_bottom_count in range (1, alc_side + 1):
        printarray[print_atom, 0] = print_atom + 1;
        printarray[print_atom, 1] = 2;
        printarray[print_atom, 2] = printarray[alc_pos_bottom[alc_bottom_count - 1, 0] - 1, 2];
        printarray[print_atom, 3] = printarray[alc_pos_bottom[alc_bottom_count - 1, 0] - 1, 3];
        printarray[print_atom, 4] = printarray[alc_pos_bottom[alc_bottom_count - 1, 0] - 1, 4] - ao_co;
        print_atom = print_atom + 1;

    # Assemble the top basal plane oxygen atoms for epoxide groups
    for epox_top_count in range (1, epox_side + 1):
        printarray[print_atom, 0] = print_atom + 1;
        printarray[print_atom, 1] = 2;
        printarray[print_atom, 2] = (printarray[epox_pos_top[epox_top_count - 1, 0] - 1, 2] +
printarray[epox_pos_top[epox_top_count - 1, 1] - 1, 2])/2 ;
```

```
        printarray[print_atom, 3] = (printarray[epox_pos_top[epox_top_count - 1, 0] - 1, 3] + printarray[epox_pos_top[epox_top_count - 1, 1] - 1, 3])/2;
        printarray[print_atom, 4] = printarray[epox_pos_top[epox_top_count - 1, 0] - 1, 4] + h_epox;
        print_atom = print_atom + 1;

    # Assemble the bottom basal plane oxygen atoms for epoxide groups
    for epox_bottom_count in range (1, epox_side + 1):
        printarray[print_atom, 0] = print_atom + 1;
        printarray[print_atom, 1] = 2;
        printarray[print_atom, 2] = (printarray[epox_pos_bottom[epox_bottom_count - 1, 0] - 1, 2] + printarray[epox_pos_bottom[epox_bottom_count - 1, 1] - 1, 2])/2 ;
        printarray[print_atom, 3] = (printarray[epox_pos_bottom[epox_bottom_count - 1, 0] - 1, 3] + printarray[epox_pos_bottom[epox_bottom_count - 1, 1] - 1, 3])/2;
        printarray[print_atom, 4] = printarray[epox_pos_bottom[epox_bottom_count - 1, 0] - 1, 4] - h_epox;
        print_atom = print_atom + 1;

    # Calculate the "number of oxygen atoms" (offset by 2 due to Python indexing)
    # Added to facilitate H atom addition in the printing step
    num_o_atoms = print_atom - len(dataset);
    #----------------------------------------
    # Generation of hydrogen atom coordinates

    for h_alc_top_count in range (1, alc_side + 1):
        printarray[print_atom, 0] = print_atom + 1;
        printarray[print_atom, 1] = 3;
        printarray[print_atom, 2] = printarray[print_atom - num_o_atoms, 2];
        printarray[print_atom, 3] = printarray[print_atom - num_o_atoms, 3];
        printarray[print_atom, 4] = printarray[print_atom - num_o_atoms, 4] + ao_oh;
        print_atom = print_atom + 1;

    for h_alc_bottom_count in range (1, alc_side + 1):
        printarray[print_atom, 0] = print_atom + 1;
        printarray[print_atom, 1] = 3;
        printarray[print_atom, 2] = printarray[print_atom - num_o_atoms, 2];
        printarray[print_atom, 3] = printarray[print_atom - num_o_atoms, 3];
        printarray[print_atom, 4] = printarray[print_atom - num_o_atoms, 4] - ao_oh;
        print_atom = print_atom + 1;
    #-----------------------------------
    # Output file generation

    # Obtain system information
    num_atoms = len(printarray);

    # Open output file
    output = open(output_name, 'w');
    output.write(str(num_atoms));
    output.write('\n');

    for at_print in range (0, num_atoms):
        if printarray[at_print, 1] == 1:
            output.write('\nC  ' + str(printarray[at_print][2]) + ' ' + str(printarray[at_print][3]) + ' ' + str(printarray[at_print][4]));
        elif printarray[at_print, 1] == 2:
            output.write('\nO  ' + str(printarray[at_print][2]) + ' ' + str(printarray[at_print][3]) + ' ' + str(printarray[at_print][4]));
```

```
        elif printarray[at_print, 1] == 3:
            output.write('\nH  ' + str(printarray[at_print][2]) + ' ' + str(printarray[at_print][3]) + ' ' + str(printarray[at_print][4]));

    output.close();
```

The execution code for this function is as follows

```
import oxidation_fun

filename = 'graphene.xyz'
output_name = 'sheet_1.xyz'
lx_p = 204.48
ly_p = 209.0585325
epox_side = 0; # NEVER CHANGE THIS ENTRY FROM 0
alc_side = 635;
# Begin code snippet
# The following 3 lines let you oxidize only side a rectangular region of lengths lx and ly, whose center is in the middle of the graphene sheet.
x_max = 100; # CAN BE USED IF DESIRE, SET BOX LENGTH IN X
y_max = 100; # CAN BE USED IF DESIRE, SET BOX LENGTH IN Y
do_square = 0; # CAN BE USED IF DESIRE. THIS IS A BOOLEAN FLAG.
# End code snippet

oxidation_fun.oxi_fun(filename,output_name,epox_side,alc_side, x_max, y_max, do_square, lx_p, ly_p);
```

Appendix C: Python Code for Addition of Epoxide Groups to Graphene Basal Plane

Below is a copy of the Python function written to add epoxide functional groups to graphene or GO models for the work presented herein.

```
# Import the relevant libraries
import os
import math
import numpy
import random
import sys

def oxi_fun(filename, output_name, epox_side, alc_side, x_max, y_max, do_square):
   #-----------------------------------------------
   # Convert the xyz dataset to a temporary dataset
   # THIS COULD BE GENERALIZED IN THE FUTURE FOR VERY BROAD APPLICATIONS.

   # Open data file and load information temporally
   temp_file = open(filename, 'r');
   temp_data = temp_file.readlines();

   # Read number of atoms
   num_at = int(temp_data[0].split(' ')[0]);

   # Initialize the recipient array
   dataset = numpy.zeros((num_at, 5));

   # Load the data set using Python functions
   # Here, we adopt the atom ID numeration:
   # 1 - C atom
   # 2 - O atom
   # 3 - H atom
   for line in range (2, num_at + 2):
         dataset[line - 2][0] = (line - 1);
         dataset[line - 2][2] = temp_data[line].split()[1];
         dataset[line - 2][3] = temp_data[line].split()[2];
         dataset[line - 2][4] = temp_data[line].split()[3];
         atom_type = temp_data[line].split()[0];
         if atom_type == 'C':
               dataset[line - 2][1] = 1;
         elif atom_type == 'O':
               dataset[line - 2][1] = 2;
         elif atom_type == 'H':
               dataset[line - 2][1] = 3;
         else:
               sys.exit('Unexpected atom atom_type. Could not write information.')
   #-----------------------------------------------
   # Calculate the species present in the system
   num_c_atoms = len(numpy.where(dataset[:, 1] == 1)[0]);
   num_o_atoms = len(numpy.where(dataset[:, 1] == 2)[0]);
   num_h_atoms = len(numpy.where(dataset[:, 1] == 3)[0]);
   num_alc_g = num_h_atoms;
```

```
num_epox_g = num_o_atoms - num_h_atoms;
#--------------------------------------
# Define GO characteristics
ao_cc = 1.42;
ao_co = 1.43;
ao_oh = 0.95;
h_epox = math.sqrt(math.pow(ao_co, 2) - math.pow(ao_cc / 2, 2));

# Define oxidation parameters
atoms_added = 2 * epox_side + 4 * alc_side;
#---------------------------------------------
# Generate neighbor list for the current system

# Generate empty neighbor list for C atoms only (connectivity)
neigh_list = numpy.zeros((num_c_atoms, 5));

for c_counter in range (0, num_c_atoms):
      neigh_num = 2;
      neigh_list[c_counter, 0] = dataset[c_counter, 0];
      neigh_list[c_counter, 1] = neigh_num - 2;
      for neigh_check in range (0, num_c_atoms):
            dist_x = dataset[neigh_check, 2] - dataset[c_counter, 2];
            dist_y = dataset[neigh_check, 3] - dataset[c_counter, 3];
            r = math.sqrt(math.pow(dist_x, 2) + math.pow(dist_y, 2));
            if (abs(r - ao_cc) <= 1.0E-3 and r > 0):
                  neigh_num = neigh_num + 1;
                  neigh_list[c_counter, 1] = neigh_num - 2;
                  neigh_list[c_counter, neigh_num - 1] = dataset[neigh_check, 0];

max_x = numpy.amax(dataset[:, 2]);
min_x = numpy.amin(dataset[:, 2]);
max_y = numpy.amax(dataset[:, 3]);
min_y = numpy.amin(dataset[:, 3]);
x_shift = (max_x + min_x) * 0.5;
y_shift = (max_y + min_y) * 0.5;
#-----------------------------------------------------------------------------------------
# Generate list of system C atoms
if do_square == 1:
        c_atom_avail = numpy.zeros((num_c_atoms, 4));
        avail = 0;
        for k in range (0, num_c_atoms):
           x = dataset[k, 2] - x_shift;
      y = dataset[k, 3] - y_shift;
      if ((abs(x) - x_max) <= 1E-3) and ((abs(y) - y_max) <= 1E-3):
            c_atom_avail[avail, 0] = dataset[k, 0];
            avail = avail + 1;
        random.seed();
        loc_switch = 0;
        for k in range (0, num_c_atoms):
      loc = c_atom_avail[k, 0];
      if loc == 0 and loc_switch == 0:
           loc_switch = 1;
            loc_array = k;

        c_atom_avail = c_atom_avail[0 : loc_array, :];
```

```
        c_atom_avail[:, 0] = sorted(c_atom_avail[:, 0], key=lambda k: random.random());
else:
   c_atom_avail = numpy.zeros((num_c_atoms, 4));
   random.seed();
   c_atom_avail[:, 0] = sorted(dataset[0 : num_c_atoms, 0], key=lambda k: random.random());
#-----------------------------------------------------------------------
# Generate used (functionalized) C atoms list

# First, generate the arrays
num_occ_c = 2 * num_epox_g + num_alc_g;
used_c_atoms = numpy.zeros((num_occ_c + 4 * epox_side + 2 * alc_side, 1));
used_counter = -1;

for c_counter in range (0, num_c_atoms):
      for used_check in range (num_c_atoms, len(dataset)):
            dist_x = dataset[used_check, 2] - dataset[c_counter, 2];
            dist_y = dataset[used_check, 3] - dataset[c_counter, 3];
            dist_z = dataset[used_check, 4] - dataset[c_counter, 4];
            r = math.sqrt(math.pow(dist_x, 2) + math.pow(dist_y, 2) + math.pow(dist_z, 2));
            if (abs(r - ao_co) <= 1.0E-3 and r > 0 and abs(abs(dataset[used_check, 4]) - ao_co) <= 1.0E-3):
                  used_counter = used_counter + 1;
                  used_c_atoms[used_counter, 0] = c_counter + 1;
                  pos = numpy.where(c_atom_avail[:, 0] == (c_counter + 1))[0];
                  c_atom_avail[pos, 1] = 1;
                  if (dataset[used_check, 4] > 0):
                        c_atom_avail[pos, 3] = 1;
                  elif (dataset[used_check, 4] < 0):
                        c_atom_avail[pos, 3] = 2;
                  else:
                        c_atom_avail[pos, 3] = 0;
      for used_check in range (num_c_atoms, len(dataset)):
            dist_x = dataset[used_check, 2] - dataset[c_counter, 2];
            dist_y = dataset[used_check, 3] - dataset[c_counter, 3];
            dist_z = dataset[used_check, 4] - dataset[c_counter, 4];
            r = math.sqrt(math.pow(dist_x, 2) + math.pow(dist_y, 2) + math.pow(dist_z, 2));
            if (abs(r - ao_co) <= 1.0E-3 and r > 0 and abs(abs(dataset[used_check, 4]) - h_epox) <= 1.0E-6):
                  used_counter = used_counter + 1;
                  used_c_atoms[used_counter, 0] = c_counter + 1;
                  pos = numpy.where(c_atom_avail[:, 0] == (c_counter + 1))[0];
                  c_atom_avail[pos, 2] = 1;
#-------------------------------------------------
# Addition of top alcohol groups

# Initialize arrays and counters
alc_pos_top = numpy.zeros((alc_side, 1));
atom_num = 0;

for atom_gen in range (1, alc_side + 1):
      overlap_check = 1;
      while overlap_check == 1:
            conflict_check = 0;
            atom_id = c_atom_avail[atom_num, 0];
            usage_check = len(numpy.where(used_c_atoms == atom_id)[0]);
            neigh_num = neigh_list[atom_id - 1, 1];
            for counter in range (1, int(neigh_num + 1)):
```

```
                neigh_id = neigh_list[atom_id - 1, counter + 1];
                pos = numpy.where(c_atom_avail[:, 0] == neigh_id)[0];
                if (c_atom_avail[pos, 3] != 1):
                    conflict_check = conflict_check + 1;
            if ((conflict_check == neigh_num) and (usage_check == 0)):
                alc_pos_top[atom_gen - 1, 0] = atom_id
                c_atom_avail[atom_num, 1] = 1;
                used_counter = used_counter + 1;
                used_c_atoms[used_counter] = c_atom_avail[atom_num, 0];
                overlap_check = 0;
                c_atom_avail[atom_num, 3] = 1;
                atom_num = atom_num + 1;
            else:
                atom_num = atom_num + 1;
#-----------------------------------------------
# Addition of bottom alcohol groups

# Initialize arrays and counters
alc_pos_bottom = numpy.zeros((alc_side, 1));

for atom_gen in range (1, alc_side + 1):
    overlap_check = 1;
    while overlap_check == 1:
        conflict_check = 0;
        atom_id = c_atom_avail[atom_num, 0];
        usage_check = len(numpy.where(used_c_atoms == atom_id)[0]);
        neigh_num = neigh_list[atom_id - 1, 1];
        for counter in range (1, int(neigh_num + 1)):
            neigh_id = neigh_list[atom_id - 1, counter + 1];
            pos = numpy.where(c_atom_avail[:, 0] == neigh_id)[0];
            if (c_atom_avail[pos, 3] != 2):
                conflict_check = conflict_check + 1;
        if ((conflict_check == neigh_num) and (usage_check == 0)):
            alc_pos_bottom[atom_gen - 1] = atom_id
            c_atom_avail[atom_num, 1] = 1;
            used_counter = used_counter + 1;
            used_c_atoms[used_counter] = c_atom_avail[atom_num, 0];
            overlap_check = 0;
            c_atom_avail[atom_num, 3] = 2;
            atom_num = atom_num + 1;
        else:
            atom_num = atom_num + 1;
#-----------------------------------------------
# Addition of top epoxide groups

# Initialize arrays and counters
epox_pos_top = numpy.zeros((epox_side, 2));

#print 'TOP EPOXIDE LOOP'
for atom_gen in range (1, epox_side + 1):
    overlap_check = 1;
    while overlap_check == 1:
        neigh_toggle = 0;
        atom_id = c_atom_avail[atom_num, 0];
        usage_check = len(numpy.where(used_c_atoms == atom_id)[0]);
```

```
            neigh_num = neigh_list[atom_id - 1, 1];
            temp_array = numpy.zeros((neigh_num, 1));
            for neigh_curr in range (1, int(neigh_num + 1)):
                  neigh_check = len(numpy.where(used_c_atoms == (neigh_list[atom_id - 1, 1 + neigh_curr]))[0]);
                  if (usage_check == 0 and neigh_check == 0):
                        temp_array[neigh_toggle, 0] = neigh_list[atom_id - 1, 1 + neigh_curr];
                        neigh_toggle = neigh_toggle + 1;
            temp_array = temp_array[temp_array != 0];
            if len(temp_array) != 0:
                  rand_neigh = random.randint(0, neigh_toggle - 1);
                  epox_pos_top[atom_gen - 1, 0] = atom_id;
                  epox_pos_top[atom_gen - 1, 1] = temp_array[rand_neigh];
                  used_counter = used_counter + 1;
                  used_c_atoms[used_counter] = epox_pos_top[atom_gen - 1, 0];
                  used_c_atoms[used_counter + epox_side] = epox_pos_top[atom_gen - 1, 1];
                  c_atom_avail[atom_num, 2] = 1;
                  pos = numpy.where(temp_array[rand_neigh] == c_atom_avail);
                  c_atom_avail[pos, 2] = 1;
                  atom_num = atom_num + 1;
                  overlap_check = 0;
            else:
                  atom_num = atom_num + 1;
#-----------------------------------------------
# Addition of bottom epoxide groups

# Initialize arrays and counters
epox_pos_bottom = numpy.zeros((epox_side, 2));
used_counter = used_counter + epox_side;

for atom_gen in range (1, epox_side + 1):
      overlap_check = 1;
      while overlap_check == 1:
            neigh_toggle = 0;
            atom_id = c_atom_avail[atom_num, 0];
            usage_check = len(numpy.where(used_c_atoms == atom_id)[0]);
            neigh_num = neigh_list[atom_id - 1, 1];
            temp_array = numpy.zeros((neigh_num, 1));
            for neigh_curr in range (1, int(neigh_num + 1)):
                  neigh_check = len(numpy.where(used_c_atoms == (neigh_list[atom_id - 1, 1 + neigh_curr]))[0]);
                  if (usage_check == 0 and neigh_check == 0):
                        temp_array[neigh_toggle, 0] = neigh_list[atom_id - 1, 1 + neigh_curr];
                        neigh_toggle = neigh_toggle + 1;
            temp_array = temp_array[temp_array != 0];
            if len(temp_array) != 0:
                  rand_neigh = random.randint(0, neigh_toggle - 1);
                  epox_pos_bottom[atom_gen - 1, 0] = atom_id;
                  epox_pos_bottom[atom_gen - 1, 1] = temp_array[rand_neigh];
                  used_counter = used_counter + 1;
                  used_c_atoms[used_counter] = epox_pos_bottom[atom_gen - 1, 0];
                  used_c_atoms[used_counter + epox_side] = epox_pos_bottom[atom_gen - 1, 1];
                  c_atom_avail[atom_num, 2] = 1;
                  pos = numpy.where(temp_array[rand_neigh] == c_atom_avail);
                  c_atom_avail[pos, 2] = 1;
                  atom_num = atom_num + 1;
                  overlap_check = 0;
```

```
            else:
                atom_num = atom_num + 1;
    #---------------------------------------------
    # Generation of oxygen atom coordinates

    # Generate the new printing array
    printarray = numpy.zeros((len(dataset) + atoms_added, 5));
    printarray[0 : len(dataset), :] = dataset;

    # Initialize the counter in appropiate location
    print_atom = (len(dataset) + 1) - 1;

    # Assemble the top basal plane oxygen atoms for OH groups
    for alc_top_count in range (1, alc_side + 1):
        printarray[print_atom, 0] = print_atom + 1;
        printarray[print_atom, 1] = 2;
        printarray[print_atom, 2] = printarray[alc_pos_top[alc_top_count - 1, 0] - 1, 2];
        printarray[print_atom, 3] = printarray[alc_pos_top[alc_top_count - 1, 0] - 1, 3];
        printarray[print_atom, 4] = printarray[alc_pos_top[alc_top_count - 1, 0] - 1, 4] + ao_co;
        print_atom = print_atom + 1;

    # Assemble the bottom basal plane oxygen atoms for OH groups
    for alc_bottom_count in range (1, alc_side + 1):
        printarray[print_atom, 0] = print_atom + 1;
        printarray[print_atom, 1] = 2;
        printarray[print_atom, 2] = printarray[alc_pos_bottom[alc_bottom_count - 1, 0] - 1, 2];
        printarray[print_atom, 3] = printarray[alc_pos_bottom[alc_bottom_count - 1, 0] - 1, 3];
        printarray[print_atom, 4] = printarray[alc_pos_bottom[alc_bottom_count - 1, 0] - 1, 4] - ao_co;
        print_atom = print_atom + 1;

    # Assemble the top basal plane oxygen atoms for epoxide groups
    for epox_top_count in range (1, epox_side + 1):
        printarray[print_atom, 0] = print_atom + 1;
        printarray[print_atom, 1] = 2;
        printarray[print_atom, 2] = (printarray[epox_pos_top[epox_top_count - 1, 0] - 1, 2] +
printarray[epox_pos_top[epox_top_count - 1, 1] - 1, 2])/2 ;
        printarray[print_atom, 3] = (printarray[epox_pos_top[epox_top_count - 1, 0] - 1, 3] +
printarray[epox_pos_top[epox_top_count - 1, 1] - 1, 3])/2;
        printarray[print_atom, 4] = printarray[epox_pos_top[epox_top_count - 1, 0] - 1, 4] + h_epox;
        print_atom = print_atom + 1;

    # Assemble the bottom basal plane oxygen atoms for epoxide groups
    for epox_bottom_count in range (1, epox_side + 1):
        printarray[print_atom, 0] = print_atom + 1;
        printarray[print_atom, 1] = 2;
        printarray[print_atom, 2] = (printarray[epox_pos_bottom[epox_bottom_count - 1, 0] - 1, 2] +
printarray[epox_pos_bottom[epox_bottom_count - 1, 1] - 1, 2])/2 ;
        printarray[print_atom, 3] = (printarray[epox_pos_bottom[epox_bottom_count - 1, 0] - 1, 3] +
printarray[epox_pos_bottom[epox_bottom_count - 1, 1] - 1, 3])/2;
        printarray[print_atom, 4] = printarray[epox_pos_bottom[epox_bottom_count - 1, 0] - 1, 4] - h_epox;
        print_atom = print_atom + 1;

    # Calculate the "number of oxygen atoms" (offset by 2 due to Python indexing)
    # Added to facilitate H atom addition in the printing step
    num_o_atoms = print_atom - len(dataset);
```

```
    #---------------------------------------
    # Generation of hydrogen atom coordinates

    for h_alc_top_count in range (1, alc_side + 1):
            printarray[print_atom, 0] = print_atom + 1;
            printarray[print_atom, 1] = 3;
            printarray[print_atom, 2] = printarray[print_atom - num_o_atoms, 2];
            printarray[print_atom, 3] = printarray[print_atom - num_o_atoms, 3];
            printarray[print_atom, 4] = printarray[print_atom - num_o_atoms, 4] + ao_oh;
            print_atom = print_atom + 1;

    for h_alc_bottom_count in range (1, alc_side + 1):
            printarray[print_atom, 0] = print_atom + 1;
            printarray[print_atom, 1] = 3;
            printarray[print_atom, 2] = printarray[print_atom - num_o_atoms, 2];
            printarray[print_atom, 3] = printarray[print_atom - num_o_atoms, 3];
            printarray[print_atom, 4] = printarray[print_atom - num_o_atoms, 4] - ao_oh;
            print_atom = print_atom + 1;
    #-----------------------------------
    # Output file generation

    # Obtain system information
    num_atoms = len(printarray);

    # Open output file
    output = open(output_name, 'w');
    output.write(str(num_atoms));
    output.write('\n');

    for at_print in range (0, num_atoms):
            if printarray[at_print, 1] == 1:
                output.write('\nC  ' + str(printarray[at_print][2]) + ' ' + str(printarray[at_print][3]) + ' ' +
str(printarray[at_print][4]));
            elif printarray[at_print, 1] == 2:
                output.write('\nO  ' + str(printarray[at_print][2]) + ' ' + str(printarray[at_print][3]) + ' ' +
str(printarray[at_print][4]));
            elif printarray[at_print, 1] == 3:
                output.write('\nH  ' + str(printarray[at_print][2]) + ' ' + str(printarray[at_print][3]) + ' ' +
str(printarray[at_print][4]));

    output.close();
```

The execution code for this function is as follows

```
import oxidation_fun

filename = 'go_1.xyz'
output_name = 'go_f.xyz'
epox_side = 2539;
alc_side = 0; # NEVER CHANGE THIS ENTRY FROM 0
# Begin Code Snippet
# These entries do the same function of the as those in the hydroxyl addition code. See the comments
# for specific details.
```

```
x_max = 100;
y_max = 100;
do_square = 0;
# End Code Snippet

oxidation_fun.oxi_fun(filename,output_name,epox_side,alc_side, x_max, y_max, do_square);
```

Appendix D: Distribution and Homogeneity of PVA Coating on GO-PVA Nanolaminates as a Function of GO Archetype and PVA Molecular Weight

The HRTEM and AFM data presented in Chapter 5 show that microscale polymer features beyond the nanostructured PVA network are present on the surface of GO-PVA nanolaminates (Figure 28b). An understanding of the formation mechanisms behind this hierarchical network can provide insight towards the rational design of nanolaminate systems with novel mechanical properties. Such structures presumably arise through a combination of PVA adsorption at the nanoscale and polymer dewetting at the microscale. At the nanoscale, the first monolayer of PVA chains preferentially adsorbs to the oxidized domains through hydrogen-bonding interactions, thus nucleating preferential sites onto which subsequent PVA chains can adsorb. In addition, because the size of the graphitic domains that punctuate the network of oxidized domains is less than the length of an extended PVA chain, some of the PVA chains can presumably bridge across the graphitic domains to connect to other PVA chains on neighboring oxidized domains. This results in the formation of a nanostructured PVA network. The resulting nanoscale heterogeneity (PVA-sparse graphitic and PVA-dense oxidized regions) presumably leads to differential adsorption of PVA at the microscale, and formation of the PVA features observed in AFM images.

In contrast, when PVA is deposited onto reduced GO (rGO) nanosheets, under the same conditions used to fabricate GO-PVA nanolaminates (see Chapter 2), a largely continuous PVA coating is obtained (Figure 35c). The lack of PVA patterns implies that dewetting does not occur due to the more homogeneous surface of rGO, which primarily contains graphitic domains and relatively few oxidized domains. Furthermore, the highly graphitic nature of rGO implies that it engages in predominantly van der Waals interactions with PVA, rather than the hydrogen-bonding present in GO-PVA nanolaminates. Interestingly, the PVA coating on reduced GO is punctuated

by small pinholes (Figure 35d), suggesting that a small number of oxidized domains serve as surface point heterogeneities that lead to minor dewetting and subsequent pinhole formation.

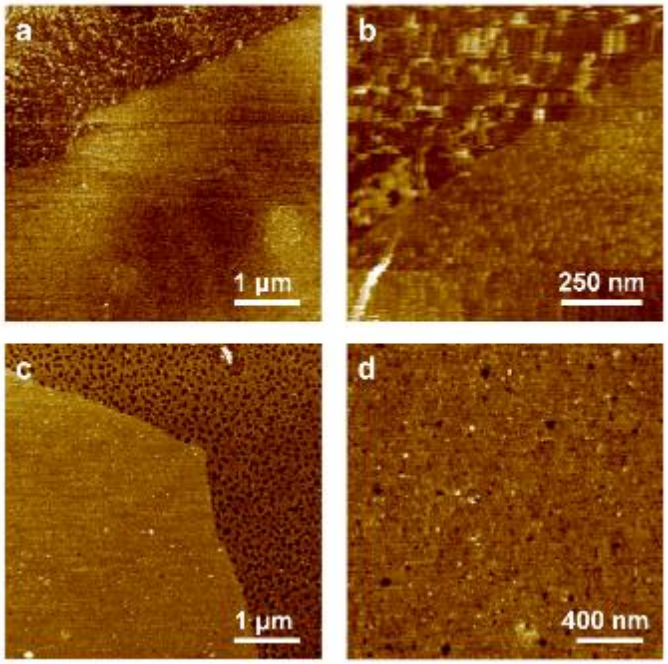

Figure 35. AFM images of GO and rGO modified with PVA of different molecular weights. a, Uneven polymer coverage on the surface of a GO nanosheet modified with PVA (25k). **b,** PVA (25k) aggregating into nanoparticles on the GO surface, suggesting that at higher polymer molecular weight, PVA-PVA interactions are favored over GO-PVA interactions. **c,** rGO modified with a nearly continuous layer of PVA (6k). **d,** Pinholes in the PVA (6k) coating on the rGO surface.

As alluded to in Chapter 5, the formation of the hierarchical PVA network may also depend on polymer size. The PVA chains used in this work (~34 nm extended length, molecular weight of 6k) are comparable in size to 3-4 GO oxidized domains, and can engage in extensive hydrogen-bonding with these domains, leading to the even coating of microscale PVA features on the GO surface (Figure 28b). However, the use of longer PVA chains (~140 nm extended length, molecular weight of 25k) results in uneven coverage of PVA on the GO surface (Figure 35a), implying weaker GO-PVA interactions. This is supported by high-magnification AFM images which reveal PVA nanoparticles on the GO surface (Figure 35b), rather than the microscale features observed when shorter PVA chains are used, suggesting that PVA prefers to engage in intramolecular

hydrogen-bonding instead of interacting with the GO domains. The acquired data demonstrates that selecting a polymer of appropriate size, that is capable of suitable interactions with GO, can allow unique mechanical properties to manifest in the resulting nanolaminate assembly, such as the mesoscale crack-bridging reported herein.